Analysis of neutrino interactions and search for neutral heavy particles with the front calorimeter of the NOMAD experiment

Dissertation
zur Erlangung des akademischen Grades
eines Doktors der Naturwissenschaften
der Abteilung Physik
Universität Dortmund

vorgelegt von Dipl. Physiker
Dirk Geppert

Januar, 2001

Gutachter: Prof. Dr. C. Gößling (Universität Dortmund, Deutschland)
Prof. Dr. S.R. Mishra (Universität South Carolina, USA)

Contents

Introduction

The Standard Model (SM) of particle physics has been extremely successful in describing the properties of the elementary constituents of matter and their interactions. However, it is still regarded as being incomplete. A major shortcoming seems to be the fact that it is not capable of predicting nor explaining the values of the elementary particles masses. In particular, the Standard Model only contains strictly massless and left-handed neutrinos without any indication of a fundamental principle.

The question of the neutrino mass makes neutrino physics to one of the most actual and important topics of particle physics. A neutrino mass, even if very small, would signify that the prominent Standard Model has to be modified and extended. A non-zero neutrino mass would also allow for so-called neutrino oscillations, where strong experimental evidence exists for. These could help to explain the deviation in the theoretical ratio of atmospherical electron to muon type neutrinos and/or the observed deficit of solar neutrinos. Massive neutrinos would also be candidates for a part of the missing non-baryonic matter in the universe providing a better understanding of the expansion of the universe and early formation of large-scale structure.

Many plausible extensions of the Standard Model allow neutrinos to have mass and predict new relatively heavy particles like mirror fermions, vector doublets or singlet neutrinos. For example, in grand unification theories, which try to unify the strong and electroweak forces, new neutrino-like massive states, often called neutral heavy leptons, occur naturally as right-handed isosinglet partners of the light isodoublet neutrinos. In those models, the neutral heavy leptons do not couple directly to the carriers of weak, strong or electromagnetic interactions, but are produced and decay via mixing with the Standard Model light neutrinos.

If observed, the neutral heavy leptons might help to explain and understand better some of the open questions in the Standard Model and provide important impact for possible extensions to the Standard Model.

This thesis presents the results of a search for neutral heavy leptons in the NOMAD[1] experiment at CERN[2] using data collected during the 1996-1998 data taking periods. The neutral heavy leptons are assumed to be produced

[1] **N**eutrino **O**scillation **MA**gnetic **D**etector

[2] **C**entre **E**uropéenne pour la **R**echerche **N**ucléaire, European Laboratory for Particle Physics

in neutrino-like neutral current interactions of neutrinos of the CERN wideband beam in the front calorimeter of the detector. The combination of an instrumented neutrino target (FCAL) followed by an instrumented decay region (NOMAD detector) forms a compelling experimental setup for such a search. A large event statistics is provided by the heavy target, while the light decay analyzer with its excellent measurement capabilities allows to study the properties of the decay products. The analysis concentrates on the subsequent decay of the muon type neutral heavy particle into final states including an identified muon. In the context of the analysis, the energy calibration of the FCAL has been performed and neutrino interactions in the FCAL have been studied.

Outline of this thesis

In Chapter 1 models for neutral heavy leptons, including the mechanisms for production and decay, are described. A summary on the existing experimental situation a given.

Chapter 2 details the NOMAD experiment. The neutrino oscillation search strategy is depicted, followed by a description of the CERN wideband neutrino beam, the NOMAD apparatus and the NOMAD software environment.

Chapter 3 focuses upon the main detector used for this analysis, the NOMAD front calorimeter FCAL. The motivation for its construction is outlined and a detailed sketch of its components is given. A method for the energy calibration is discussed.

Chapter 4 describes the selection and classification of FCAL neutrino interactions. A comparison between real data and *MonteCarlo* events is presented and the achieved agreement of the applied calibration is demonstrated. Further the event timing information of the FCAL in combination with the drift chamber timing information is introduced.

Chapter 5 explains the used *MonteCarlo* simulation of neutral heavy leptons. The implementation is outlined and resulting neutral heavy lepton characteristics are discussed.

Chapter 6 describes the algorithms for the selection of neutral heavy lepton events in general and of the different analyzed decay modes in particular. Selection efficiencies are calculated and the sources for systematic uncertainties are discussed. The concept of the "blind analysis method" is introduced. The number of expected background events is predicted and the observed number of events in the different decay modes is given.

Chapter 7 presents the results of the neutral heavy lepton analysis. Limits are established on the mixing of muon type neutral heavy leptons with Standard Model neutrinos.

Chapter 1

Theory of Neutral Heavy Leptons

In some of the models for new physics beyond the Standard Model of particle physics (SM) neutral heavy leptons are predicted, also referred to in the literature as heavy, right-handed or sterile neutrinos labelled e.g. $L_0, N, \mathcal{N}$, or NHL.

In this thesis models are considered where the neutral heavy leptons are isosinglet partners of the SM neutrinos. The LEP[1] experiments at CERN have measured the number of light neutrino families from the precise study of the Z^0 lineshape. From the ratio of the invisible width Γ_{inv} to the total width of the Z^0 boson they derived the number of neutrino generations as $N_\nu = 2.994 \pm 0.012$ [1]. However, because neutral heavy leptons do not carry charge-like attributes and they do not couple directly to Z^0 and $W^\pm$ bosons, they can contribute only very little to the Z^0 width due to the possible smallness of the coupling occurring through the mixing with ordinary neutrinos.

The SM does not explain why neutrinos are massless nor why they are so much lighter than the other charged leptons. If the left-handed neutrinos were strictly massless a new exact symmetry must be preserved at all orders. An alternative is that neutrinos, unlike other fermions, are Majorana particles and have a unique mechanism of mass generation through mixing with heavy isosinglets.

In this chapter the concepts of Dirac and Majorana neutrinos are described, important for models like GUT and left-right symmetric models extending the SM, and the "See-Saw" mechanism for neutrino mass generation is introduced. Neutral heavy lepton properties such as mixing and mass as well as production and decay are derived. The chapter closes with previous searches and existing experimental limits for the existence of neutral heavy particles.

1.1 Dirac and Majorana neutrinos

In the minimal $SU(2) \times U(1)$ model, neutrinos are predicted to be spin 1/2, electrically neutral, colorless particles which carry conserved lepton number. Since

[1] **L**arge **E**lectron **P**ositron Collider

they have only one helicity state, they are called Weyl neutrinos. However, extensions of the Standard Model involving new $SU(2)_R$ singlet fermions (if neutrinos are massive Dirac particles) or new Higgs representations (if neutrinos are Majorana particles) allow for non-zero masses. First, the expressions *Dirac*- and *Majorana*-neutrinos will be defined and the corresponding mass terms will be introduced.

Dirac neutrinos

Charged leptons and quarks are four component Dirac particles, left- and right-handed[2] particles and their anti-particles. To write the Lagrangian of a free Dirac neutrino, the four chiral components ν_L, ν_R, $(\nu_L)^C$ and $(\nu_R)^C$ are required, where C denotes the charge conjugated partners. Of these four components only those with negative chirality have been observed, i.e. ν_L and $(\nu_L)^C = (\nu^C)_R = \overline{\nu}_R$. Since the components with positive chirality do not take part in charged or neutral currents, they are usually called sterile neutrinos, but they interact with the Standard Model Higgs bosons and are present in the Lagrangian of a free Dirac neutrino and its mass terms[3] [2]:

$$\mathcal{L}^D = \overline{\nu^D}(\imath\gamma^\mu\partial_\mu - m)\nu^D \tag{1.1}$$

$$-\mathcal{L}^D_{\mathcal{M}} = m^D\left(\overline{\nu_L}\nu_R + \overline{\nu_R}\nu_L\right) = m^D\overline{\nu_L}\nu_R + \text{h.c.}^4 \tag{1.2}$$

m^D is the Dirac mass denoting the strength of the coupling between left- and right-handed fields. Since both ν_L and ν_R are necessary to describe the Dirac mass term but ν_R are not observed, the Standard model implies that the neutrino mass is zero.

Majorana neutrinos

Particles being their own anti-particles are called Majorana particles, only possible for particles not carrying charge-like attributes like electric charge, lepton or baryon number. Since neutrinos, as far as known, do not carry any charge-like attribute, they can be defined as Majorana neutrinos:

$$\nu^M = (\nu^M)^C \equiv C^{-1}\nu^M C. \tag{1.3}$$

[2]The terms left- and right-handed are used in the literature referring to both *chirality* and *helicity*, which are different concepts. The chirality operator is γ_5, whereas the helicity operator is $\vec{\sigma}\cdot\hat{p}$, the spin projection on the direction of motion. Since the latter commutes with the free Hamiltonian, the helicity states are the physical states for free particles. Only in the case of massless particles γ_5 commutes as well with the free Hamiltonian. It is important to note that chirality is a Lorentz invariant concept but not directly measurable, whereas helicity is, but is frame dependent.

[3]Unless otherwise specified, "natural" units in which $\hbar = c = 1$ are used.

[4]**h**ermetian **c**onjugate

The free Lagrangian for a Majorana neutrino is given by:

$$\mathcal{L}^M = \frac{1}{2}\overline{\nu^M}(\imath\gamma^\mu\partial_\mu - m)\nu^M, \tag{1.4}$$

where the factor 1/2 takes care of double counting when an interaction term is added to the free Lagrangian. In the Majorana mass term, the fermion fields ν_L and ν_R are coupled to their charge conjugates[5] and the Majorana masses $m^M_{L,R}$ give the strength of the coupling. There are two mass terms in the Lagrangian:

$$\begin{aligned} -2\mathcal{L}^M_{\mathcal{M}} &= m^M_L\left(\overline{\nu_L}\nu^C_R + \overline{\nu^C_R}\nu_L\right) + m^M_R\left(\overline{\nu_R}\nu^C_L + \overline{\nu^C_L}\nu_R\right) \\ &= m^M_L\overline{\nu_L}\nu^C_R + m^M_R\overline{\nu^C_L}\nu_R + \text{h.c.} \end{aligned} \tag{1.5}$$

depending on whether the left- or right-handed fields are coupled.

The Dirac and Majorana particles are different only if the neutrino rest mass is not zero. If the neutrino has no mass and travels at the speed of light, then a Lorentz transformation to a faster moving frame is not possible and the classification *w.r.t.* helicity is only theoretical. On the other hand, if the neutrino mass is non zero, it would be possible to decide experimentally if neutrinos are of type Dirac or Majorana: a massive Dirac neutrino has nonzero magnetic and electric dipole moments, whereas Majorana neutrinos are invariant under a charge conjugation C, they cannot have a magnetic moment.

The Dirac mass term is invariant under the global phase transformation $\nu \rightarrow e^{\imath\alpha}\nu$, thus it can be associated with a conserved quantum number, the lepton number. The Majorana neutrino is a linear combination of two components with lepton number $L = +1$ and $L = -1$; in consequence, the lepton number violation is $\Delta L = \pm 2$, an important ingredient for neutrino-less double-beta decay. Lepton number violation is only possible in extensions to the Standard Model. Although the SM Lagrangian does not have any terms that violate lepton number, there is no intrinsic gauge symmetry that would require that lepton number is conserved.

The theory of Dirac neutrinos provides no explanation why neutrinos are so much lighter, if non-zero, with respect to the other fermions of the same generation. If one assumes a neutrino mass as solely a Dirac mass, $m^D = g_\nu < \phi^0 >$, than a ν_e mass in the 10 eV/c^2 range would require an extremely small coupling ($g_{\nu_e} \leq 10^{-10}$). Moreover, g_{ν_e} would have to be smaller by $m_{\nu_e} \leq 10^{-4}$ than the analogous Yukawa coupling for the electron. Majorana masses are different from the Dirac masses of the quark and charged lepton masses and provide therefore a possibility to explain the difference between neutrino and charged fermion masses.

[5] here $\nu^C_{L,R} \equiv \left(\nu^C\right)_{L,R} = \left(\nu_{R,L}\right)^C$; others define sometimes $\nu^C_{L,R} \equiv \left(\nu_{L,R}\right)^C$

1.2 General mass term

The most general mass Lagrangian for the neutrino can be written as a sum of Dirac and Majorana mass terms [2]:

$$-2\mathcal{L}_{\mathcal{M}} = m_D \left(\overline{\nu_L}\nu_R + \overline{\nu_L^C}\nu_R^C\right) + m_L\overline{\nu_L}\nu_R^C + m_R\overline{\nu_L^C}\nu_R + \text{h.c.} \tag{1.6}$$

This equation can be rewritten in the more comfortable matrix form:

$$-2\mathcal{L}_{\mathcal{M}} = \overline{N_L}\mathcal{M}N_R^C + \text{h.c.} \tag{1.7}$$

with $N_L \equiv \begin{pmatrix}\nu_L \\ \nu_L^C\end{pmatrix}$, such that $(N_L)^C = N_R^C$, and

$$\mathcal{M} = \begin{pmatrix} m_L & m_D \\ m_D & m_R \end{pmatrix}. \tag{1.8}$$

A mass matrix like this indicates some kind of mixing between mass and weak eigenstates. To find its corresponding eigenstates and eigenvalues the matrix has to be diagonalized finding:

$$\begin{aligned} \nu_L^{'} &= +\nu_L \cos\theta + \nu_L^C \sin\theta \\ \nu_L^{C'} &= -\nu_L \sin\theta + \nu_L^C \cos\theta \end{aligned} \tag{1.9}$$

with the mixing angle $\tan 2\theta = \frac{2m_D}{m_R - m_L}$ and

$$m_{1,2} = \frac{1}{2}\left\{(m_L + m_R) \pm \sqrt{(m_L - m_R)^2 + 4m_D^2}\right\}. \tag{1.10}$$

Under the assumption $m_L \ll m_D \ll m_R$, motivated in the following two sections, the relation for the eigenvalues simplifies significantly leading to the so-called "See-Saw" model described in Section 1.5.

1.3 Grand Unified Theories

Grand Unified Theories (GUT) unite electroweak and strong forces at energies greater than the mass scale $M_{\text{GUT}} = 10^{14} - 10^{16}$ GeV/c^2. Above this mass scale the running couplings of weak, strong and electromagnetic forces merge and may be described by a "Grand Unification" theory.

GUT theories introduce additional sets of Higgs bosons responsible for the symmetry breaking between strong and electroweak interactions at M_{GUT} scale. As a result of this spontaneous symmetry breaking these additional Higgs multiplets Φ develop vacuum expectation values and set the mass scale for both gauge bosons and fermions.

GUTs based on groups larger than $SU(5)$ [3–5] predict the existence of heavy weak isosinglets N that couple with the Standard Model neutrinos. Mass eigenstates ν' and N' are related to the weak eigenstates ν and N via the mixing matrix in Equation 1.8:

$$\begin{pmatrix} \nu' \\ N' \end{pmatrix} = \begin{pmatrix} m_L & m_D \\ m_D & m_R \end{pmatrix} \begin{pmatrix} \nu \\ N \end{pmatrix}. \tag{1.11}$$

The mixing matrix enters the neutrino mass Lagrangian in the form of Equation 1.7. The parameters m_D, m_L and m_R appear in the Lagrangian as a result of the interaction of ν and N fields with the Higgs fields, resulting in Majorana terms:

$$\begin{aligned} m_D &= h_\nu \overline{\nu}_L \Phi \nu_R \\ m_L &= h' \overline{\nu}_L^C \Delta_L \nu_L \\ m_R &= h' \overline{\nu}_R^C \Delta_R \nu_R, \end{aligned} \tag{1.12}$$

where h_ν is the Yukawa coupling of the neutrinos to a Higgs field Φ, and h' the Yukawa coupling to Δ_L and Δ_R. It appears that the coupling of any additional Higgs doublet to the SM fermion fields would result in observable consequences. Therefore the vacuum expectation value of Δ_L must be small. On the other side, there are no constraints on the vacuum expectation value of the singlet field Δ_R. Its mass scale must be large because there is no experimental evidence for an additional right-handed gauge boson. GUT predicts the mass of the weak singlet eigenstate of the order of the GUT mass scale. This leads to the relation between the Dirac and Majorana masses:

$$m_L \ll m_D \ll m_R. \tag{1.13}$$

Under this assumption the mass eigenvalues in Equation 1.10 are:

$$\begin{aligned} m_1 &= m_{\nu'} \simeq m_D^2 / m_R \\ m_2 &= m_{N'} \simeq m_R. \end{aligned} \tag{1.14}$$

Choosing e.g. $m_D \simeq 1$ GeV/c^2 and $m_R \simeq 10^{15}$ GeV/c^2 GUT predicts one very small mass corresponding to the left-handed neutrino and its extremely heavy right-handed partner:

$$m_{\nu'} \simeq 10^{-15} \text{ GeV}/c^2 \text{ and } m_{N'} \simeq 10^{15} \text{ GeV}/c^2. \tag{1.15}$$

1.4 Left-right symmetrical model

Heavy neutrinos are also predicted in the so-called left-right symmetrical model $SU(2)_L \times SU(2)_R \times U(1)_{B-L}$ [6], where the basic weak Lagrangian is invariant

under space reflection, as are electromagnetic and strong interactions. It therefore involves both $(V-A)$ as well as $(V+A)$ charge currents and predicts the existence of a right-handed gauge boson W_R. The observed predominance of left-handed weak interactions at low energies is understood as a consequence of the fact that the vacuum is not symmetric under space reflection. In the left-right symmetric models, since both left and right-handed helicities of the neutrino are included, the neutrino naturally has a mass. Additional Higgs multiplets Δ_L, Δ_R and Φ are introduced. The various stages of symmetry breaking are:

$$SU(2)_L \times SU(2)_R \times U(1)_{B-L} \xrightarrow{<\Delta_R>\neq 0, <\Delta_L>=0} SU(2)_L \times U(1) \ . \tag{1.16}$$

The subsequent breakdown of $SU(2)_L \times U(1)$ down to $U_{em}(1)$ is achieved via the Standard Model Higgs $< \Phi > \neq 0$.

The neutrino mass Lagrangian after symmetry breaking is:

$$-2\mathcal{L}_{\mathcal{M}} = h' \left(\nu_L^T v_L C \nu_L - \nu_R^{C^T} v_R C \nu_R^C \right) + h \nu_L^T v_1 C \nu_R^C + \text{h.c.}, \tag{1.17}$$

where C is the charge conjugation matrix, ν^T is the transposed field, $v_L \equiv < \Delta_L^0 >$, $v_R \equiv < \Delta_R^0 >$ and $v_1 \equiv < \Phi >$ are the vacuum expectation values and h is the Yukawa coupling to Φ and h' the Yukawa coupling to Δ_L and Δ_R.

In matrix form

$$-2\mathcal{L}_{\mathcal{M}} = (\overline{\nu}^T N^T) \mathcal{M} \begin{pmatrix} \nu \\ N \end{pmatrix} + \text{h.c.} \tag{1.18}$$

where $\nu \equiv (\nu_L N) \equiv C(\overline{\nu}_R)^T$ and $\mathcal{M}$ is a mass matrix similar to Equation 1.8 with $m_D \equiv h v_1$, $m_L \equiv h' v_L$, $m_R \equiv h' v_R$ and its eigenstates

$$\begin{aligned} \nu' &= +\nu \cos\theta + N \sin\theta \\ N' &= -\nu \sin\theta + N \cos\theta \end{aligned} \tag{1.19}$$

with $\tan 2\theta = \frac{2m_D}{m_R - m_L}$.

For the eigenvalues of the mass matrix one can find two different solutions depending on the number of Higgs bosons in the theory:

- There is only one Φ in the theory, whose vacuum expectation value sets the mass scale for both left-handed gauge bosons and fermions. One then attributes a tiny fermion mass to the arbitrary chosen small Yukawa couplings

$$\begin{aligned} m_{\nu'} &\simeq m_L + m_D^2 / m_R \\ m_{N'} &\simeq m_R. \end{aligned} \tag{1.20}$$

- Postulating the existence of two Φ's the small fermion mass may originate from a different mass scale than the masses of the gauge bosons, with one of them coupling to the fermions and providing their small masses through its small vacuum expectation value

$$\begin{aligned} m_{\nu'} &\simeq m_D^2/m_R \\ m_{N'} &\simeq m_R. \end{aligned} \tag{1.21}$$

m_R is related to the mass of the right-handed boson via the Yukawa coupling $h/g = m_R/m_{W_R}$, where h is the Yukawa coupling of the Higgs to the fermions and g the Yukawa coupling to the gauge bosons.

The left-right symmetric model leads to the same relation as the GUT model: the mass of the right-handed neutrino N is of the same order as the mass of the right-handed boson:

$$m_{N'} \simeq m_{W_R} \simeq 10^5 \text{ GeV}/c^2. \tag{1.22}$$

1.5 The See-Saw mechanism

The resulting relations between the mass eigenvalues of the left-handed neutrino and its heavy right-handed partner can be generalized leading to one of the most popular models in the literature for generating neutrino masses, the so-called "See-Saw" model [7]. For each lepton family with its light left-handed neutrino coupling to its family charged lepton via weak charged currents, a heavy right-handed Majorana neutrino as a weak isosinglet is postulated which does not couple to any fermions or bosons directly.

Both the GUT and left-right symmetric model predict the relation:

$$m_L \ll m_D \ll m_R \tag{1.23}$$

so that the mass eigenvalues are:

$$\begin{aligned} m_1 &\simeq m_D^2/m_R \ll m_D \\ m_2 &\simeq m_R \end{aligned} \tag{1.24}$$

with $m_2 \gg m_D \gg m_1$. This is the See-Saw mechanism: with fixed m_D the light neutrino gets lighter as the hypothetical heavy neutrino gets heavier. The mass of the light neutrino is generated by the See-Saw mechanism. The eigenstates Equation 1.9 can be rewritten as:

$$\begin{aligned} \nu' &= \nu(1 - \frac{\xi^2}{2}) + N\xi \\ N' &= -\nu\xi + N(1 - \frac{\xi^2}{2}) \end{aligned} \tag{1.25}$$

where $\xi \simeq m_D/m_R$. The mass m_D is a typical Dirac mass of a fermion (lepton or quark), thus the See-Saw mechanism naturally leads to neutrino masses much smaller than the fermion masses. On the other hand, there is no indication on what fermion mass is qualified to be "typical".

The See-Saw mechanism for three generations

The See-Saw model can be generalized to 3 families leading to a 6×6 mass matrix. Assuming that m_R is about the same for all three families

$$m_R \simeq \begin{pmatrix} 1 & 0 & 0 \\ 0 & 1 & 0 \\ 0 & 0 & 1 \end{pmatrix} \tag{1.26}$$

one gets the so-called *quadratic* See-Saw prediction:

$$m_{\nu_e} : m_{\nu_\mu} : m_{\nu_\tau} = m_e^2 : m_\mu^2 : m_\tau^2. \tag{1.27}$$

If m_R would follow the family hierarchy:

$$m_R \simeq \begin{pmatrix} m_e & 0 & 0 \\ 0 & m_\mu & 0 \\ 0 & 0 & m_\tau \end{pmatrix} \tag{1.28}$$

the quadratic dependence is replaced by the *linear* dependence on m_D:

$$m_{\nu_e} : m_{\nu_\mu} : m_{\nu_\tau} = m_e : m_\mu : m_\tau \tag{1.29}$$

One could also choose the up-quark masses instead of the charged lepton partner of the neutrino in which case the corresponding masses in the upper relations would have to be changed to the appropriate quark masses.

Summary

In summary, both GUT and left-right symmetrical models provide a mechanism for the neutrino mass generation. The See-Saw mechanism naturally follows from these theories. However, both models predict extremely heavy neutral heavy leptons: more than $\simeq 10^{14}$ GeV/c^2 for GUT and $\simeq 10^5$ GeV/c^2 for left-right symmetry. Both these values are out of reach for any experiment in the foreseeable future.

Fine tunings and modifications within the models are possible, or one may assume that the symmetry breaking occurs at lower than GUT and LR scales, resulting in NHL masses being in experimental reach.

Also, it is not clear what to use as a typical Dirac mass: the mass of the charged lepton or the quark mass from the same family or the lepton/quark mass

from other families. Given present bounds on the muon neutrino mass $m_{\nu_\mu} \leq 0.5$ keV/c^2 and taking a typical Dirac mass as $m_D = m_e = 0.5$ MeV/c^2 one could estimate the neutral heavy lepton mass of the muon family m_R using the See-Saw mechanism:

$$m_R \simeq \frac{m_D^2}{m_{\nu_\mu}} = 0.5 \text{ GeV}/c^2. \tag{1.30}$$

There are alternative theories [8–10] which predict the same mechanism for neutrino mass generation and much lighter neutral heavy leptons.

Without strong theoretical indications on the neutral heavy lepton mass range, except that it should be relatively heavy, the whole range from $\simeq 0.1$ GeV/c^2 to infinity is open for searches.

1.6 Neutral Heavy Leptons

In GUT or left-right symmetric models, as shown in the previous sections, additional heavy neutral leptons occur which are primarily isosinglets under ordinary weak $SU(2)$. Since the NHL does not have electromagnetic, strong or weak charge it consequently does not interact with matter and can only be produced via the mixing with SM neutrinos in such a way that fundamental weak isodoublets acquire some admixture of the heavy states.

Introducing the mixing parameter $|U| \equiv \xi \simeq m_D/m_R$ the weak eigenstates relations in the See-Saw mechanism Equation 1.25 can be rewritten as:

$$\begin{aligned} \nu' &\simeq \nu(1 - \frac{|U|^2}{2}) + N|U| \\ N' &\simeq -\nu|U| + N(1 - \frac{|U|^2}{2}). \end{aligned} \tag{1.31}$$

The general mixing between ordinary and heavy neutrinos is described by a 3×3 mixing matrix U_{ij}:

$$U = \begin{pmatrix} U_{ee} & U_{e\mu} & U_{e\tau} \\ U_{\mu e} & U_{\mu\mu} & U_{\mu\tau} \\ U_{\tau e} & U_{\tau\mu} & U_{\tau\tau} \end{pmatrix} \tag{1.32}$$

in which case the SM neutrinos $i = e, \mu, \tau$ are substituted as:

$$\nu_i' \simeq \nu_i \left(1 - \frac{\sum_a |U_{ia}|^2}{2}\right) + \sum_a N_a |U_{ia}| \tag{1.33}$$

where the sum is over heavy lepton species a. The weak eigenstates are now ν_i'; mass eigenstates are ν_i (light) and N_a (heavier). Equation 1.33 leads to both

charged and neutral currents connecting the heavy leptons with the familiar light ones.

In a model in which a neutrino mixes with another isodoublet, one can expect a suppression of flavor-changing neutral currents ($FCNC$) analogous to that which holds for quarks. Also mixing of the known isodoublet neutrinos with higher isodoublet (sequential leptons) could appear. For both cases strong experimental constraints exist, e.g. the total Z^0 width. One can evade these by assuming that mixing between ordinary and heavy neutrinos occurs only diagonally, i.e. with a single correspondence between light and heavy states: $U = diag(U_{ee}, U_{\mu\mu}, U_{\tau\tau})$.

1.6.1 Production of NHL

Neutral heavy leptons could be produced e.g. in the semileptonic decays of charged mesons or in neutrino beams via deep-inelastic neutral weak current interactions. The latter is the case for the analysis performed in this thesis where the beam consists predominantly of muon type neutrinos ν_μ. For a model described by Equation 1.33 with no inter-family mixing the transition is $\nu_\mu \to \mathcal{N}_\mu$.

Then the production cross-section for neutral heavy leptons may be expressed as that of an ordinary weak current (with a neutral heavy lepton in the final state instead of the light neutrino) times the square of the mixing parameter $|U_{\mu\mu}|^2$ times a suppression factor depending on the mass $m_{\mathcal{N}_\mu}$ of the $\mathcal{N}_\mu$(see GLR [11]):

$$d\sigma(\nu_\mu N \to \mathcal{N}_\mu X) = d\sigma(\nu_\mu N \to \nu_\mu X) \times |U_{\mu\mu}|^2 \times \left(1 - \frac{m^2_{\mathcal{N}_\mu}}{xs}\right)^2 \times \Theta(xs - m^2_{\mathcal{N}_\mu}) \tag{1.34}$$

with the Θ-function:

$$\Theta(z) \equiv \begin{cases} 1 & \text{for } z \geq 0 \\ 0 & \text{for } z < 0 \end{cases} \tag{1.35}$$

The kinematical factor $S_m = \left(1 - \frac{m^2_{\mathcal{N}_\mu}}{xs}\right)^2$ (x: Bjorken x, $\sqrt{s}$: center of mass energy) takes into account the reduction of phase space for the production of the heavy lepton and follows directly from calculating the first order matrix element [12] for the Feynman diagram describing the process depicted in Figure 1.1. The Θ-function assures that the struck quark carries a sufficient fraction of the center of mass energy, xs, to generate a neutral heavy lepton of mass $m_{\mathcal{N}_\mu}$.

1.6.2 Decay of NHL

Because of its mass the neutral heavy lepton has a finite lifetime. In Figure 1.2 the typical decay mechanism is shown, where both neutral and charged currents

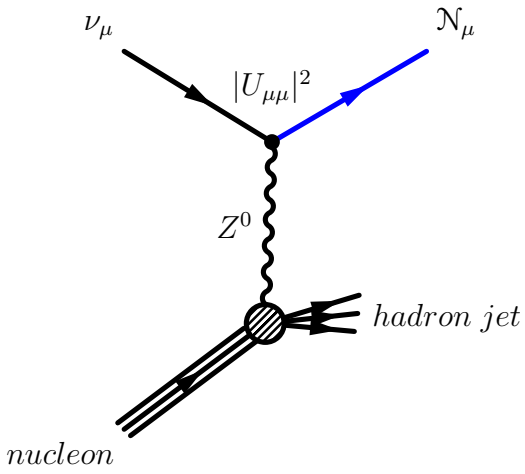

Figure 1.1: *Feynman diagram for $\mathcal{N}_\mu$ production in deep-inelastic neutrino-nucleon interaction via weak neutral current.*

can contribute. The total decay rate may be expressed in terms of the muon decay width [11]:

$$\Gamma_{\mathcal{N}_\mu} = \Gamma_\mu \cdot \left(\frac{m_{\mathcal{N}_\mu}}{m_\mu}\right)^5 \cdot \Phi \cdot |U_{\mu\mu}|^2 \tag{1.36}$$

The decay width is proportional to the effective number Φ of unit-strength charged current channels which can be calculated [11]:

$$\Phi_\mu = 6.95 \cdot \left(\frac{m_{\mathcal{N}_\mu}}{1\ \mathrm{GeV}/c^2}\right)^{0.19} \tag{1.37}$$

So the lifetime of the muon type neutral heavy lepton is (with $m_\mu = 105.658\ \mathrm{MeV}/c^2$ [1]):

$$\tau_{\mathcal{N}_\mu} = 4.51 \cdot 10^{-12}\ \mathrm{sec} \cdot \left(\frac{m_{\mathcal{N}_\mu}}{1\ \mathrm{GeV}/c^2}\right)^{-5.19} \cdot |U_{\mu\mu}|^{-2} \tag{1.38}$$

Figure 1.3 shows the lifetime as a function of the mixing parameter $|U_{\mu\mu}|^2$ and mass $m_{\mathcal{N}_\mu}$. For a mass of $\simeq 3\ \mathrm{GeV}/c^2$ and mixing parameter $\simeq 2 \cdot 10^{-5}$ the lifetime is $\simeq 10^{-9}$ sec corresponding to a mean flight length of $\gamma c\tau \simeq 2.4$ m for a typical energy of 24 GeV, corresponding to the experimental setup of this analysis (see Chapters 2 and 3).

For muon type neutral heavy leptons typical branching ratios into specific final states for different masses are listed in Table 1.1 (from [11]). With increasing mass $m_{\mathcal{N}_\mu}$ the number of possible decay modes increases. Attempts have been made to further subdivide and calculate the branching ratios more precisely [13], but the

calculations depend strongly on assumptions made for the type of neutral heavy lepton.

The only undetectable final state is $\mathcal{N}_\mu \rightarrow \nu\nu\overline{\nu}$ with about 15% branching ratio. In this thesis the decay modes with a charged lepton in the final states will be considered using the excellent lepton identification of the apparatus. The mode $\mathcal{N}_\mu \rightarrow e^- e^+ \nu_\mu$ is excluded because of its small branching ratio as well as the hadronic mode $\mathcal{N}_\mu \rightarrow \nu_\mu q\overline{q}$ because of the missing identification power (no charged lepton). So the analyzed fraction of the total decay width is $\simeq 60\%$.

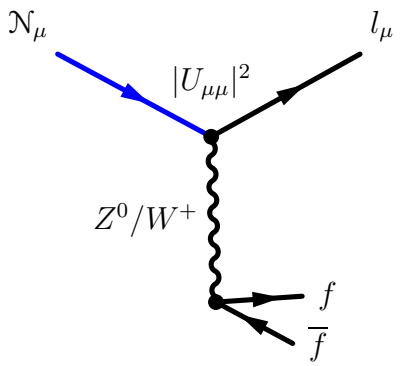

Figure 1.2: *Feynman diagram for the decay of* $\mathcal{N}_\mu$.

final state	type	0.5	1.0	2.0
$\mu^- e^+ \nu_e$	CC	13.6%	13.8%	13.8%
$\nu_\mu e^+ e^-$	NC	2.4%	1.9%	1.8%
$\mu^- \mu^+ \nu_\mu$	NC/CC	5.5%	7.3%	7.7%
$\nu\nu\overline{\nu}$	NC	19.0%	15.0%	14.1%
$\mu^- q\overline{q}$	CC	40.5%	41.2%	41.3%
$\nu_\mu q\overline{q}$	NC	18.9%	20.8%	21.3%

Table 1.1: *Decay branching ratios in per cent and type of weak decay for* $\mathcal{N}_\mu$ *into specific final states for different masses* $m_{\mathcal{N}_\mu} = 0.5, 1.0, 2.0\ GeV/c^2$.

1.7 Previous Neutral Heavy Lepton searches

Previous experiments searching for neutral heavy leptons, starting about 25 years ago, may be categorized based on the source of NHL production into five types:

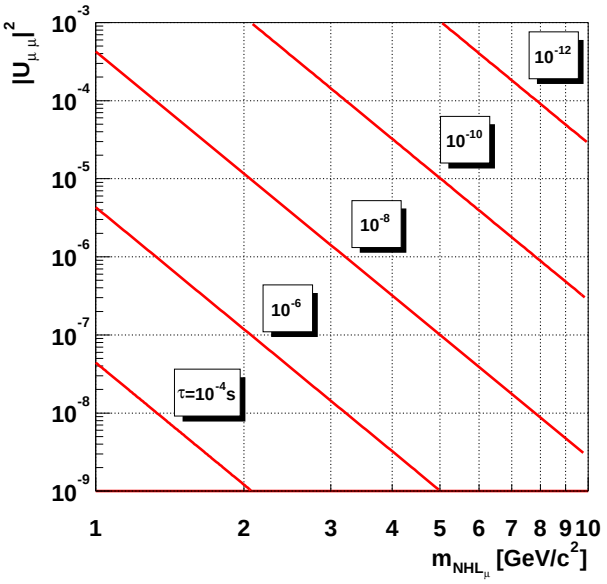

Figure 1.3: *Lifetime of a muon type neutral heavy lepton* $\mathcal{N}_\mu$ *as a function of the mixing parameter* $|U_{\mu\mu}|^2$ *and mass* $m_{\mathcal{N}_\mu}$.

β-decays

Here β-sources are analyzed for an admixture of neutral heavy leptons. All experiments were negative hitherto [14–22].

Neutrino decays in reactor experiments

Because neutral heavy leptons are heavier than anti-electron neutrinos they may decay into an anti-electron and a gamma or, if the mass is sufficient, into an anti-electron neutrino plus a e^+e^- pair. Reactor experiments have searched for these kind of signatures [23–25].

Two-body decays of mesons

The semileptonic decays of charged mesons like pions, kaons, D and D_S were analyzed for the presence of neutral heavy leptons with different techniques:

- The final state kinematics of decay modes with a charged lepton and a neutrino were investigated. Without the presence of a NHL the momentum spectrum of the charged lepton would peak (two-body decay with missing neutrino momentum). An admixture of a NHL would result in a second peak whose distance and relative height *w.r.t.* the Standard Model neutrino peak would indicate the mass and mixing parameter.

- A direct NHL measurement is possible in so-called beam-dump experiments where e.g. a proton beam hits a thick target such that the large number of secondary mesons are stopped in the target producing neutrinos and possibly neutral heavy leptons. These experiments are usually limited in the NHL mass range by the mass of the mesons (decay at rest).

In none of the experiments [26–48] an evidence for neutral heavy leptons was found. Only the so-called KARMEN anomaly (see below) may be interpreted as a possible decay of a slow moving heavy neutral particle.

Collider searches

In collider searches possible sources for NHL are the decays of $W^{\pm}$ and Z^0 bosons, where the neutral heavy leptons are produced and decay inside the detector. These experiments were sensitive for high NHL masses up to the boson mass. For smaller NHL masses the lifetime and so the decay length increases and the decay occurs outside the acceptance of the detector ($\lesssim 3$ GeV/c^2). No evidence was found in the LEP experiments [49–52] at CERN.

Direct production in neutrino-nucleon scattering

In high-statistics neutrino experiments one might expect several million neutral current events which can be analyzed for the presence of neutral heavy leptons. Depending on the experimental setup these experiments are sensitive for different NHL masses, determined by the distance of the neutrino neutral current interaction target and the decay analyzer. Previous experiments like CHARM [53, 54] and CCFR [55, 56], essentially huge iron-sampling calorimeters, were both, target and analyzer, at the same time and limited in their sensitivity by the granularity of the detector: the decay vertex had to be well separated from the production vertex. The search for neutral heavy leptons was negative [57–60].

The KARMEN anomaly

The KARMEN neutrino experiment [61] used a pulsed proton beam to generate pions which decay into a muon and neutrino, with the muon subsequently decaying yielding muon and electron neutrinos. Neutrino interactions are observed and their timing spectrum is characteristic for the muon lifetime. However, there is an excess of events in the neutrino timing distribution, which can be interpreted as the decay of a slow moving particle, $v \simeq 0.016\ c$, arriving 3.6 μs after the pulse. A possible explanation is the existence of a 33.9 MeV/c^2 NHL produced in the pion decay $\pi \to \mu\mathcal{N}$. The potential NHL is on the edge of available phase space, and therefore travels slowly in the π rest frame, making this type of detection possible.

Four other experiments could not confirm such kind of NHL [41, 62–64]. However, there are other explanations such as exotic muon decay $\mu^+ \rightarrow e^+X$, but searches in the region of the KARMEN anomaly have been negative [65, 66].

Figure 1.4 shows the existing experimental limits at 90% confidence level ($C.L.$) (the exclusion curve from the L3 experiment shows 95% $C.L.$) on muon type neutral heavy leptons from experiments L3 [51],CHARMII [57],CCFR [58], sensitive in the same region as the also drawn estimated sensitivity of this experiment (from [67]). The regions inside the curves are excluded.

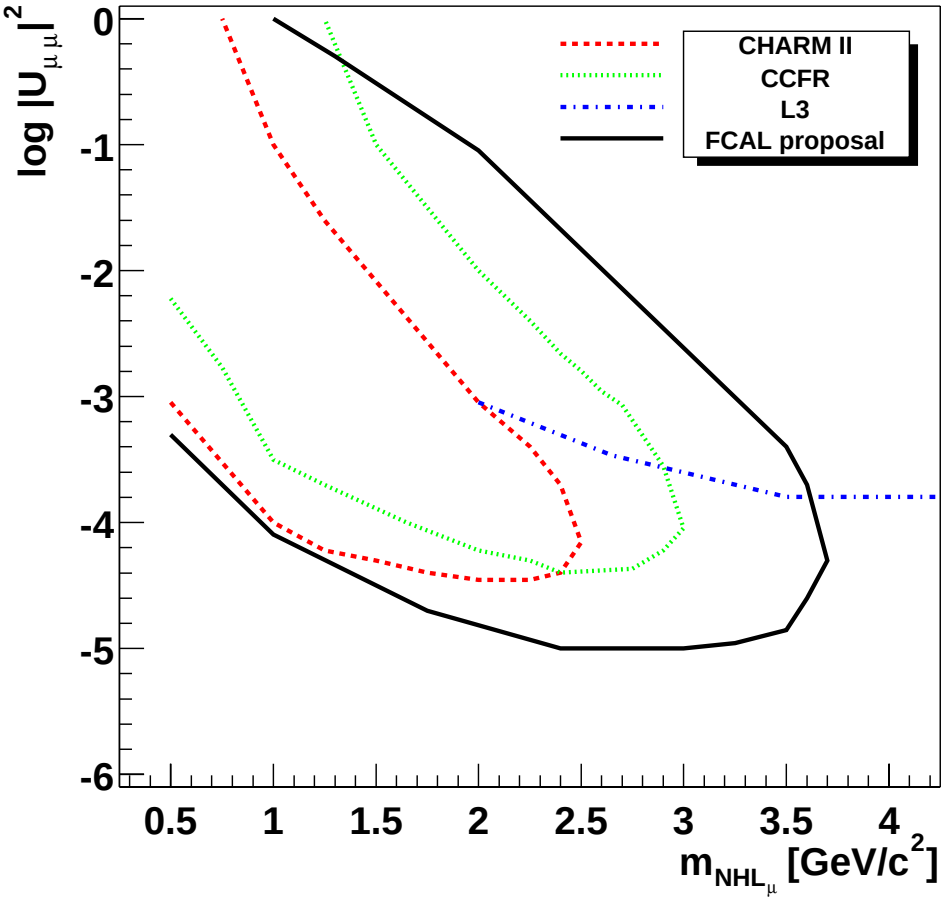

Figure 1.4: *Existing limits on muon type neutral heavy lepton mixing parameter and mass from experiments sensitive in the same region as this experiment.*

Chapter 2

The NOMAD experiment

The NOMAD (**N**eutrino **O**scillation **MA**gnetig **D**etector) [68] experiment is designed for the appearance search of tau neutrinos ν_τ in the CERN SPS wideband neutrino beam. The beam has a mean energy of 24 GeV and predominantly consists of muon neutrinos ν_μ. As a byproduct, the experiment can set limits on $\nu_\mu \leftrightarrow \nu_e$ oscillations.

NOMAD is sensitive on the mixing between ν_μ and ν_τ to the mass difference squared $\Delta m^2 > 1$ eV^2 with a maximal sensitivity obtained for $\Delta m^2 > 40$ eV^2.

Two different approaches have been envisaged to detect τ production via ν_τ^{CC} interactions:

- The proper τ decay length at SPS beam energies is $c\tau = 88.6$ μm and can be measured with a high precision position detector. A practical choice adopted by the CHORUS experiment [69] is an emulsion detector, allowing to measure the τ decay path on an event-by-event basis with an almost negligible background. The disadvantage of this approach is the very time consuming emulsion scanning process, requiring years for the analysis for the 10^6 event statistics of the experiment.

- An alternative approach, chosen by NOMAD, is to identify the τ's with kinematical criteria: the differences in the final state kinematics between ν_μ- and ν_τ-induced charged current interactions. In this way it is possible to search on a statistical basis for an excess of τ candidates over the background.

The kinematical analysis techniques and the design of the NOMAD detector are the subject of this chapter.

Decay channel	BR[%] [1]	ϵ [%]	BR $\times \epsilon$ [%]	N_τ	$N_{\rm BKG}$
$\tau^- \to e^- \overline{\nu}_e \nu_\tau$	17.81 $\pm$ 0.07	13.5	2.4	39	4.6
$\tau^- \to \mu^- \overline{\nu}_\mu \nu_\tau$	17.37 $\pm$ 0.09	3.9	0.7	11	2.2
$\tau^- \to h^- \nu_\tau$	11.79 $\pm$ 0.24	1.5	0.2	3	$\leq$0.2
$\tau^- \to \rho^- \nu_\tau$	25.32 $\pm$ 0.15	2.2	0.6	7	$\leq$0.2
$\tau^- \to h^- h^- h^+ n\pi^0 \nu_\tau$	15.18 $\pm$ 0.13	7.7	1.1	18	$\leq$0.2
Total	87.5		5.0	78	$\simeq 7$

Table 2.1: *Sensitivity of the NOMAD experiment to the different τ decay modes (from [68])*

2.1 Search for $\nu_\mu \leftrightarrow \nu_\tau$ oscillations with NOMAD

In order to increase the sensitivity for the oscillation search the NOMAD detector is designed to detect most of the τ decay modes, listed in Table 2.1, together with their estimated analysis efficiencies (at the time of the proposal of the experiment) and the expected number of τ and background events. The kinematical analysis strategy is determined by the dominant background to the different channels. From this point of view, the accessible signatures can by divided into two categories, the leptonic and the hadronic decay modes. A brief description of the general analysis criteria used for the two classes will be given here. More detailed descriptions may be found in [70] and [71].

Leptonic channels

The search for leptonic τ decays starts with the identification of the lepton, μ or e, produced close to the ν_τ^{CC} interaction vertex. The dominant background for the two leptonic channels are the corresponding charged current neutrino interactions, $\nu_\mu^{CC}$and ν_e^{CC}, producing the lepton directly at the interaction vertex. Figure 2.1 illustrates the kinematic selection criteria used to distinguish background from signal events. The missing momentum transverse to the incoming ν_μ direction ($\vec{\not{P}}_T$) can be calculated from the reconstructed event. The angles $\phi_{\mu \rm h}$ and $\phi_{\rm mh}$ are then formed between the transverse momentum vectors of the outgoing lepton, the hadron jet and $\vec{\not{P}}_T$. The angle $\phi_{\rm lh}$ is peaked strongly towards 180° in ν_μ^{CC} events, whereas in events from τ decays this correlation is much weaker because of the undetected neutrinos. Similarly, the direction of the $\vec{\not{P}}_T$ vector in ν_μ^{CC}events is determined mainly by resolution and has no specific direction, making the $\phi_{\rm mh}$ distribution rather flat. In contrast, the $\phi_{\rm mh}$ distribution from events with a τ decay peaks towards 180°, reflecting the fact that the τ^- and the jet are produced back-to-back. The separation between signal and background is enhanced by combining these variables in the $\phi_{\rm lh}$-$\phi_{\rm mh}$ plane.

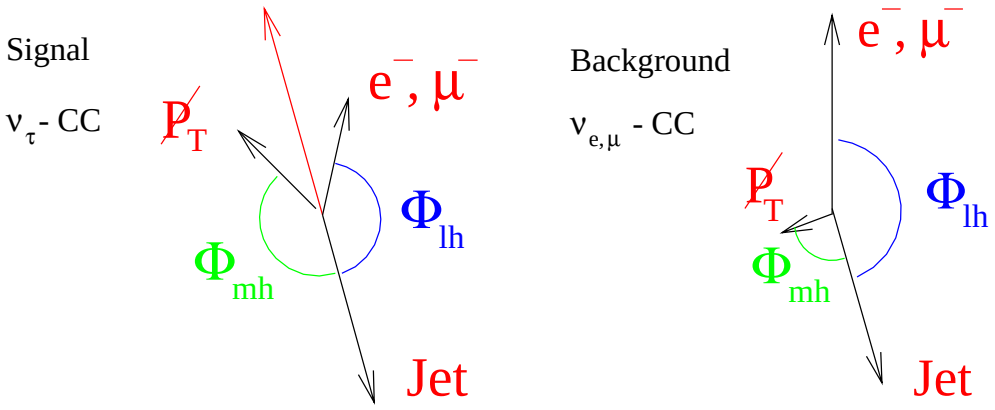

Figure 2.1: *Transverse plane kinematics for signal (left) and charged current background (right).*

Muonic channel

This channel is in direct competition with ν_μ^{CC} interactions. To reject events with a primary μ^- from the scattering process, a tight cut in the $\phi_{\mu\mathrm{h}}$-ϕ_{mh} plane is used. Another contribution to the background arises from π^- and K^- decays in flight in the target region. However, these have a limited transverse momentum Q_T with respect to the total visible event momentum $\vec{P}_{\mathrm{tot}}$:

$$Q_T \equiv \sqrt{\left(\vec{P}_{\mu^-}\right)^2 - \left(\vec{P}_{\mu^-} \cdot \vec{P}_{\mathrm{tot}}\right)^2 / P_{\mathrm{tot}}^2} \tag{2.1}$$

and may be used to reject this background efficiently. The large statistics of ν_μ^{CC} events offers the possibility to study and understand detector and physics effects on the missing transverse momentum resolution and on the oscillation search.

Electronic channel

The advantage of this channel compared to the muonic channel is a much smaller background of the corresponding charged current interaction, since the ν_e content of the beam is only 1% of the ν_μ contribution. Therefore a more relaxed cut in the ϕ_{eh}-ϕ_{mh} plane can be used, yielding a larger efficiency. Besides ν_e^{CC} interactions the following background sources are considered as important:

- γ conversion and Compton scattering
- π^0 and η Dalitz decays with asymmetric electrons (one is lost)
- $\mu^- \rightarrow \mathrm{e}^-\overline{\nu}_\mathrm{e}\nu_\mu$ and $\mathrm{K}^- \rightarrow \mathrm{e}^-\pi^0\nu_\mathrm{e}$ decays

Hadronic channels

In the case of τ hadronic decays, the basic preliminary selection requires events with no identified electron or muon, thus eliminating the bulk of charged current events. Given the large number of ν_μ^{CC} in the data sample, the rejection of this background requires an excellent efficiency for lepton identification. The remaining background are ν_μ^{NC}events where a hadron (or a group of hadrons) in the hadronic jet is taken as a candidate for the τ decay products. The selection in the transverse plane is not efficient in this case, as the background events present a momentum imbalance from the undetected outgoing ν_μ^{NC} neutrino. The main handle is again the perpendicular component of the momentum of the generic hadron candidate h^- with respect to the total visible momentum of the event, Q_T. Since hadrons in the background are produced in the fragmentation of the hit quark and the nuclear remnants, they have a limited transverse momentum, while the hadrons from τ decays are expected to be well separated in space from the hadronic jet, as depicted in Figure 2.2.

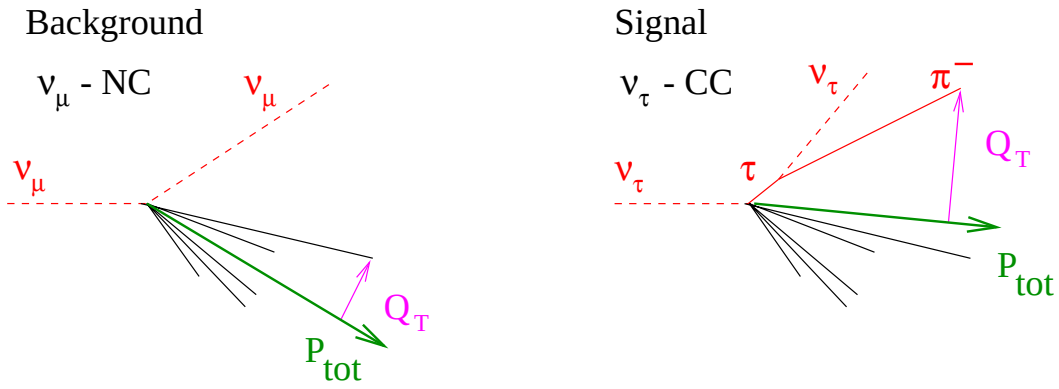

Figure 2.2: *Sketch of the isolation variable Q_T for signal and background.*

2.2 The CERN neutrino beam

The NOMAD detector is located at the CERN West Area Neutrino Facility (WANF) and is exposed to the SPS wide-band beam (WBB) which consists predominantly of ν_μ.

Figure 2.3 shows a schematic layout of the WANF beam line.

The neutrinos are primarily produced from 450 GeV protons impinging on a beryllium target. Two Beam Current Transformers (BCT) and several Secondary Emission Monitors (SEM) are used to measure the proton beam intensity. Protons are extracted from the SPS in two 4 ms long spills separated by a 2.6 s "flat-top" (cf. Figure 2.4). The delivered intensity is $\sim 2.2 \times 10^{13}$ protons on target (*p.o.t.*) per SPS cycle.

The secondary pions and kaons are focussed by a pair of coaxial magnetic lenses, the horn and reflector. In such a system, charged particles are deflected by the toroidal field between two coaxial conductors carrying equal and opposite currents, such that focusing of particles of one sign implies defocusing of particles of the opposite sign. The section between the horn and reflector and that between the reflector and decay tunnel have been equipped with helium tubes to reduce the absorption of secondary particles.

A neutrino beam monitoring system, based on the detection of muon yields at several depths in the iron shield (the "muon pits"), is built into the line. The silicon detectors in these muon pits also provide an independent absolute flux measurement. The absolute calibration of the silicon detectors is performed against emulsion measurements in the pits.

Most of the mesons will decay in a 290 m vacuum tunnel. Shielding made of iron and earth follows to range out muons and stop hadrons. The CHORUS and NOMAD detectors are located at about 823 m and 835 m from the target.

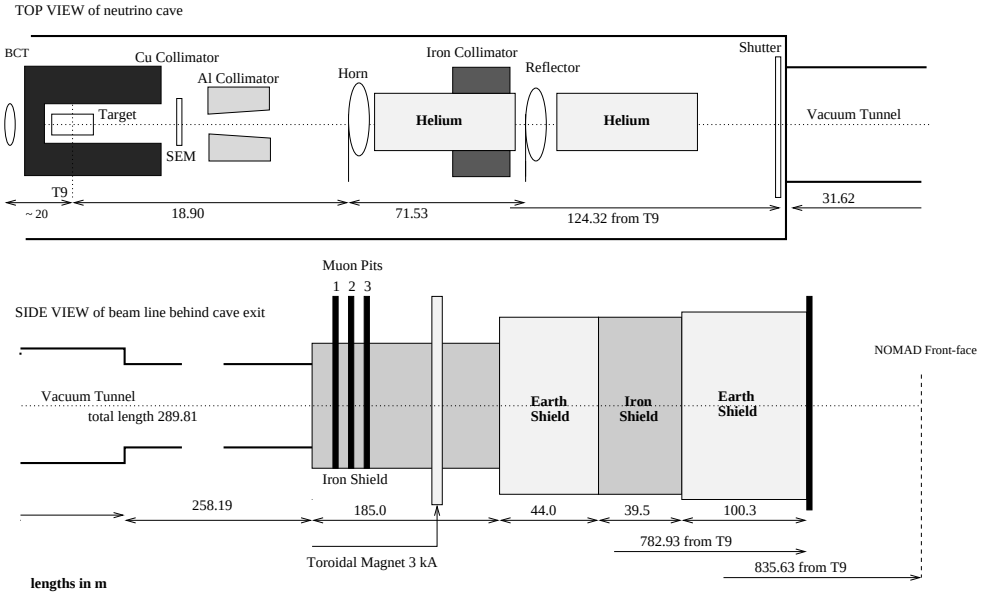

Figure 2.3: *Scheme layout of the WANF beam line pointing out its main elements (not drawn to scale).*

A detailed GEANT [72] simulation of the beam line was used to predict the neutrino energy spectra (Figure 2.5) and radial distributions of the various neutrino types at the NOMAD detector. The parameters of the various neutrino components are summarized in Table 2.2.

The neutrino beam consists predominantly of ν_μ whose parent particles are mostly $\pi^+(E_\nu < 60$ GeV) and $\mathrm{K}^+(E_\nu > 60$ GeV) mesons. This can be seen from

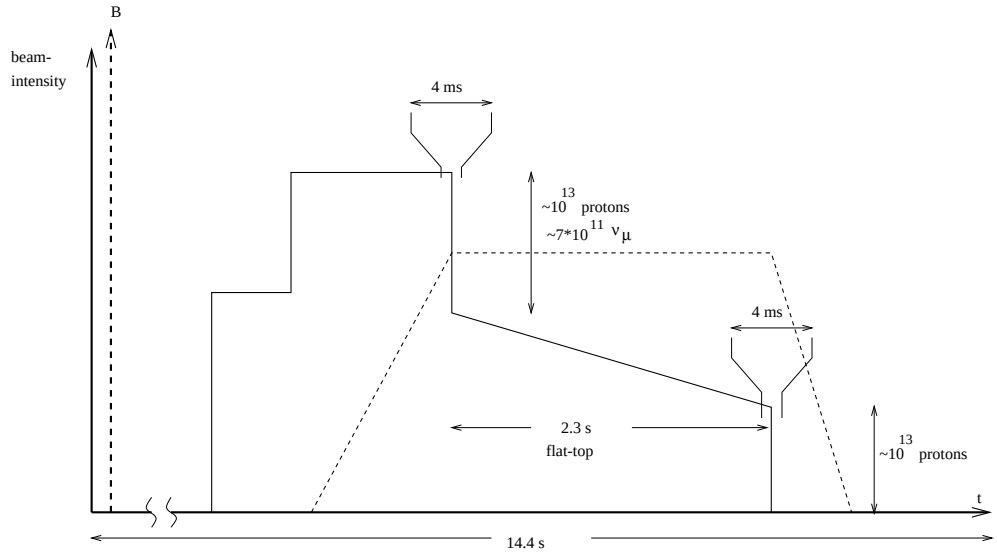

Figure 2.4: *Time structure of the SPS cycle (not drawn to scale).*

the relation between the neutrino and meson energy:

$$E_\nu = E_{\rm meson}\frac{1-\left(\frac{m_\mu}{m_{\rm meson}}\right)^2}{1+\gamma^2\theta^2} \tag{2.2}$$

where θ is the angle of the neutrino *w.r.t.* the beam axis. This shows that the average energy of neutrinos in the center of NOMAD, thus at small θ, is higher than towards the border of the fiducial area of the detector. The maximal possible decay angle $\theta_{\rm max}$ for neutrinos reaching the NOMAD detector is $\sim 1.5/400$. Since $m_{\rm K^+}/m_{\pi^+} \sim 3.5$, neutrinos from $\rm K^+$-decays satisfying the condition of angular acceptance have a higher energy than neutrinos from π^+-decays. The neutrino beam simulation is affected by uncertaincies due mostly to the limited knowledge of the π and K yields from the hadronic interactions in the beryllium target.

The intrinsic ν_τ component in the beam, from the prompt reaction:

$$p + N \rightarrow D_s^\pm + X;\;\; D_s^\pm \rightarrow \tau^\pm + \nu_\tau^{(-)} \tag{2.3}$$

followed by $\tau^\pm \rightarrow \nu_\tau + X$ has been calculated to be negligible [73,74]. The relative number of ν_τ produced from the above reaction and interacting via the CC in the fiducial volume of NOMAD has been calculated to be $(4-5)\times 10^{-6}$ the number of ν_μ^{CC} events. After selection criteria, the resulting intrinsic ν_τ signal is much less than one observed event in the total duration of the NOMAD experiment.

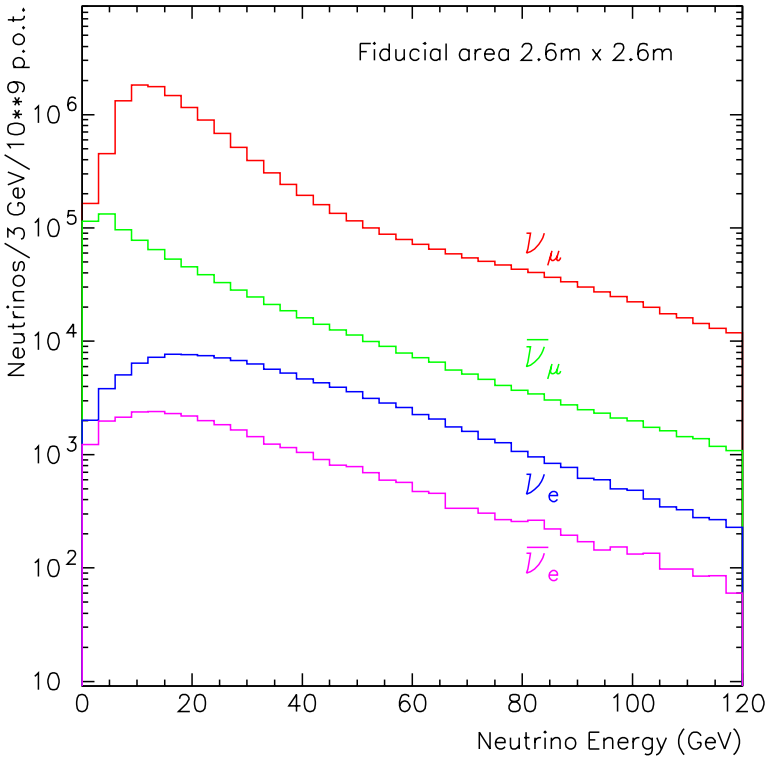

Figure 2.5: *Energy spectra of the different neutrino flavors in the beam, from a MonteCarlo beam simulation.*

Component	$< E_\nu >$ [GeV]	*Relative flux*	# ν^{CC} *events*
ν_μ	23.6	1.00	1.15×10^6
$\overline{\nu}_\mu$	22.7	0.07	0.39×10^5
ν_e	37.0	10^{-2}	0.17×10^5
$\overline{\nu}_e$	33.2	3×10^{-3}	0.22×10^4

Table 2.2: *Predicted flux at NOMAD for a fiducial area of* 2.6×2.6 m^2 *and* 2.4×10^{19} *p.o.t.*

2.3 The NOMAD detector

A detailed description of the NOMAD detector can be found in [75]. Here, only a short description is given.

The neutrino beam traverses the experiment tilted upwards at an angle of 42 mrad, being nominally centered on the back side of the transition radiation detector. The NOMAD coordinate system is defined as:

- z: horizontal projection of the beam direction
- x: dipole field direction (horizontal; left-hand direction if seen along the beam)
- y: vertical (positive upwards)
- origin: the nominal origin of the NOMAD coordinate system is the center of the first drift chamber front face, coinciding with the longitudinal axis of the NOMAD magnet.

It is important to note that the coordinate system for the experimental setup differs from the one used for physics analyses [76]. The detector coordinate system is defined *w.r.t.* the magnet axis (also referred to as Laboratory frame); the physics coordinate system is defined *w.r.t.* the beam axis (also called Beam frame), which is rotated 42.73 mrad relative to the magnet axis.

The magnet

The NOMAD detector uses the dipole magnet from the former UA1 experiment. While the "C"s of this magnet form the magnetic flux return, the end-caps, which have the form of "I"s, serve as support for the central detector. Both these support pillars have been instrumented as iron-scintillator calorimeters. The front "I" forms the front calorimeter and the back pillar forms the hadronic calorimeter.

Veto counters

The veto system consists of an arrangement of 59 scintillation counters covering an area of 5×5 m^2 at the upstream end of the NOMAD detector. 56 of the counters are viewed at both ends by photomultipliers, the remaining 3 have single-ended readout. The counters are arranged in a geometry which provides optimal rejection of charged particles produced upstream of NOMAD, of those produced in neutrino interactions in the iron detector support and of large angle cosmic rays traveling in the same and opposite direction to the neutrino beam. A small part of interactions in the central region and in the upstream part of the magnet can not be vetoed, but can be distinguished from target interactions by the reconstruction of the event vertex position.

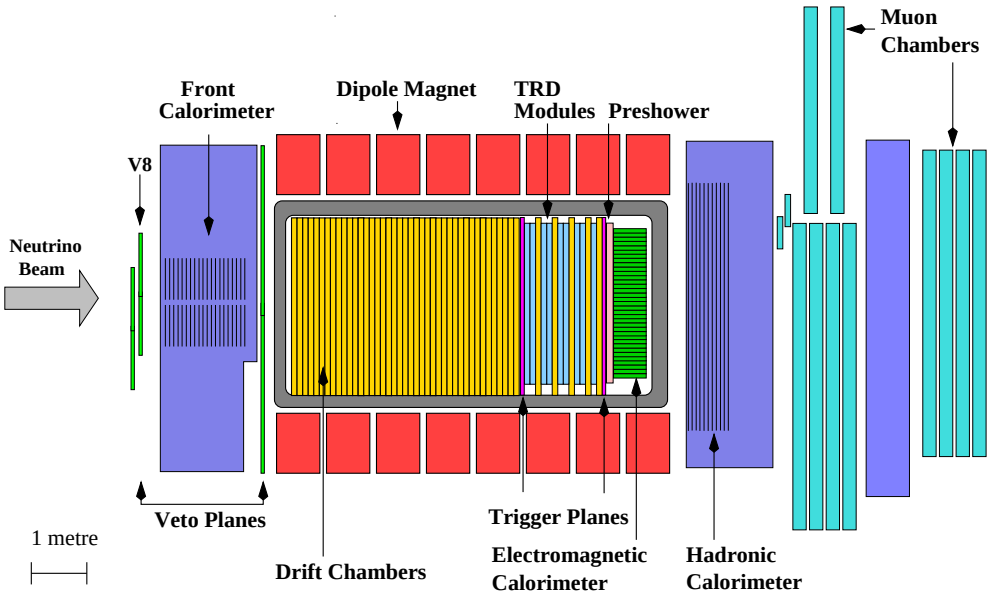

Figure 2.6: *General side view of the NOMAD detector.*

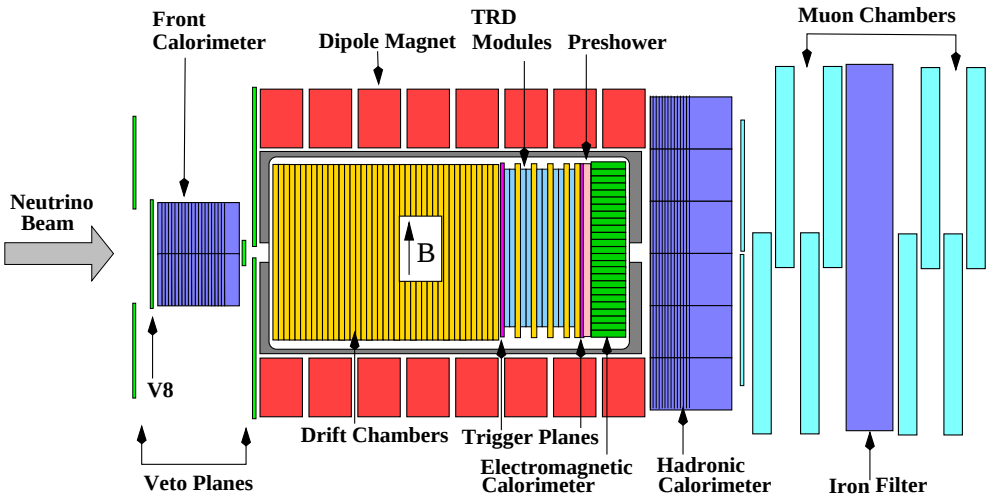

Figure 2.7: *General top view of the NOMAD detector.*

For triggers in the front calorimeter, which instruments the central region of the front detector support, the veto is formed from the subset of ten counters (denoted V_8) mounted on the front face of the support, see Figures 2.6 and 2.7.

The charged particle rejection efficiency of the NOMAD veto is constantly monitored and has remained stable at a level of 96-97%. Averaged over the two neutrino spills, the contribution of the veto system to the overall dead time is 4%.

Front calorimeter

The front part of the magnet return yoke is instrumented as a iron-scintillator hadronic calorimeter (FCAL), using the plate structure of the magnet end-cap pillars. The FCAL consists of 20 iron plates separated by air gaps, which are instrumented with scintillator slabs. Groups of five scintillators are ganged together via adiabatic light guides to form a module, which are read out on both sides by phototubes. Ten such modules are arranged vertically on top of each other to form a stack, of which there are four aligned along the beam axis. The instrumented region has a mass of 17.7 t and is about 5 nuclear interaction lengths deep. Further details on the FCAL can be found in Chapter 3.

Drift chambers

The drift chambers (DC), which provide at the same time the target material and the tracking of particles, are the crucial part of the detector. They were designed with the conflicting requirements that their walls should be as heavy as possible in order to maximize the number of neutrino interactions and as light as possible in order to minimize multiple scattering of particles, secondary particle interactions and photon conversions. To minimize the total number of radiation lengths for a given target mass, the chambers are made of low density and low atomic number materials; there is less than 1% of radiation length between two consecutive measurements.

The transverse dimension of the chambers is approximately 3×3 m^2 and fills completely the available space inside the magnet coil. The total number of chambers in the complete detector is 49, corresponding to 147 sense wire planes. The target chambers are mounted in 11 modules of four chambers; five additional chambers are installed in the TRD region. The fiducial mass of the chambers is 2.4 t over an area of 2.6×2.6 m^2.

The chambers are built on panels made of aramid fibres in a honeycomb structure sandwiched between two kevlar-epoxy resin skins, which give the mechanical rigidity and flatness necessary over the large surface area. Each drift chamber consists of four panels. Three gaps between the panels are filled with an argon (40%) - ethane (60%) mixture at atmospheric pressure. The central gap is equipped with sense wires at 0° and the outer gaps with wires at $+5^\circ$ and -5°

with respect to the magnetic field direction. The potential on the strips provide a drift field of 1 kV/cm. With the electric field and the gas mixture, the ionization electrons drift with a velocity of about 50 mm/μs. The residuals of sample straight tracks at normal incident has a sigma of about 150 μm. The 5° stereo angles give a resolution along the wires of 1.5 mm.

The momentum resolution provided by the drift chambers is a function of momentum and track length; a fit for muons and charged hadrons can be parametrized by:

$$\frac{\sigma_p}{p} \simeq \frac{0.05}{\sqrt{L}} \oplus \frac{0.07p}{\sqrt{L^5}} \tag{2.4}$$

where the momentum p is in GeV/c and the track length L is in m. The first term is the contribution from multiple scattering and the second term comes from the single hit resolution of the chambers. The tracking is much more difficult for electrons as they radiate photons via the bremsstrahlung process as they traverse the non-zero-density tracking system, resulting in a continuously changing curvature. In this case, the resolution is worse and electron energies are measured by combining information from the drift chambers and the electromagnetic calorimeter.

Trigger counters

Two trigger planes are installed inside the magnet volume; the first plane follows the active target and the second is positioned behind the TRD region. Each of them covers a fiducial area of 280×286 cm^2 and consists of 32 horizontally arranged scintillators. To increase the fiducial area of the trigger planes, four additional counters are installed vertically to cover the lightguides of the horizontal counters.

The scintillators are connected by adiabatic lightguides to photomultipliers of the proximity mesh type, which are oriented parallel to the magnetic field. The field of 0.4 T only reduces the photomultiplier response by 30%. They have an intrinsic time resolution of 1 ns and a noise rate of less than 50 Hz.

The average efficiency of the trigger counters for single tracks has been determined with data and measured to be $(97.5 \pm 0.1)\%$.

A more detailed description may be found in [77, 78].

Transition radiation detector

The transition radiation detector (TRD) has been designed to separate electron and pion tracks with a rejection factor greater than 10^3 for a 90% electron efficiency. This factor, together with the additional rejection provided by the preshower and electromagnetic calorimeter, is needed to eliminate the

expected neutral current background events in the oscillation search for the $\tau^- \to e^- \overline{\nu}_e \nu_\tau$ channel, in which an isolated pion track may fake an electron.

The large rejection factor required and the dimensions of the target (3×3 m^2) make the NOMAD TRD one of the largest transition radiation detectors ever built. It is located after the first trigger plane and consists of 9 identical modules. Each of them includes a radiator followed by a detection plane. The first 8 TRD modules are paired into 4 doublets. Five drift chambers are embedded, one after each TRD doublet and one after the last TRD module, in order to provide a precise track extrapolation from the drift chamber target to the electromagnetic calorimeter.

The design of each module is:

- The radiator is a set of 315 polypropylene foils, each 15 μm thick and 2.85×2.85 m^2 in area, separated by 250 μm air gaps.

- The detection plane consists of 176 vertical straw tubes, each 3 m long and 16 mm in diameter, separated by 0.2 mm. The straw tubes are fed with a mixture of 80% xenon - 20% methane gas mixture.

The signals from the 1584 straw tubes working in proportional mode are fed into preamplifiers followowd by differential drivers and charge ADCs.

Electron identification in the TRD is based on the difference in the total energies deposited in the straw tubes by particles of different Lorentz factors ($\gamma = E/mc^2$). Charged particles with $\gamma < 500$ deposit energy predominantly by ionization losses, whereas charge particles with $\gamma > 500$ (mainly electrons in NOMAD) also produce transition radiation X-rays at the interfaces of the foils. As a result, a few photons in the keV range are produced by an electron crossing a radiator. About 60% of the photons emitted from the radiator are absorbed in the detection planes. Transition radiation X-ray energy deposition is added to the ionization losses of the parent particle in the same straw tube, because the angular distribution of emitted photons peaks around the initial particle direction (the mean angle of emission is about $1/\gamma$).

The algorithm developed for electron identification is based on a likelihood ratio method and relies on test beam measurements and detector simulation. A pion rejection factor greater than 1000 is obtained with the 9 TRD modules in the momentum range from 1 to 50 GeV/c, while retaining an electron efficiency of 90%.

Preshower detector

The preshower (PRS), which is located just in front of the electromagnetic calorimeter, is composed of two planes of proportional tubes (286 horizontal and 288 vertical) preceded by a 9 mm (1.6 X_0) lead-antimony ($96\% - 4\%$) converter.

Signals from each tube are fed into charge preamplifiers; at the output of the preamplifier, two pulses of opposite polarity are sent via Delaying and Pulse Shaping Amplifiers (DPSA) to charge sensitive ADCs.

With the preshower alone, a resulting π contamination of less than 10% can be obtained for an electron efficiency of 90% at energies above 4 GeV. The π/e separation can be substantially improved by using the PRS in combination with the electromagnetic calorimeter. Test beam measurements with pion and electron beams show that a rejection factor between $3 \cdot 10^{-4}$ (at energies greater than 10 GeV) and 10^{-2} (at about 1 GeV) may be achieved with 90% electron acceptance. Especially, the fine granularity of the preshower assists the separation of overlapping clusters in the electromagnetic calorimeter caused by adjacent particles.

Electromagnetic calorimeter

The search of ν_τ events in NOMAD relies strongly on a very accurate determination of the total transverse momentum in the event as well on electron identification. The electromagnetic calorimeter (ECAL) is crucial to accurately measure electron and gamma energies from 100 MeV up to 100 GeV. The large energy range to be covered requires a large dynamic range in the response of the detector and of the associated electronics. The ECAL combined with the PRS is also used to help improving the electron identification provided by the TRD.

ECAL consists of 875 lead-glass Čerenkov counters arranged in a matrix of 35 rows and 25 columns. Each counter is a 19 radiation lengths deep block with a rectangular cross-section of 79×112 mm^2. Light detectors (two stage photomultipliers, tetrodes) are coupled at the back end face of the blocks. This face is cut at 45° with respect to the block axis, in such a way that the symmetry axis of the tetrodes forms an angle of 45° with respect to the field direction, thus keeping the signal reduction caused by the magnetic field to less than 20%. A low-noise electronic chain, composed of charge preamplifiers followed by a shaper and a peak sensing ADC provides a calorimeter response in a dynamic range larger than 4×10^3. An additional fast analog signal chain provides time measurements with a resolution of a few ns used to reject energy depositions not associated with the triggering event and to form an ECAL trigger, as explained in Section 2.3.

The linearity of the calorimeter response to electrons was verified with a test beam in the energy range $1.5 - 80$ GeV; deviations from linearity are less than 1.5%. The energy resolution was measured to be

$$\frac{\sigma_E}{E} \simeq \frac{(3.22 \pm 0.07)\%}{\sqrt{E(\mathrm{GeV})}} \oplus (1.04 \pm 0.01)\% \qquad (2.5)$$

Hadronic calorimeter

The hadron calorimeter (HCAL) is intended to detect neutral hadrons and to provide a measurement of charged hadrons complementary to that derived from momentum measurements in the drift chambers. Knowledge of neutral hadrons is important when constructing kinematic quantities such as missing transverse momentum, and calorimetric measurements of charged particles can be used both as consistency check and as an aid in distinguishing muons from charged hadrons.

To construct the HCAL, the downstream support pillar of the magnet basket is instrumented as an iron-scintillator sampling calorimeter similar to the FCAL. 23 iron plates 4.9 cm thick separated by 1.8 cm gaps form a wall of 5.4 m width, 5.8 m height and 1.5 m depth, acting as a filter for the large muon chambers downstream.

The active elements of the calorimeter are scintillator paddles 3.6 m long, 1 cm thick and (on average) 18.3 cm wide. Tapered acrylic light pipes are glued to each end to form an assembly 5.52 m long. Eleven of these assemblies are threaded horizontally through the first 11 gaps to form a calorimeter module of approximately 3.1 interaction lengths ($\lambda_{\rm int}$). Scintillation light is directed through adiabatic light guides to 5 inch phototubes at each side of the module. Eighteen such modules stacked vertically form an active area 3.6 m wide by 3.5 m high.

The energy deposited in a given module is obtained from the geometric mean of the two phototube signals, and the horizontal position of the energy deposit is determined from the attenuation length of the scintillator and the ratio of the phototube signals. Vertical positions are determined from the pattern of energy sharing between the modules.

There is a high probability that hadrons will begin to shower in the approximately 2.1 $\lambda_{\rm int}$ of material upstream of the hadron calorimeter, and so the total hadronic energy is taken to be a weighted sum of the energies deposited in the hadron and electromagnetic calorimeters.

Muon chambers

The muon detector consists of 10 drift chambers previously used in the UA1 experiment. Each chamber has an active area of 3.75×5.55 m^2 with two planes of drift tubes in the horizontal and two in the vertical directions. In total there are 1210 drift tubes, each with a minimum drift distance of 7 cm.

The chambers are arranged in pairs (modules) for track segment reconstruction. The first muon station consists of three modules and is placed behind the hadron calorimeter. It is followed by an 80 cm thick iron absorber and a second muon station of two modules. In 1995 there was a small gap between the chambers of station 2 which was closed with several scintillation counters, the "muon veto", in the beginning of the 1996 run.

Track segments are reconstructed separately for each station from (typically) 3 or 4 hits per projection with a measured efficiency of 97%.

The chambers are operated with an argon/ethane (40%/60%) gas mixture. Their performance was monitored continuously using high energy muons passing the detector. The average position resolution for hits is in the range $350-600$ μm depending on the gas quality.

The average hit efficiency is 92.5% and the dominant source of inefficiency (6.5%) is due to dead areas between the drift tubes.

Triggering

The trigger logic is performed by a especially designed MOTRINO module [77,78], providing the following functionalities:

- Generation of timing signals to synchronize with the SPS beam cycle.
- Combination of subdetector signals for trigger formation.
- Storing of trigger times relative to the SPS cycle.
- Recording of the status of the different triggers. The information is stored as soon as the first trigger fires and again 200 ns later, to record any additional trigger condition set.
- Determination of the lifetimes for the various trigger types.
- Moderation of trigger rates.

Triggers were set up for the study of neutrino interactions. In addition to the approximately 15 neutrino events per spill, various triggers are setup in the muon flat-top, where about 60 triggers are taken and about 20 are written to tape.

Neutrino triggers

- $\overline{V} \times T_1 \times T_2$: The trigger allows to study neutrino interactions in the drift chamber target region. At least one hit in both trigger planes T_1 and T_2 is required. To prevent triggering on through-going muons, no hit should have occurred in the veto counters V. The rate for this trigger is $\simeq 5.0/10^{13}$ $p.o.t.$ and the lifetime is $(86 \pm 4)\%$. Of these triggers, about 0.5 are potentially interesting neutrino interaction candidates. The remaining consist of "cosmics", non-vetoed muons and neutrino interactions in the magnet.
- $\overline{V}_8 \times$ FCAL: An energy deposit of at least 4 $m.i.p.$[1] in the FCAL fires this trigger. Through-going muons are vetoed by the veto subset V_8. On average

[1] **m**inimum **i**onizing **p**article

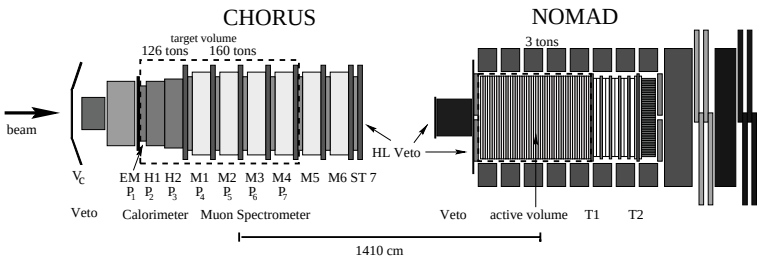

Figure 2.8: *Setup of the CHORUS-NOMAD neutral heavy particle trigger .*

6.5 neutrino interactions occur in the FCAL for 10^{13} *p.o.t.* and the lifetime is $(90 \pm 3)\%$.

- $\overline{V}_8 \times \mathrm{FCAL}' \times T_1 \times T_2$: With this trigger it is possible to study quasielastic like events in the FCAL, allowing a relative flux measurement of the beam as a function of neutrino energy. An energy deposition between 1 and 3 *m.i.p.* in the FCAL is required for this trigger, with a rate of $\simeq 1.5/10^{13}$ *p.o.t.* and a lifetime of $(90 \pm 3)\%$.

- $\overline{T_1 \times T_2} \times \mathrm{ECAL}$: Using the ECAL as a target, physics topics such as $\nu_\mu \leftrightarrow \nu_e$ and $\nu_\mu \leftrightarrow \nu_\tau$ oscillations may be addressed. An energy deposit of more than $\simeq 1$ GeV in the ECAL enables this trigger, which has an average rate of $\simeq 2/10^{13}$ *p.o.t.* and a lifetime of $(88 \pm 3)\%$.

- $\overline{V}_C \times \sum_{i=1}^{6} M_i \times \overline{ST}_7 \times \overline{V}_N \times T_1 \times T_2$: Motivated by the search for neutral heavy particles a joint trigger with the CHORUS experiment, situated upstream of NOMAD, has been set up in 1996 [79]. Both experiments are recording simultaneous interactions in the CHORUS spectrometer and the NOMAD drift chambers. Such a configuration corresponds to the signature of a hypothetical neutral heavy particle produced in CHORUS and decaying in NOMAD. Figure 2.8 shows the various subdetectors used to form this trigger.

Muon triggers

- $V \times T_1 \times T_2$: Covering the full fiducial area, this trigger is used for drift chamber alignment and calibration of the different subdetectors with minimum ionizing particles.

- $V_8 \times T_1 \times T_2 \times \mathrm{FCAL}'$: This trigger was implemented to enhance the sample of muons traversing the FCAL, used for detector calibration.

- $V_8 \times T_1$: With this trigger the efficiency of the trigger plane T_2 is measured.

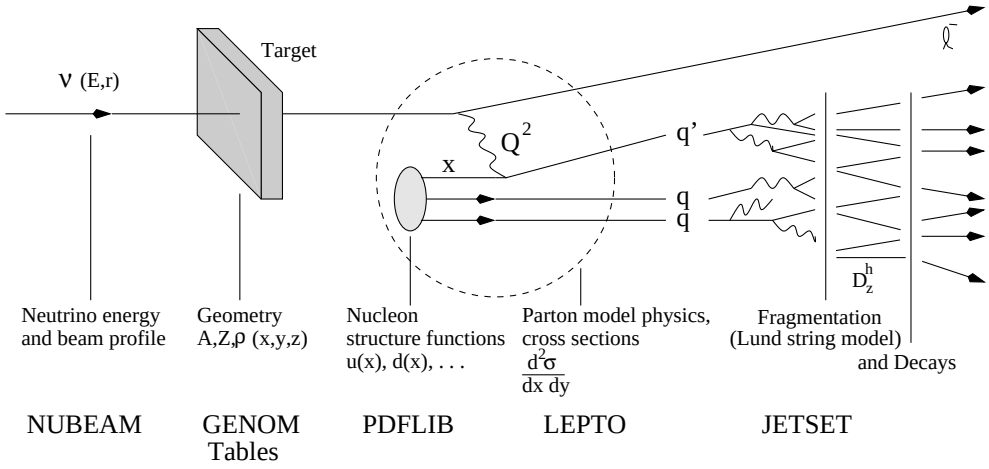

Figure 2.9: *Overview of the various packages used in NEGLIB for the simulation of the physics process* $\nu + \mathcal{N} \rightarrow l + X$.

- $V_8 \times T_2$: This trigger allows to measure the efficiency of T_1.
- $V \times T_1 \times T_2 \times \text{ECAL} \times \overline{\text{HCAL}}$: A proper understanding of the behavior of electrons in NOMAD is crucial for the oscillation search. This trigger allows to select and study electrons from muon decay or delta rays. Since the threshold for the ECAL is too low to exclude triggering on muons, HCAL is put in anti-coincidence.

2.4 Software environment

Beam simulation

NUBEAM [80] is a *MonteCarlo* program using the GEANT [72] framework to simulate the present WANF beam line and processes leading to the generation of neutrinos. The proton-beryllium collisions and hadronic interactions which follow were simulated using the FLUKA92 package [81], which is available in a version interfaced to GEANT. The simulated neutrino beam compositions together with the predicted fluxes are shown in Figure 2.5 and in Table 2.2.

Neutrino Event Generation

The NOMAD Event Generator LIBrary (NEGLIB) [82] offers all the needed flexibility to generate neutrino interactions in the NOMAD detector. In order to describe the physics process $\nu + N \rightarrow l + X$ correctly, various packages are used. Their interplay is depicted in Figure 2.9.

The kinematics for deep inelastic neutrino-nucleon scattering are simulated with the LEPTO [83] package. It is based on the leading order electroweak cross-sections for the parton level scattering processes. The fragmentation of produced partons into observable hadrons is performed with the Lund string model [84], implemented in JETSET [85]. For the parton density distributions the GRV-HO [86] parameterization is used, which is available in the PDFLIB [87].

In case of ν_τ^{CC} interactions, the τ-decays are simulated with the KORALZ [88, 89] package which contains TAUOLA [90, 91].

Detector simulation

The propagation of particles produced in neutrino events and their interactions in the detector is simulated using the environment of the GEant NOMad library (GENOM) [92], which is a detector simulation based on GEANT [72]. It contains a detailed description of the detector geometry, records particle trajectories through the experimental setup and simulates the response of the sensitive detector parts. Events simulated with GENOM can subsequently be passed through the normal reconstruction and selection programs as if they were real data.

Chapter 3

The Front Calorimeter

In Chapter 2 the Front Calorimeter (FCAL) [67] of the NOMAD experiment has been introduced. In this chapter the motivations for its construction are outlined and a detailed description of its components is given. A method for the energy calibration is provided, similar to the ones in [93] and [94].

3.1 Motivation for the construction of the FCAL

The NOMAD detector was designed for the search of neutrino oscillations. However, the intense neutrino beam at CERN and the FCAL as an instrumented heavy target detector provide a high statistic of neutrino induced events. In combination with the proper NOMAD detector, immediately downstream of the FCAL, as a high precision tracking device, the possibility is provided to study other interesting topics in neutrino physics:

- **Opposite-Sign Dimuons** (OSDM)

  Events with the emission of two oppositely charged muons appear in neutrino induced charm production and the subsequent decay of the charmed meson in a muon:

$$\nu_\mu + \begin{pmatrix} s \\ d \end{pmatrix} \rightarrow \mu^- + c \hookrightarrow s + \mu^+ + \nu_\mu$$

  The corresponding $\overline{\nu}_\mu$ process has the s, d and c quarks replaced by their anti-quark partners and oppositely charged muons. Its distinct experimental signature is the presence of opposite sign dimuons in the final state: one associated with the incoming neutrino, and the other with the decay of the charm-quark. This process may be used to investigate the mass of the

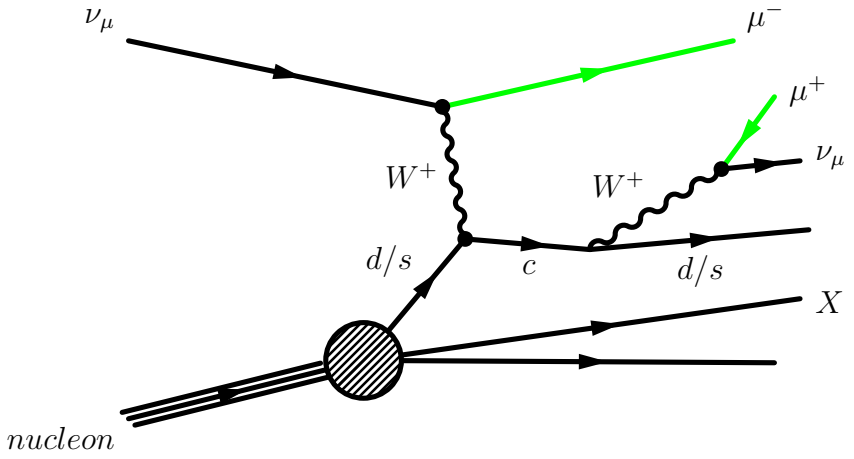

Figure 3.1: *OSDM production process.*

charm-quark m_c, the coupling V_{cd} of the CKM-matrix and the strange quark contents of the nucleon. Analyses have been performed in [95–98].

- **Like-Sign Dimuons** (LSDM)

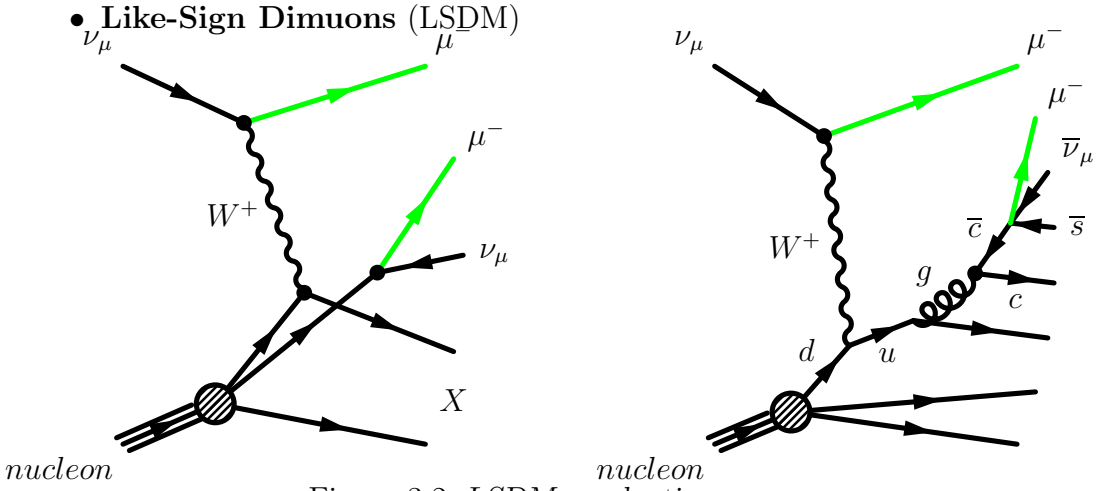

Figure 3.2: *LSDM production process.*

The occurrence of events with two muons of same charge is mainly due to π^-/K^- decay or processes involving $\overline{c}$-production. The CCFR collaboration has studied these events, finding a small excess of events [99]. The expected number of FCAL events should be an order of magnitude larger than obtained to date.

- **Trimuons**

Trimuons are typically standard charge current events accompanied by two extra, oppositely charged muons, which come about either from the hadronic continuum, or the decay of discrete vector bosons, such as $\rho - \omega$, J/ψ, or a hard muon bremsstrahlung where the photon creates the two extra muons. A trimuon search is currently under way [100].

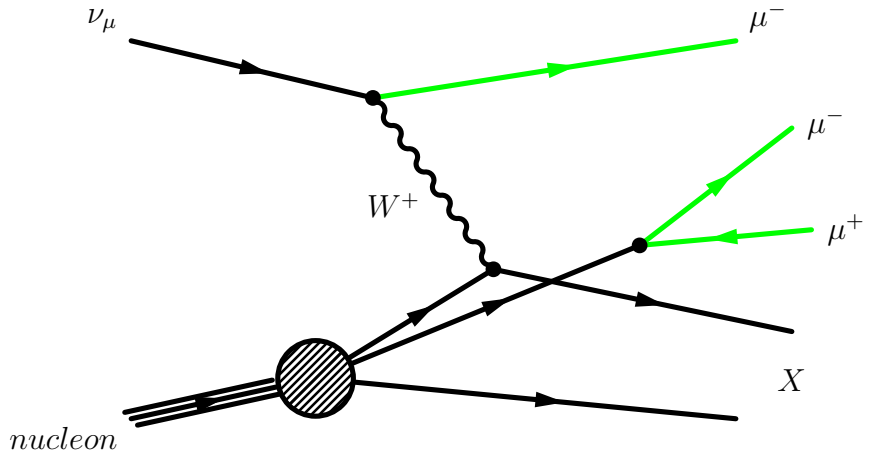

Figure 3.3: *Trimuon production process.*

- **Trident production**

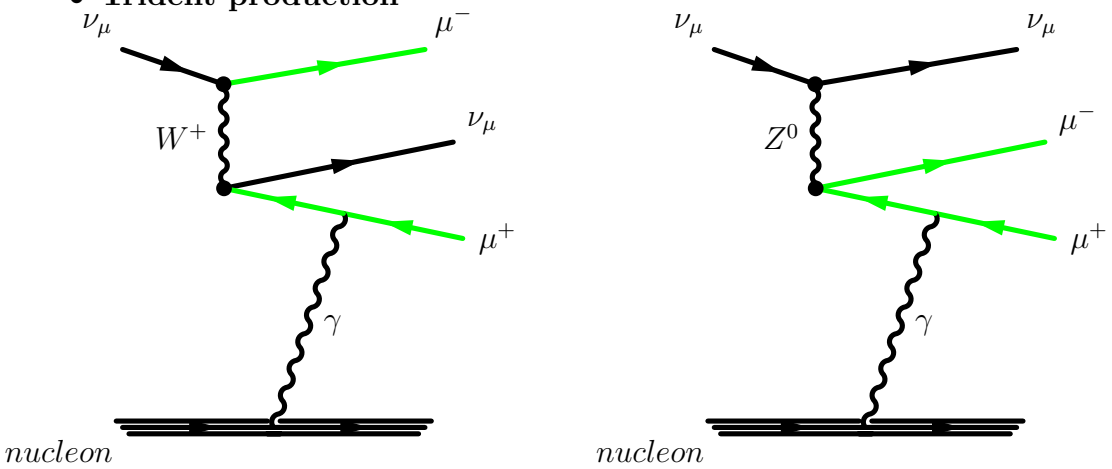

Figure 3.4: *Trident production process.*

The so-called Trident production process is the elastic scattering of a neutrino off the Coulomb field of a nucleus. The resulting W or Z boson decays in the muonic channel and the decay products are brought onto mass-shell by the exchange of a virtual photon with the nucleon field. Magnitude and sign of the interfering neutral and charged current processes (see Figure 3.4) are predicted by the Standard Model, so a measurement of the cross-section provides a test of the Lorentz structure of the electroweak current and the Weinberg angle. The CCFR collaboration has reported the observation of destructive interference in the tridents [101]. The CCFR data, however, are statistically small and NOMAD may be able to improve the measurement by an order of magnitude in statistics.

- **J/ψ in neutrino neutral current events**

Consider a neutrino induced process depicted in Figure 3.5: a Z^0-gluon

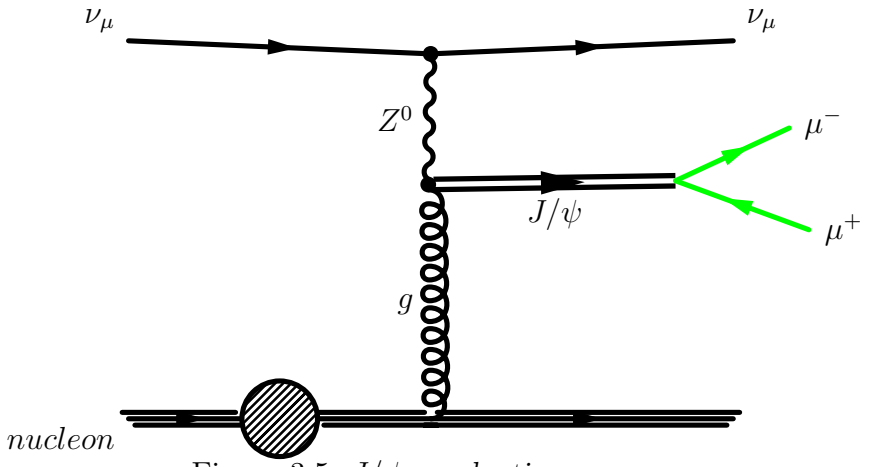

Figure 3.5: *J/ψ production process.*

fusion where the J/ψ decays into a pair of muons. The CDHS experiment is the only that has reported such an event at about 3σ level [102] and the combination NOMAD-FCAL may be able to establish and improve the measurement. An analysis is currently conducted [103].

- **Neutral Heavy Lepton Search**

  The existence of neutral heavy leptons coupling with Standard Model neutrinos is predicted in many extensions of the Standard Model. A search for neutral heavy leptons produced in the FCAL and decaying in the NOMAD active volume, already discussed in Chapter 1, is the subject of this thesis and will be considered further in the analysis chapters.

- **Beam studies**

  The large data sample of FCAL events permits detailed studies of the features of the neutrino beam, e.g. anti-neutrino content, radial distribution and energy spectrum [80].

3.2 Description of the FCAL

3.2.1 The Front "I"

The Front-"I" consists of 23 iron plates, each having a thickness of 4.9 cm, separated by 1.8 cm air gaps. The first 20 gaps (as counted from the most upstream plate) are instrumented with scintillator slabs of 18.5 cm height, 185 cm width and 0.5 cm thickness. The last three gaps are not instrumented as they are occupied by structural elements of the "I". To achieve optimal light collection and a reasonable number of read-out channels, groups of 5 scintillators along the beam axis are ganged together by twisted adiabatic light guides and form a module.

Each module is read out on both sides by 3−inch phototubes, allowing the reconstruction of the x-coordinate of the hadronic shower by signal sharing between the left and right read-out channels as well as the determination of signal timing. 10 such modules are arranged vertically on top of each other, separated by a 4.4 cm wide strip, due to structural elements in the gap, between the lower and upper 5 modules. Along the beam axis there are four such stacks. The instrumented region covers an area of 175×190 cm^2 and a depth of 134 cm corresponding to about 5 nuclear interaction lengths, resulting in a total target mass of 17.7 t.

The stacks are numbered from 1 to 4 starting at the most upstream stack. The modules within each stack are numbered from 0 to 9 beginning at the bottom module. For each module the photomultipliers are labelled by 1 (left) and 2 (right) *w.r.t.* the beam. Each module has a unique identification label based on the formula:

$$\text{module} = 100 \times \text{stack} + 10 \times (\text{module number within the stack}) \tag{3.1}$$

Figures 3.6, 3.7 and 3.8 show the different schematic views of the FCAL.

3.2.2 The Scintillators

The scintillators used in the FCAL are organic plastic scintillators, previously used in the CDHS experiment [104]. An extract of their specifications is presented in Table 3.1.

Energy deposited by charged particles traversing a scintillator is converted into light. The average number of photons is proportional to the amount of deposited energy and follows the Poisson distribution. To detect particles the scintillator light is collected and measured by optical receivers. Taking into account light absorption by the scintillator volume and by reflections on the scintillator surfaces, the scintillator may be characterized by a attenuation length λ, describing an exponential light attenuation.

The attenuation length of each scintillator slab was measured using an ultraviolet light source and three pin diode detectors [94] and scintillators were grouped to modules having similar attenuation lengths.

3.2.3 The Photomultipliers

Each FCAL module is read out on both sides by photomultpliers, also recycled from the CDHS experiment. Specifications of the used photomultiplier tubes are listed in Table 3.2. In CDHS on each photomultiplier a yellow Kodak Wratten 2E filter was glued, absorbing light with wavelengths > 430 nm, the part of the spectrum absorbed in the scintillator. The result is a uniform light measurement, i.e. independent of the position a particle traverses the scintillator. The

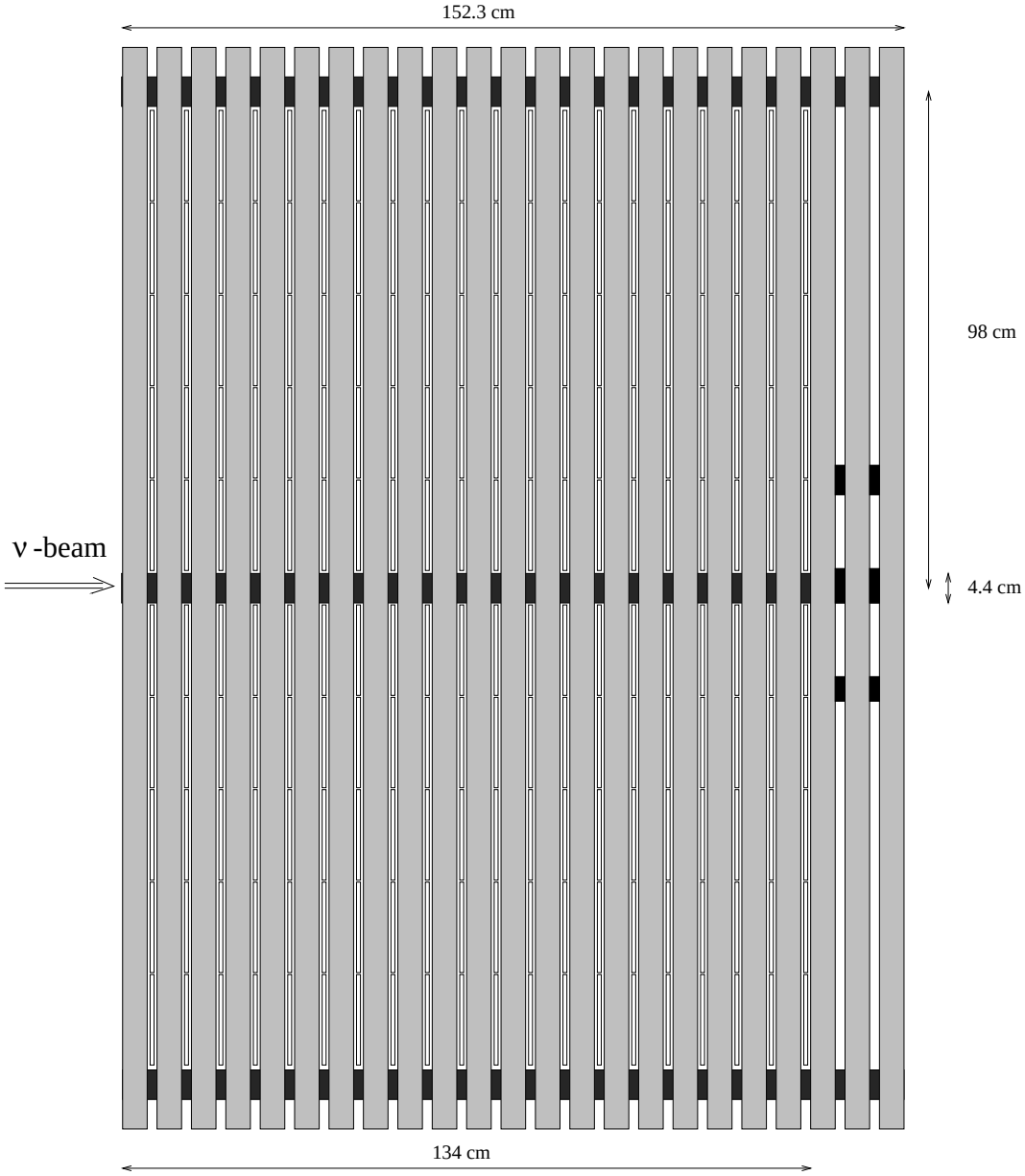

Figure 3.6: *Side view of the FCAL.*

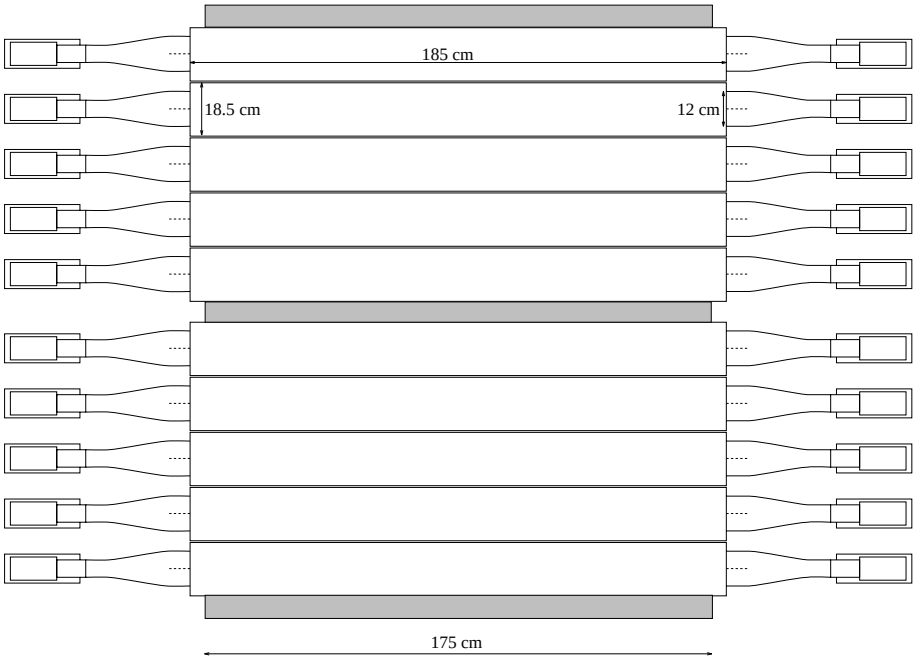

Figure 3.7: *Front view of the FCAL.*

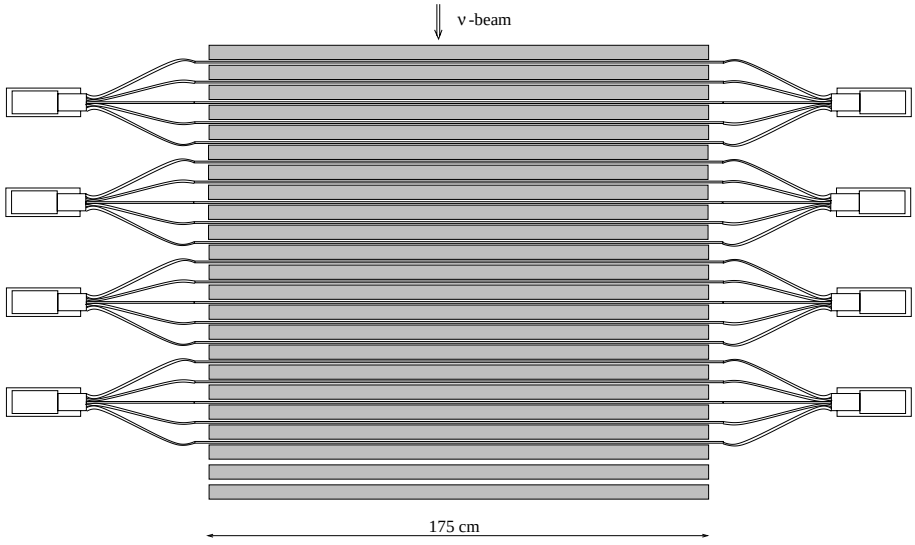

Figure 3.8: *Top view of the FCAL.*

type	NE102A
length	175 cm
width	18.5 cm
thickness	0.5 cm
wavelength of max. emission	423 nm
density	1.032 g/cm^3
refractive index	1.580
attenuation length	$\simeq$ 150 cm

Table 3.1: *Specifications of FCAL scintillators.*

FCAL should be used for position measurement using light attenuation. Because the filters could not be removed, a study of the position resolution must show that the required resolution can be achieved. The absolute gain of each photomultiplier was determined by measuring the pulse height spectra as a function of the input supply voltage [94].

type	SRC GT75B01
diameter of phototube	3 inches
diameter of photocathode	2.6 inches
cathode material	semi-transparent $Cs-K-Sb$
wavelength of max. response	(400 ± 50) nm
quantum efficiency	22%
# of dynode stages	10
max. supply voltage	2.25 kV
current amplification @ 1.5 kV DC	4.5×10^5

Table 3.2: *Specifications of FCAL photomultipliers.*

3.2.4 Readout electronics

Figure 3.9 shows the schematics of the FCAL readout electronics. The signals from the photomultipliers are amplified and divided into three different channels using custom-designed active pulse splitters [94].

- **Energy measurement**: The photomultiplier signal is delayed by passive analog delay lines of type SECRE DPI S14 in order to be in-time with the NOMAD data acquisition system, performing the readout about 400 ns after the interaction has occurred. The delay lines conserve the total charge of the pulse but distort the pulse shape. The signals are recorded by custom-made charge-integrating *ADCs* with 100 ns gate with and 12-bit dynamic

range of 1024 pC. A *MonteCarlo* simulation of neutrino interaction showed that less than 1% of the modules hit see an energy equivalent of more than 70 $m.i.p.$. Correspondingly, the amplification was chosen to yield an equivalent of the $m.i.p.$ energy of $\simeq 50$ ADC counts. Assuming a pedestal value of 250 ADC counts and a hadronic energy equivalent of 0.5 GeV/$m.i.p.$ each module has a dynamical energy range of $\simeq 70$ $m.i.p.$ or 35 GeV.

- **Time measurement**: The second signal line is discriminated by standard LeCroy CAMAC Type 4413 discriminators with a low threshold of 15 mV and sent to TDC modules of type LeCroy type 1876 Model 100. These store the information of 16 signals within 64 μs with a resolution of 1 ns.

- **Trigger formation**: To build the FCAL trigger the signals from the photomultipliers in each stack and on each side are summed inside the splitter box to form two signals per stack:

$$L_i \equiv \sum_{j=0}^{9} L_{ij} \qquad R_i \equiv \sum_{j=0}^{9} R_{ij} \qquad i = 1, \ldots, 4. \tag{3.2}$$

A linear fan-in builds the analog sum to form one signal per stack which are then discriminated at two different threshold levels

$$F_i \equiv (L_i + R_i) > U_{\text{thresh}} \qquad i = 1, \ldots, 4 \tag{3.3}$$

used to form the two FCAL triggers by a logical OR of the 4 stacks:

$$\text{FCAL} \equiv (F_1 \vee F_2 \vee F_3 \vee F_4). \tag{3.4}$$

To build the FCAL trigger an anti-coincidence with the veto subset V_8 is required:

$$\overline{V}_8 \times \text{FCAL} \equiv FCAL \tag{3.5}$$

The threshold used for this trigger is $U_{\text{thresh}} = 75$ mV. A second trigger signal FCAL$'$ is formed with the two trigger planes:

$$\overline{V}_8 \times \text{FCAL}' \times T_1 \times T_2 \equiv FCAL', \tag{3.6}$$

where $U_{\text{thresh}} = 15$ mV. With this trigger it is possible to select muons from quasielastic interactions. The signal ($V_8 \times$ FCAL$'$) is delayed by 70 ns to synchronize it with ($T_1 \times T_2$). Muons from inelastic interactions can be distinguished from those from quasielastic interactions by their timing: the trigger ($\overline{V}_8 \times \text{FCAL}' \times T_1 \times T_2$) is fired also by muons from quasielastic processes but the trigger signal ($\overline{V}_8 \times$ FCAL) is generated before. The right-hand side in the two FCAL trigger definitions gives a short-hand notation which will be used further on.

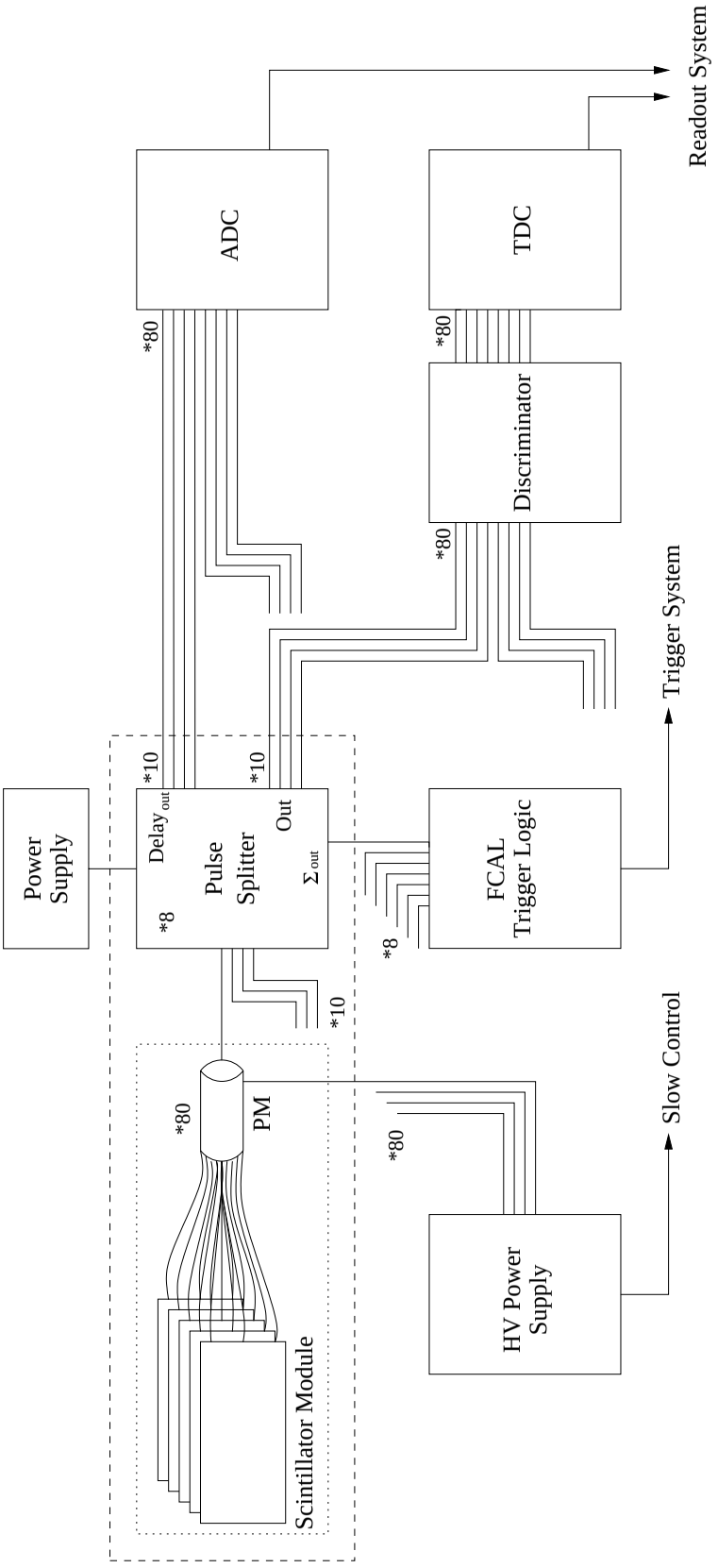

Figure 3.9: *Schematic of the FCAL readout system.*

3.3 Calibration

Because FCAL is part of the structural elements of the NOMAD detector, it is not possible to perform an energy calibration by use of a hadron test beam with know energy. Furthermore, neutrino interactions occur uniformly distributed in its depth, whereas test beam particle interactions would start predominantly at the front face of the FCAL. It would not be possible to determine a position dependence of the calibration constants, e.g. introduced through leakage effects, with a test beam. Therefore a different calibration scheme was used:

- **Relative calibration**: Charged particles passing through FCAL interacting with molecules in the scintillators deposit an energy which, in first order, does not depend on particle type and energy. A module-to-module relative response to the (almost) constant energy deposition of minimum ionizing particles ($m.i.p.$) measures the deposition of the same amount of energy by $m.i.p.$'s in units of ADC counts for each module.
- **Absolute calibration**: The amount of energy deposited by hadronic showers in units of $m.i.p.$'s has to be converted to an equivalent absolute energy. This conversion factor can, as a first estimate, be determined from *Monte-Carlo* studies.

3.3.1 Relative calibration

The response of a FCAL module may be described by three parameters: the attenuation length λ and the gains of the photomultipliers at each end of the module, α_L and α_R. For an energy deposition $E(\mathrm{GeV})$ at a given position x from the center of a counter of length l (see Figure 3.10), assuming exponential light absorption, the number of ADC counts measured at each end of the module may be written as:

$$ADC_L = \alpha_L \cdot E \cdot \exp\left(-\frac{l/2 - x}{\lambda}\right) \tag{3.7}$$

$$ADC_R = \alpha_R \cdot E \cdot \exp\left(-\frac{l/2 + x}{\lambda}\right) \tag{3.8}$$

It's useful to define the following constants:

$$\alpha \equiv \sqrt{\alpha_L \cdot \alpha_R} \cdot \exp\left(-\frac{l}{2\lambda}\right) \tag{3.9}$$

$$\beta \equiv \alpha_L/\alpha_R \tag{3.10}$$

and the quantities:

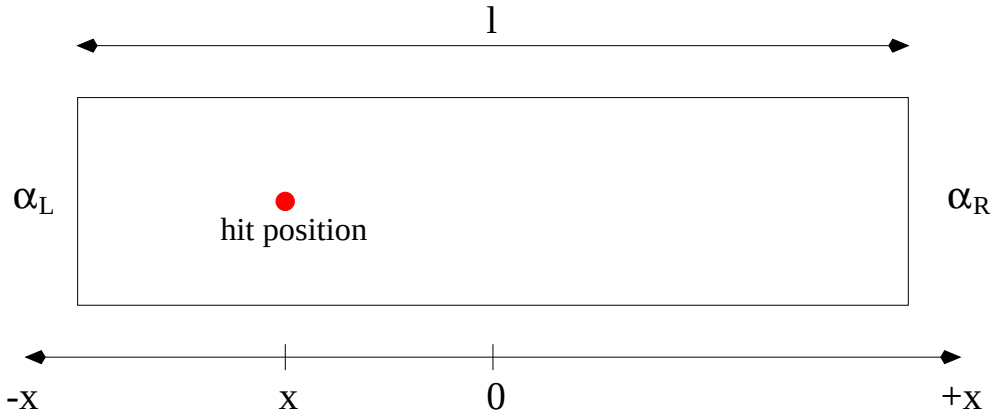

Figure 3.10: *Definition of the readout geometry of the FCAL.*

$$M \equiv \sqrt{ADC_L \cdot ADC_R} = \alpha \cdot E \tag{3.11}$$

$$R \equiv ADC_L/ADC_R = \beta \cdot \exp\left(\frac{2x}{\lambda}\right) \tag{3.12}$$

The quantity M is independent of the particle hit position and can be used to measure the gain factor α, whereas R is independent of the deposited energy in the module and may be used to determine the attenuation length λ and the asymmetry factor β.

Inverting these relations, one obtains:

$$E = \frac{1}{\alpha} M \tag{3.13}$$

$$x = \frac{\lambda}{2} \ln\left(\frac{R}{\beta}\right) \tag{3.14}$$

Measurement of the module gain

Large numbers of high energetic muons are crossing the detector along the beam direction between the two neutrino spills, so that the relative calibration can be performed in a short time and repeated frequently to monitor the calibration constants. Measuring energies in multiples of $m.i.p.$ energies requires the determination of α in units of ADC counts per $m.i.p.$ or, equivalently, the most probable value of M.

Muon data are selected using the $(V \times T_1 \times T_2)$ or $(V_8 \times T_1 \times T_2 \times \mathrm{FCAL}')$ triggers. Muon tracks are reconstructed in the drift and muon chambers and backward extrapolated to the FCAL. The energy deposition of muons follows mainly a Landau distribution with additional contributions (noise, hard muon

bremsstrahlung, photon electron smearing etc.). Since the mathematical average of a Landau distribution is not defined, and since the experimental average of a truncated distribution is strongly dependent on the tails of the distribution, the *most probable* energy is taken as the reference value instead. To obtain this parameter, the experimental distribution has been fitted to a function $\mathfrak{L}$ composed of:

- a Landau function $\phi(x)$, centered at $x = 0$ with width σ_l describing the energy deposition
- a Gaussian distribution $\Phi(x)$ with width σ_g which describes smearing due to noise processes such as fluctuation in the number of photoelectrons, electronics noise in the amplification chain
- a background distribution $B(x)$

The convolution $\mathfrak{L}$ is defined as:

$$\mathfrak{L}(y) \equiv B\left(\frac{y}{p}\right) + h\int_{-3}^{-3} \Phi(z)\psi\left(\frac{z+y-p}{\sigma_l}\right) dz \tag{3.15}$$

The definition of a Gaussian normal distribution is:

$$\Phi(y) \equiv \frac{1}{\sqrt{2\pi\sigma_g}} \exp\left(-\frac{y^2}{2\sigma_g^2}\right) \tag{3.16}$$

and the Landau distribution is:

$$\psi(y) \equiv \frac{1}{2\pi\imath}\int_{c-\imath\infty}^{c+\imath\infty} \exp\left(ys + s\,ln\,s\right) ds \tag{3.17}$$

The background function B describes empirically the low-energy part of the spectrum. Events having less than 75% of the most probable energy are very likely not to be ascribed to through-going muons. The inclusion of the background function improves the stability of the fitting procedure considerably, since the Landau distribution essentially gives no contribution in the low energy region. The function is defined by:

$$B\left(\frac{y}{p}\right) \equiv \begin{cases} b^2 \cdot \exp\left(-\frac{((y/p)-0.25)^2}{2\cdot(0.16)^2}\right) & \text{for } y < 0.25 \\ b^2 & \text{for } 0.25 \leq y < 0.75 \\ b^2 \cdot \exp\left(-\frac{((y/p)-1.39)^2}{2\cdot(0.16)^2}\right) & \text{for } 0.75 \leq y < 1.39 \\ 0 & \text{otherwise} \end{cases} \tag{3.18}$$

The function $\mathfrak{L}$ has five free parameters:

- p: the position of the most probable value, which is the parameter of interest for the extraction of the calibration constant α
- h: the normalization of the distribution (essentially, the number of events)
- σ_l: the width of the Landau distribution in ADC counts
- σ_g: the width of the Gaussian distribution in units of ADC counts
- b: the background parameter describing the normalization of the background distribution

The parameter p determines the calibration constant α for a module. If energy is measured in units of $m.i.p.$, $\alpha = p^{-1}[m.i.p./ADC]$.

Measurement of the module asymmetry and attenuation length

The calibration constants β and λ can be determined from data if the x-coordinate of the impact point of the muon in the module is known. This may be ascertained using backward extrapolation of the drift chamber track to the module under study. The extrapolation uncertainty from multiple scattering depends on the muon momentum and the amount of material traversed. The sum of all uncertainties is typically $\mathcal{O}(1$ cm), which has to be compared to a typical position measurement of the FCAL of $\simeq 10$ cm. Taking the average of many measurements at the same position x, a straight line fit to the relation:

$$\langle \ln R \rangle(x) = \langle \ln \frac{ADC_L}{ADC_R} \rangle(x) = \ln \beta + \frac{2x}{\lambda} \tag{3.19}$$

can be used to obtain the desired parameters β (offset) and λ (slope).

These calibration constants are measured [94, 98, 105, 106] for the whole NOMAD data taking period in intervals of weeks as well as for *MonteCarlo* data samples and are available in the NOMAD database.

3.3.2 Absolute calibration

Having obtained the calibration factors α, β and λ, all modules measure energy on the same scale, i.e. in units of the $m.i.p.$ scale. The hadronic energy equivalent of this unit still has to be determined. The hadronic energy deposited in the FCAL is calculated using:

$$E_{\text{had}} = \kappa \cdot \left(\sum_{i=1}^{4} \sum_{j=0}^{9} M_{ij}/\alpha_{ij} - \sum_{i=1}^{N_\mu} E_{if}^0 \right) \tag{3.20}$$

where the first is a double sum running over all modules in each stack. M_{ij} are the recorded energies in each module j of stack i in ADC counts and α_{ij} are

the calibration constants defined above. The second term runs over all muons emerging from the FCAL (mainly the muon from charged current interactions). E_f^0 is the mean energy a muon deposits traversing a FCAL stack, on average one $m.i.p.$. If the event is assumed to occur at the mid plane of the first stack hit, f, then the mean amount of energy deposition may be expressed as

$$E_f^0 = (4 - f + 0.5)\,[m.i.p.]. \tag{3.21}$$

κ is the conversion factor to convert the total energy measured in $m.i.p.$ to the absolute energy in GeV which has to be determined.

The calibration procedure applied (similar to the one in [93]) is using ν_μ^{CC} *MonteCarlo* events, which is essentially imitating a test beam where the real beam is substituted by the detector *MonteCarlo* simulation. Thus the absolute energy scale is established using *MonteCarlo*. Of course, this relies heavily on the correctness of the simulated beam and the simulated detector response. To demonstrate the level of agreement, in Chapter 4 the energy conversion factor is applied and a comparison between real data and *MonteCarlo* events is performed.

As a first step, the cuts to select events in a certain region of phase space are defined. These event selection criteria require knowledge of the vertex position in the FCAL. This is estimated calculating the center of gravity in the most upstream stack with total deposited energy above a threshold of 0.5 $m.i.p.$. This procedure will be discussed in more detail in Section 4.2.2. For now it is assumed that the vertex position is known with reasonably accuracy.

The cuts used are:

- **Charged current interaction**: Only events with exactly one negatively charged track having its first hit within the first 15 cm of the drift chambers geometrically matched with a track in the muon chambers which can be extrapolated backwards within the volume of the FCAL are selected.

- **Trigger threshold**: The FCAL will not register an event with an energy deposited in one of the four stacks below a threshold defined by a discriminator level in the data acquisition system (see Section 3.2.4). The trigger efficiency was measured in [77] (see also Figure 4.1) as a function of the maximum of the deposited energy in one stack in units of $m.i.p.$. The efficiency is essentially 100% for:

  $$\max\{E_{\text{Stack}}\} > 5\ m.i.p.,\ \ \text{Stack} = 1, \ldots, 4 \tag{3.22}$$

  In order that the calibration not be sensitive to the exact shape of the trigger threshold only events above this threshold are considered.

- **Transverse leakage**: The transverse dimensions of a hadronic shower are relatively independent of the shower energy [107] and scale roughly with the nuclear interaction length λ_I. On average 95% of the hadronic energy is

laterally contained within a radius of 1 λ_I. To minimize lateral leakage the vertex was required to be at least one λ_I (16.8 cm for iron) away from the boundaries of the FCAL. Energy is also unaccounted for if it is absorbed in the uninstrumented region in the center of the FCAL. The fiducial cuts used are:

$$|X_{\text{vertex}}| < 70 \text{ cm}, \;\; 20 \text{ cm} < |Y_{\text{vertex}}| < 70 \text{ cm} \tag{3.23}$$

- **Longitudinal leakage**: In a calorimeter short as the FCAL longitudinal energy leakage is a major concern. To select events with minimal amount of longitudinal leakage the 4th stack was used as a veto. The fraction of energy deposited in the most downstream stack was required to be less than 10% of the total deposited energy (this implies the vertex is not in stack 4). In order to take account of the energy deposit of the charged current muon one $m.i.p.$ was subtracted from the total $m.i.p.$ energy for each stack the muon traversed plus 0.5 $m.i.p.$ for the first stack hit (assuming the vertex is in the middle of the stack). Defining M_i to be the number of $m.i.p.$'s deposited in stack i and f to be the first stack hit, the appropriate cut is:

$$\frac{M_4 - 1.0}{\left(\sum_{i=f}^{4}(M_i - 1.0)\right) + 0.5} < 0.1 \tag{3.24}$$

For the selected events, Figure 3.11 shows a profile histogram of the total deposited energy in $m.i.p.$'s as a function of the energy in GeV. (M_N is the nucleon rest mass):

$$E_{\text{had}}^{\text{sim}} = E_{\nu}^{\text{sim}} - E_{\text{lep}}^{\text{sim}} + M_N \tag{3.25}$$

From a straight line fit the factor to convert energy measured in units of $m.i.p.$'s to units of GeV can be determined as:

$$1 \text{ GeV} = (2.367 \pm 0.003) \; m.i.p. \tag{3.26}$$

Sources of uncertainty

The considered sources of uncertainties are:

- **Beam profile**: The calibration method using *MonteCarlo* relies on the ability to sample the same regions of phase space in both the data and *MonteCarlo* events. Different neutrino beam profiles would result in different average neutrino energies within a fiducial volume thus sampling different cross-sections resulting in different kinematics. The effect of different beam profiles in the calibration has been studied using reweighting of *MonteCarlo* events inside the used fiducial volume (see Section 4.1) and found to be less than 1%.

- **Simulation of hadronic processes**: The final contribution in the calibration constant arises from inaccuracies in the simulation of hadronic processes in the *MonteCarlo*. A comparison of different hadronic packages has been performed in relation to the ATLAS experiment [108] including the version FLUKA92 used by GENOM. They conclude that in the few GeV range (hadronic energies of less than 5 GeV) the description exhibits a number of problems. In the high energy range FLUKA92 agrees with data to an accuracy of approximately 8%.

Results of calibration

Taking into account the systematic effects discussed above with a conservative estimate of 10% the energy calibration constant for neutrino interactions in the FCAL was found to be:

$$\kappa = \frac{1 \text{ GeV}}{(2.367 \pm 0.003(\text{stat}) \pm 0.24(\text{sys}))\ m.i.p.} \tag{3.27}$$

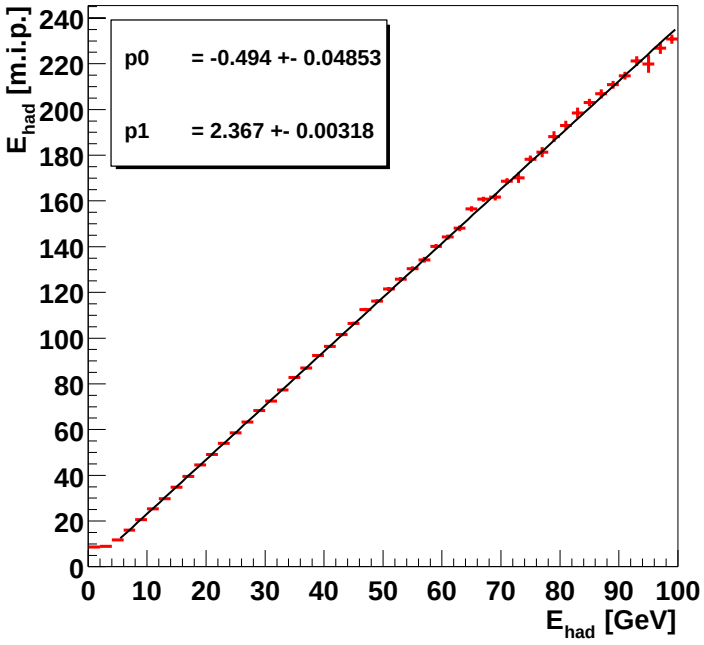

Figure 3.11: *Energy deposited in m.i.p.'s as a function of the energy in GeV for MonteCarlo events.*

Chapter 4

Analysis of neutrino interactions

An analysis using interactions in the FCAL requires selection criteria for the different types of FCAL events. In this chapter the algorithms of these selection criteria are discussed, pointing out possible differences between real data and *MonteCarlo* events. After classifying the available data samples, the obtained numbers of events as well as a subset of charged current event kinematics variables are compared to *MonteCarlo* predictions. Further, the FCAL timing information, combined with the timing information obtained from the drift chamber tracks, is introduced, an important ingredient for analyses such as the search for neutral heavy leptons.

4.1 Adjustment *MonteCarlo* to data

Before comparing events generated within the simulation framework to real data events, effects known to be not implemented in the simulation or not described sufficiently well have to be included or corrected. Here the following items are considered and described below:

- Noise (Data and *MonteCarlo*) and saturation (*MonteCarlo*)
- Beam simulation (reweighting in *MonteCarlo*)
- Trigger simulation (in *MonteCarlo*)

Noise and Saturation

The response of the FCAL to hadronic showers has been modeled in the GENOM detector simulation introduced in Chapter 2.4. The *ADCs* have a linear and infinite dynamic range in the *MonteCarlo* (see also the linear behavior in Figure 3.11) but are non-linear and can saturate in the data. The absence of the non-linearity simplifies the determination of the energy conversion factor but is essential for the comparison to data.

Since this non-linearity is highly dependent on the relative calibration discussed above (the scintillator response or the photomultiplier gain may change over time but the *ADC* length remains constant) it is implemented at the level of the analysis.

Given the energy deposition and the position of a hit in a module one can, using Equations 3.11 and 3.12 as well as the valid calibration constants, calculate the *ADC* values for that module.

ADC values less than 20 *ADC* counts, representing noise, are not used for data and *MonteCarlo*.

The non-linearity is implemented for each module j with *ADC* values ($i =$ Left, Right) by using:

$$ADC_i' = L_j + \frac{(ADC_i - L_j)}{\sqrt{1 + \left(\frac{ADC_i - L_j}{L_j}\right)^{1.02}}} \tag{4.1}$$

for *ADC* values greater than $L_j = 20 \cdot \alpha_j$, where α_j is the module calibration factor, the average *ADC* counts for a minimum ionizing particle.

Further, the saturation is implemented as a cutoff for these values ADC_i' at $(4095 - 200)$, which is the maximum possible *ADC* count for the used *ADC* types minus an approximate average pedestal value.

Now the deposited energy and the hit position are recalculated using the saturated ADC_i' and the inverse Equations 3.13 and 3.14.

Beam reweighting

It is known from within the framework of the NOMAD $\nu_\mu \leftrightarrow \nu_e$ oscillation search, which heavily relies on the beam description, that the shape of the ν_μ flux is not estimated very well by the version of the beam simulation interfaced by default to the event generation package used to generate the *MonteCarlo* samples for this analysis.

The samples were generated using the beam simulation NUBEAM400 and the model for proton-beryllium interactions in FLUKA92. It is known [109] that this version of FLUKA is incorrectly simulating the distributions of transverse momenta of particles in $p-Be$ interactions causing observed disagreements in neutrino energy spectra, confirmed by results from the SPY collaboration [110]. More actual versions including better descriptions are NUBEAM606 and FLUKA98.

In order that the effects of different beam simulation packages can be studied, weighting tables to and from the different beam prescriptions have been produced [111]. The generated *MonteCarlo* events with a given neutrino energy E_ν and radial distance R of the interaction point from the center of the beam in the NOMAD frame of reference are reweighted by the relative difference of the flux predictions a and b:

$$\text{weight}(E_\nu, R) \equiv \frac{\Phi^{\text{b}}(E_\nu, R)}{\Phi^{\text{a}}(E_\nu, R)} \tag{4.2}$$

Here a is labelling the versions used to generate the samples and b the more actual versions quoted above.

Trigger Simulation in *MonteCarlo*

Trigger signals such as $(\overline{V}_8 \times \text{FCAL})$ and $(\overline{V}_8 \times \text{FCAL}' \times T_1 \times T_2)$ are not build inside the detector simulation but are important in a comparison between data and *MonteCarlo*, especially in the low energy region.

Both signals FCAL and FCAL′ are only present if at least one of the four stacks registers an energy deposition above a certain threshold (see Chapter 3.2.4).

To implement these two signals the measured efficiencies [77], shown in Figures 4.1 and 4.1, were used in a *MonteCarlo* technique using the trigger efficiencies as probabilities to fire the signals for a given $\max\{E_{\text{Stack}}[m.i.p.]\}$.

For the trigger $(\overline{V}_8 \times \text{FCAL}' \times T_1 \times T_2)$ this is combined with the information if the two trigger planes T_1 and T_2 were hit.

The veto signals used to form the final trigger signals are not available at the level of the analysis and therefore not used. Since events were generated inside the detector, vetoing is not an important effect. However, there could be events back-splashing and self-vetoing, but this is assumed to be a minor correction [105].

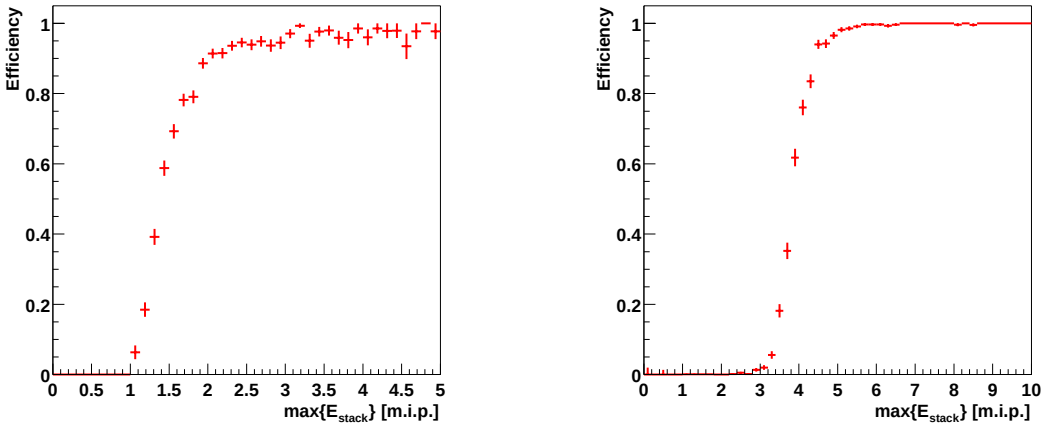

Figure 4.1: *Trigger efficiency FCAL′ (left) and FCAL (right) as a function of the maximum energy deposited in one stack in units of m.i.p..*

4.2 Event selection and classification

Interactions in the front calorimeter may be selected and classified using the following criteria:

- **Trigger conditions**
- **Primary vertex in FCAL fiducial volume**
- **Interaction type classification**
  - *Neutrino charged current*
  - *Neutrino neutral current*
  - *Cosmic rays*

In the following sections these criteria are further specified and defined.

4.2.1 FCAL triggers

Two triggers to select neutrino interactions in the front calorimeter are available (see Sections 2.3 and 3.2.4):

- $(\overline{V}_8 \times \mathrm{FCAL}) \equiv FCAL$
- $(\overline{V}_8 \times \mathrm{FCAL}' \times T_1 \times T_2) \equiv FCAL'$

The NOMAD trigger system stores the status of the several triggers at the time an event is selected and also 200 ns later. Both the *undelayed* and *delayed* trigger information is used. For *MonteCarlo* the triggers are simulated as described in Section 4.1.

4.2.2 Determination of the event vertex

The FCAL is divided into four stacks along the longitudinal direction z. The interaction is assumed to occur in the center of the most upstream stack with an energy deposit of at least 0.5 $m.i.p.$, labelled f:

$$z_{\mathrm{FCAL}} = \text{center of Stack } f \tag{4.3}$$

Because of their small cross-section neutrinos interact uniformly along their way traversing the detector. The variance of a uniform distribution on an interval of width W is:

$$\sigma = \frac{W}{\sqrt{12}}, \tag{4.4}$$

so the error in the determination of the longitudinal position of the vertex in a stack is:

$$W_{\text{stack}} = 33.5 \text{ cm} \;\Rightarrow\; \sigma_z = 9.7 \text{ cm} \tag{4.5}$$

The transverse position of the vertex may be ascertained in two ways:

- **Muon extrapolation**:
  Applicable only to processes with a muon produced at the primary vertex such as ν_μ^{CC}, $\overline{\nu}_\mu^{CC}$ or quasielastic processes. This method involves the backward extrapolation of the drift chamber muon track to the z position in the FCAL.

- **Center of Gravity in the stack containing the primary vertex**:
  Equation 3.14 showed the possibility to estimate the x position of the energy deposition within a single module. There is no information about where, on the y axis, the energy was deposited, so the y position of a module center is chosen. For a given hadronic shower the event vertex transverse positions can be estimated by calculating the center of gravity or energy E_i weighted mean of module i positions x_i and y_i within the stack the interaction is assumed to have occurred:

$$x_{\text{FCAL}} = \frac{\sum_i E_i \cdot x_i}{\sum_i E_i} \text{ and } y_{\text{FCAL}} = \frac{\sum_i E_i \cdot y_i}{\sum_i E_i} \tag{4.6}$$

Assuming that the transverse dimension of the hadronic shower development in the stack containing the vertex is smaller than the vertical size of a module and since no information is given where in the module the interaction occurred, the resulting resolution can be estimated as:

$$W_{\text{module}} = 18.5 \text{ cm} \;\Rightarrow\; \sigma_y = 5.3 \text{ cm} \tag{4.7}$$

A study on ν_μ^{CC} *MonteCarlo* events confirmed the estimated resolutions in z- and y-direction and the resolution in the x-direction is measured as $\sigma_x \simeq 2.5$ cm. Further details may be found in References [93, 94, 96].

Since for the analysis performed in this thesis both neutral and charged current interactions have to be considered (for the first the muon extrapolation method of course does not work) and the FCAL vertex resolutions resulting from the center of gravity method are sufficient, this method is used.

4.2.3 Neutrino charged current identification

The identification of neutrino charged current interactions in the front calorimeter is mainly the identification of the charged lepton produced in the FCAL and traversing at least a part of the other subdetectors. Since the neutrino beam

consists of several neutrino types with different relative fluxes (see Section 2.2), the charged lepton may be of type muon or electron. Since the probability of the latter to escape the FCAL volume and to be identified in the drift chambers and/or the combination of TRD/PRS is quite small and because of their small relative fluxes compared to the muon neutrino types only positive and negative muons originating from the FCAL have to be identified.

Primary muon identification

The primary means of muon identification is the penetrating power of a candidate particle. Muons from events occurring in stack 4 can be identified by the muon chambers if they penetrate more than 8 interactions lengths (λ_{int}) of absorber material in order to reach muon station 1, or 13 λ_{int} for muon station 2. For muons from interactions in stack 1 one has to add the 5 λ_{int} of the FCAL material. For perpendicular incidence, the momentum thresholds for muons in the drift chambers to reach the muon chambers (with 50% probability) are measured to be 2.3 GeV/c for station 1, and 3.7 GeV/c for station 2 [75]. Again, for interactions in the FCAL, the energy loss in the additional material has to be added: 0.25 GeV for penetrating the coil and 0.35 GeV for each stack traversed [105]. The criteria for a drift chamber track originating in the FCAL to be identified as a muon are:

- **Matching to muon chamber track(s)**: The drift chamber track can be extrapolated forward to at least one of the muon chamber stations within a transverse distance of 40 cm to a track in station 1 or 50 cm in station 2. Particles outside the geometrical acceptance of the muon chambers, or ranging out in the detector material can fail this criterion. A minimum track momentum cut (at its first hit in the drift chambers) of 2.5 GeV/c is applied to reduce background from π/K decays and hadron "punchthrough" from particles created either in the FCAL or in coil interactions.

- **Matching to the FCAL**:

  - The track has its first hit within[1]:

$$\left.\begin{array}{r} 0 \text{ cm} \\ 29 \text{ cm} \end{array}\right\} \leq z_{\text{first hit}} < \left\{\begin{array}{ll} 15 \text{ cm} & \text{for data 96 and } MC \\ 45 \text{ cm} & \text{for data 97 and 98} \end{array}\right. \tag{4.8}$$

  - and can be extrapolated backwards to the stack containing the vertex within the FCAL sensitive volume[2]:

$$|x| < 87.5 \text{ cm}, \;\; |y| < 95.0 \text{ cm} \;\; \text{and} \;\; -242.6 \text{ cm} < z < -90.3 \text{ cm} \tag{4.9}$$

[1] At the beginning of the 1997 data taking period the first 3 chambers of drift chamber module 1 have been removed to install an additional subdetector STAR [112, 113].

[2] In the detector simulation the FCAL has a constant z-offset of +6.9 cm. One always has to add this when referencing FCAL *MonteCarlo* z-positions.

The first item is referenced as *loose muon id* and the second as *FCAL association* from now on.

If there is more than one candidate track, the one with the highest momentum is tagged as the primary muon.

For the matching to the FCAL a combination of a linear (no magnetic field in coil and FCAL) and a helix (magnetic field in drift chambers) extrapolation is used, not taking into account the energy loss in the material traversed. The extrapolated energy and momentum at the primary vertex (PV) are corrected by:

$$E_\mu^{\mathrm{PV}} = \sqrt{|\vec{p}_{\mathrm{extrap}}|^2 + m_\mu^2} + dE_{\mathrm{coil}} + dE_{\mathrm{stacks}} \tag{4.10}$$

$$\vec{p}_\mu^{\mathrm{PV}} = \frac{\vec{p}_{\mathrm{extrap}}}{|\vec{p}_{\mathrm{extrap}}|} \cdot \sqrt{E_\mu^{\mathrm{PV}^2} - m_\mu^2} \tag{4.11}$$

with:

$$dE_{\mathrm{coil}} = 0.25\ \mathrm{GeV} \tag{4.12}$$

$$dE_{\mathrm{stacks}} = 0.35\ \mathrm{GeV} \cdot (4 - f + 0.5) \tag{4.13}$$

$(4 - f + 0.5)$ is the number of stacks traversed plus a half for the stack number f (see Section 4.2.2). The position of the primary lepton is taken to be the center of the primary vertex stack with transverse position of the extrapolation. A comparison to an extrapolation including multiple scattering and energy loss showed that the resulting accuracy is good.

4.2.4 Cosmic ray interactions

Cosmic ray muons traversing the FCAL can mimic neutral current neutrino interactions as explained below. Therefore it is important to identify cosmic events if their contribution to the neutral current event sample is not negligible and quantities such as the ratio of neutrino neutral and charged current interactions (see Section 4.3.5) have to be calculated.

"Primary" (particles accelerated at astrophysical sources) and "secondary" (particles produced in interactions of primaries with interstellar gas) cosmic rays interacting in the atmosphere produce mainly [1] protons, neutrons and pions.

Muons from charged pion decays are the most numerous charged particles at sea level. Their energy and angular distribution reflect a convolution of production spectrum, energy loss in the atmosphere, and decay. The mean energy at the ground is $\simeq 4$ GeV. The integral intensity of vertical muons above 1 GeV/c at sea level is $\simeq 70\ \mathrm{m^{-2}s^{-1}sr^{-1}}$ or $1\ \mathrm{cm^{-2}min^{-1}}$ for a horizontal detector.

The overall angular distribution of muons at the ground is $\propto \cos^2\theta$ which is characteristic for muons with $E_\mu \simeq 3$ GeV. At lower energy the angular distribution becomes increasingly steeper, while at higher energy it flattens.

Thus the signature of a cosmic muon mimicking a FCAL event is a particle traversing the volume from the top to the bottom with similar energy deposits ($m.i.p.$'s) in a group of vertically arranged modules and no track in the drift chambers (the probability of an overlap between a cosmic particle firing the FCAL and a ($\overline{V} \times T_1 \times T_2$) trigger is very small compared to the FCAL cosmic trigger rate).

The main strategy to identify FCAL cosmic events is extracting the vertical incident angle of energy deposits in the detector.

A way to measure the angle of a particle traversing the FCAL is using the energy weighted mean of energy deposits in one stack:

$$< y_j >= \frac{\sum_i E_{ij} \cdot y_{ij}}{\sum_i E_{ij}} \tag{4.14}$$

and its second momentum, representing the width of the energy deposition:

$$dy_j \equiv \sigma_{<y_i>} = \sqrt{\frac{\sum_i E_{ij} \cdot y_{ij}^2}{\sum_i E_{ij}} - \left(\frac{\sum_i E_{ij} \cdot y_{ij}}{\sum_i E_{ij}}\right)^2} \tag{4.15}$$

- **Very small angles**:
  If the angle is very steep and only one FCAL stack f is traversed one can use the width to identify cosmic events:

  $$dy_f > 18.5 \text{ cm} \tag{4.16}$$

  The value chosen represents the width of one module. For neutrino interactions the width of the shower in the stack containing the vertex is relatively small compared to a cosmic particle traversing the stack (see Figure 4.2).

- **Small angles**:
  If the angle is larger and several stacks are traversed the difference between the energy gravity centers in the first and last stack hit (labelled f and l respectively) is used:

  $$|\delta y_{fl}| \equiv | < y_f > - < y_l > | > 37.0 \text{ cm} \tag{4.17}$$

  Here the chosen cut value is the width of two modules. Figure 4.3 shows the distributions for neutrino interactions and cosmic events (taken without neutrino beam in a so-called Machine Development phase).

If the incident angle is greater the cosmic ray particle would hit the veto and the event is rejected by the included trigger condition of a veto anti-coincidence.

The steps respective spikes in the distributions in Figure 4.2 and Figure 4.3 represent the vertical dimensions of the FCAL modules.

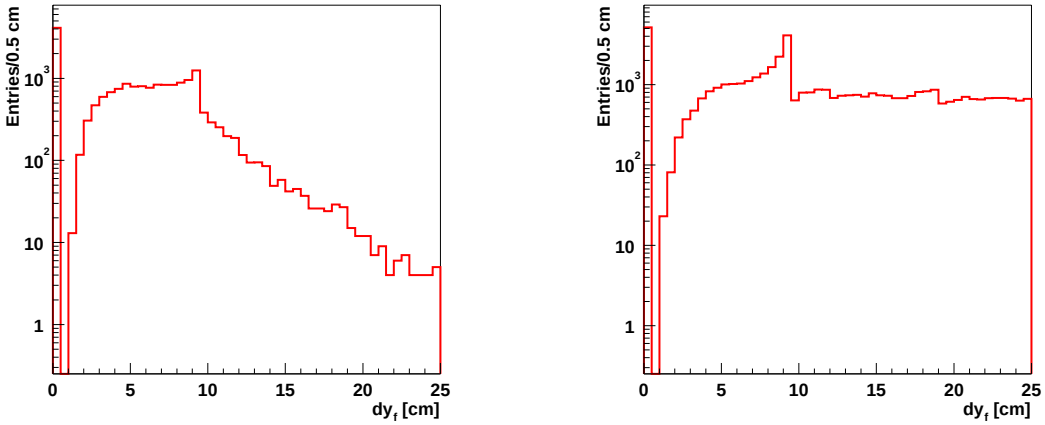

Figure 4.2: *Distributions for dy_f in ν_μ^{CC} (left) and cosmic (right) data interactions.*

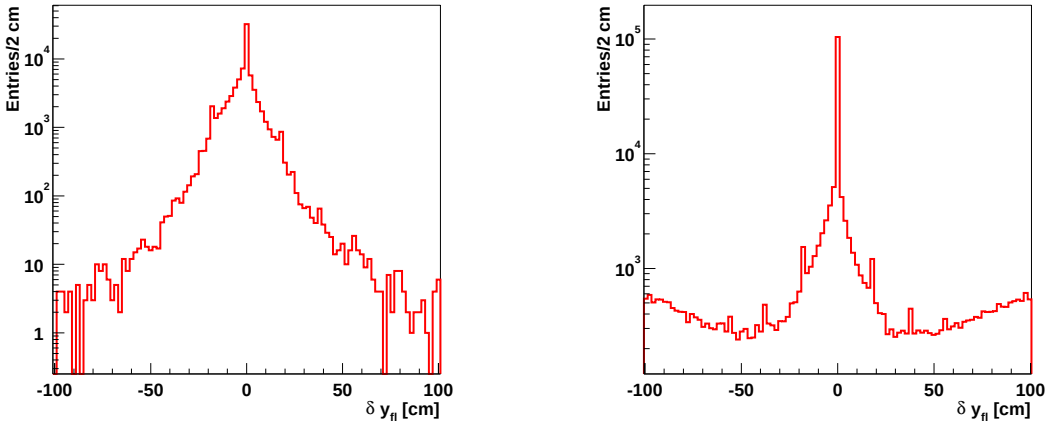

Figure 4.3: *Distributions for δy_{fl} in ν_μ^{CC} (left) and cosmic (right) data interactions.*

Efficiency

Pure cosmic ray interactions can be analyzed with data recorded without neutrino beam. The efficiency of the cuts to identify cosmic ray interactions, defined as the number of cosmics identified as cosmics, was measured to be:

$$(75.9 \pm 0.4)\% \tag{4.18}$$

In return,

$$(24.1 \pm 0.3)\% \tag{4.19}$$

cosmics are identified as neutrino neutral current interactions.

The uncertainties are the statistical errors of the used event sample.

Purity

The purity of identified cosmic ray interactions, defined as the ratio of real cosmics identified as cosmics, can be estimated using a sample of pure neutrino neutral current interactions, e.g. *MonteCarlo* ν_μ^{NC} events. From these (see Table 4.9 in Section 4.3.3)

$$(2 \pm 2)\% \tag{4.20}$$

are identified as cosmics. Assuming this is the main contamination the purity can be estimated to be:

$$(98 \pm 2)\% \tag{4.21}$$

Here also the statistical errors of the used event sample are quoted.

Both, the efficiency and the purity, show that the cuts to identify cosmic ray interactions are quite loose but sufficient.

4.2.5 Neutral current interaction identification

If a FCAL event is not identified as a muon neutrino charged current or cosmic ray interaction it is classified as a neutral current event.

Since no information of the outgoing primary lepton (neutrino) is available one can not distinguish neutral currents of the different neutrino species. Also a primary lepton identification for electrons and positrons is not performed because their probability to escape the FCAL is too small.

The main contamination of this event sample are muon neutrino charged current events where the primary muon is outside the geometrical acceptance of the muon chambers or ranging out in the detector material. Smaller contributions come from unidentified cosmics and electron neutrino neutral and charged current interactions (the relative flux of the latter to the muon neutrino type is $\mathcal{O}(1\%)$, see Section 2.2).

4.2.6 Selection criteria

The selection and classification criteria for interactions in the front calorimeter used in the following sections refer to the ones defined as:

- **Trigger condition**:
  one of the two FCAL triggers is required to have fired:

$$FCAL \equiv (\overline{V}_8 \times \text{FCAL}) \tag{4.22}$$
$$FCAL' \equiv (\overline{V}_8 \times \text{FCAL}' \times T_1 \times T_2) \tag{4.23}$$

- **FCAL fiducial volume**:
  the reconstructed primary vertex (using the center of gravity method) must be in the volume[3]:

$$|x| < 90.0 \text{ cm}, \;\; |y| < 90.0 \text{ cm} \;\; \text{and} \;\; -240.15 \text{ cm} < z < -116.15 \text{ cm} \tag{4.24}$$

- **Interaction type classification**:
  the event must be classified as one of the types:

$$\text{muon neutrino charged current} \quad \nu_\mu^{CC} \tag{4.25}$$
$$\text{muon anti neutrino charged current} \quad \overline{\nu}_\mu^{CC} \tag{4.26}$$
$$\text{neutrino neutral current} \quad \nu^{NC} \tag{4.27}$$
$$\text{cosmic ray} \quad \text{cosmic} \tag{4.28}$$

MonteCarlo events are preselected having been generated in the FCAL fiducial volume and reweighted as described in Section 4.1. FCAL *ADC* saturation effects have been included using the results from Section 4.1. Further, events with problems during data taking (online errors), reconstruction (offline errors) or at generation level (MC truncated) are excluded from analyses but may be listed for completeness (labelled as PRE).

4.3 Event statistics

This thesis is based on data collected during the NOMAD data taking periods in 1996, 1997 and 1998 [114]. Although the FCAL was already instrumented and taking data in 1995, data from this period was not used as not available in the same framework of reconstruction and analysis format.

[3] see also footnote on Page 60

4.3.1 Protons on target

In Table 4.1 the exposures of protons on target delivered by the SPS are listed for the different data taking periods as $\sum BCT_{\rm SPS}$. During 1998 the SPS switched the beam operation mode for about two times three weeks to the production of anti neutrinos ($\overline{\nu}$). Also shown are equivalent numbers of *p.o.t.*'s for the data collected by the NOMAD experiment, $\sum BCT_{\rm NOMAD}$, and for the reconstructed FCAL events, $\sum BCT_{\rm FCAL}$ (in SPS neutrino spills tagged as good). $\sum BCT_{\rm NOMAD}$ *w.r.t.* $\sum BCT_{\rm SPS}$ can be used to estimate the lifetime of the NOMAD experiment whereas $\sum BCT_{\rm FCAL}$ *w.r.t.* $\sum BCT_{\rm NOMAD}$ represents the losses during reconstruction. These numbers will be used when calculating the total numbers of neutrino interactions in the FCAL (see Section 4.3.6).

Sample	96	97	98	
Type	ν	ν	ν	$\overline{\nu}$
	[10^{19} *p.o.t.*] ± 0.01	[10^{19} *p.o.t.*] ± 0.01	[10^{19} *p.o.t.*] ± 0.01	[10^{19} *p.o.t.*] ± 0.01
$\sum BCT_{\rm SPS}$	1.46	1.66	1.34	0.47
$\sum BCT_{\rm NOMAD}$	1.40	1.57	1.21	0.43
$\sum BCT_{\rm FCAL}$	1.36	1.55	1.20	0.43

Table 4.1: *Protons on target for the different data taking periods.*

4.3.2 Initial data and *MonteCarlo* statistics

The available initial statistics of reconstructed FCAL events for the data taking periods are summarized in Table 4.2. The events are further listed by different combination of the FCAL trigger types. Table 4.3 lists the available statistics of generated *MonteCarlo* muon neutrino neutral and charged current events.

Sample	96	97	98	
Type	ν	ν	ν	$\overline{\nu}$
$(FCAL) \vee (FCAL')$	10.464.618	10.820.938	7.791.265	1.215.046
$(FCAL)$	9.144.352	9.515.266	6.866.924	979.945
$(\overline{FCAL}) \wedge (FCAL')$	1.320.266	1.305.672	924.341	235.101

Table 4.2: *Initial statistics of FCAL data for the data taking periods as the number of reconstructed events for different $FCAL$ and $FCAL'$ trigger combinations.*

ν_μ^{CC}	ν_μ^{NC}
563.642	239.886

Table 4.3: *Initial statistics of generated ν_μ^{CC} and ν_μ^{NC} MonteCarlo events used in this analysis.*

4.3.3 Event classification

Using the selection and classification criteria of Section 4.2.6 the selected available data and *MonteCarlo* event types are summarized in Tables 4.4, 4.5, 4.6, 4.7, 4.8 and 4.9, together with the relative selection efficiencies of each cut (*w.r.t.* its predecessor).

Sample	96ν					
RAW	10.464.618			100.00%		
PRE	10.464.598			100.00%		
	$(FCAL) \vee (FCAL')$		$(FCAL)$		$(FCAL') \wedge (\overline{FCAL})$	
Trigger	–	–	9.144.333	87.38%	1.320.265	12.62%
FCAL fid.	9.682.872	92.53%	8.541.848	93.41%	1.141.024	86.42%
ν_μ^{CC}	4.324.899	44.67%	3.573.685	41.84%	751.214	65.84%
$\overline{\nu}_\mu^{CC}$	87.854	0.91%	70.633	0.83%	17.221	1.51%
ν^{NC}	3.977.124	41.07%	3.610.991	42.27%	366.133	32.09%
cosmic	1.292.995	13.35%	1.286.539	15.06%	6.456	0.57%

Table 4.4: *Selection and classification of FCAL events 1996.*

Sample	97ν					
RAW	10.820.938			100.00%		
PRE	10.546.036			97.46%		
	$(FCAL) \vee (FCAL')$		$(FCAL)$		$(FCAL') \wedge (\overline{FCAL})$	
Trigger	–	–	9.288.883	88.08%	1.257.153	11.92%
FCAL fid.	9.742.543	92.38%	8.671.758	93.66%	1.070.785	85.18%
ν_μ^{CC}	4.819.879	49.47%	4.037.874	46.56%	782.005	73.03%
$\overline{\nu}_\mu^{CC}$	107.549	1.10%	84.418	0.97%	23.131	2.16%
ν^{NC}	3.722.261	38.21%	3.456.990	39.86%	265.271	24.77%
cosmic	1.092.854	11.22%	1.092.476	12.60%	378	0.04%

Table 4.5: *Selection and classification of FCAL events 1997.*

A few comments on the *MonteCarlo* Tables 4.8 and 4.9:

Sample	98ν					
RAW	7.791.265			100.00%		
PRE	7.591.026			97.43%		
	$(FCAL) \vee (FCAL')$		$(FCAL)$		$(FCAL') \wedge (\overline{FCAL})$	
Trigger	–	–	6.690.490	88.14%	900.536	11.86%
FCAL fid.	7.152.686	94.23%	6.361.108	95.08%	791.578	97.90%
ν_μ^{CC}	3.677.983	51.42%	3.085.855	48.51%	592.128	74.80%
$\overline{\nu}_\mu^{CC}$	92.691	1.30%	71.900	1.13%	20.791	2.63%
ν^{NC}	2.744.975	38.38%	2.566.634	40.35%	178.341	22.53%
cosmic	637.037	8.91%	636.719	10.01%	318	0.04%

Table 4.6: *Selection and classification of FCAL events 1998 (ν).*

Sample	$98\overline{\nu}$					
RAW	1.215.046			100.00%		
PRE	1.195.764			98.41%		
	$(FCAL) \vee (FCAL')$		$(FCAL)$		$(FCAL') \wedge (\overline{FCAL})$	
Trigger	–	–	963.086	80.54%	232.678	19.46%
FCAL fid.	1.066.230	89.17%	907.860	94.27%	158.370	68.06%
ν_μ^{CC}	134.107	12.58%	118.334	13.03%	15.773	9.96%
$\overline{\nu}_\mu^{CC}$	378.154	35.47%	276.458	30.45%	101.696	64.21%
ν^{NC}	388.128	36.40%	347.289	38.25%	40.839	25.79%
cosmic	165.841	15.55%	165.779	18.26%	62	0.04%

Table 4.7: *Selection and classification of FCAL events 1998 ($\overline{\nu}$).*

Sample	*MonteCarlo* ν_μ^{CC}					
RAW	563.642			100.00%		
PRE	473.303			83.97%		
	$(FCAL) \vee (FCAL')$		$(FCAL)$		$(FCAL') \wedge (\overline{FCAL})$	
Trigger	448.775	94.82%	404.090	85.38%	44.685	9.44%
FCAL fid.	448.158	99.86%	403.566	99.87%	44.592	99.79%
ν_μ^{CC}	333.354	74.38%	294.239	72.91%	39.115	87.72%
$\overline{\nu}_\mu^{CC}$	6.922	1.54%	6.681	1.66%	241	0.54%
ν^{NC}	105.717	23.59%	100.529	24.91%	5.188	11.63%
cosmic	2.165	0.48%	2.117	0.54%	48	0.11%

Table 4.8: *Selection and classification of MonteCarlo ν_μ^{CC} events.*

Sample	*MonteCarlo* ν_μ^{NC}					
RAW	239.886				100.00%	
PRE	201.513				84.00%	
	$(FCAL) \vee (FCAL')$		$(FCAL)$		$(FCAL') \wedge (\overline{FCAL})$	
Trigger	167.048	82.90%	162.218	80.50%	4.830	2.40%
FCAL fid.	166.809	99.86%	162.005	99.87%	4.804	99.46%
ν_μ^{CC}	153	0.09%	141	0.09%	12	0.25%
$\overline{\nu}_\mu^{CC}$	139	0.08%	135	0.08%	4	0.08%
ν^{NC}	163.438	97.98%	158.671	97.94%	4.767	99.23%
cosmic	3.079	1.85%	3.058	1.89%	21	0.44%

Table 4.9: *Selection and classification of MonteCarlo* ν_μ^{NC} *events.*

- Events are preselected to have been generated in the used fiducial volume, the listed cut on the fiducial refers to the reconstructed primary vertex.
- Comparing the breakdown of the trigger selection for CC and NC shows the effect of the $FCAL'$ trigger with its lower energy threshold. The primary muon in CC events fulfills the included condition that the trigger planes fired, whereas in NC events there is no primary muon.

From these numbers several quantities can be derived, such as:

- Selection efficiency of ν_μ^{CC} and ν^{NC} events
- Ratio of neutral and charged current interactions $R_{\mathrm{NC/CC}}$
- Calculated number of charged current interactions,

which are described in the following sections.

4.3.4 Selection efficiency of ν_μ^{CC} and ν^{NC} events

Using Tables 4.8 and 4.9, the averaged selection efficiencies for charged and neutral current events originating in the FCAL can be estimated. Table 4.10 lists these overall (including the cuts on trigger and fiducial) efficiencies $\varepsilon_{\mathrm{CC}}$ and $\varepsilon_{\mathrm{NC}}$ for events with $(FCAL) \vee (FCAL')$ triggers. Also quoted is the efficiency $\varepsilon_{\mathrm{CC}}^{\mu}$ for the muon selection in charged current events. The uncertainties are only statistical.

4.3.5 Ratio $R_{\mathrm{NC/CC}}$

Neutrino charged current interactions where the primary muon is not identified (e.g. range out in the detector material or outside the geometrical acceptance)

$\varepsilon^{\mu}_{\mathrm{CC}}[\%]$	$\varepsilon_{\mathrm{CC}}[\%]$	$\varepsilon_{\mathrm{NC}}[\%]$
74.4 ± 0.2	70.4 ± 0.2	81.1 ± 0.3

Table 4.10: *Charged and neutral current interaction selection efficiencies.*

are identified as neutral current interactions. Since the fraction of ν_{μ}^{CC} with lost muon is relatively large (about $(1-\varepsilon^{\mu}_{\mathrm{CC}}) \simeq 25\%$) they represent a non-negligible contamination of the ν^{NC} event sample.

As a first order approximation, the ratio of neutral and charged current interactions $R_{\mathrm{NC/CC}}$ can be calculated by correcting the measured numbers of events N_{NC} and N_{CC} for selection efficiencies (Table 4.10) and the number of ν_{μ}^{CC} with lost primary muon, $N^{\mathrm{lost}}_{\mathrm{CC}}$:

$$R_{\mathrm{NC/CC}} = \frac{N^{\mathrm{corr}}_{\mathrm{NC}}}{N^{\mathrm{corr}}_{\mathrm{CC}}} = \frac{\frac{N_{\mathrm{NC}}}{\varepsilon_{\mathrm{NC}}} - N^{\mathrm{lost}}_{\mathrm{CC}}}{\frac{N_{\mathrm{CC}}}{\varepsilon_{\mathrm{CC}}}} = \frac{\frac{N_{\mathrm{NC}}}{\varepsilon_{\mathrm{NC}}} - \frac{N_{\mathrm{CC}}}{\varepsilon_{\mathrm{CC}}}(1-\varepsilon^{\mu}_{\mathrm{CC}})}{\frac{N_{\mathrm{CC}}}{\varepsilon_{\mathrm{CC}}}} \tag{4.29}$$

The resulting ratio $R_{\mathrm{NC/CC}}$ does not include corrections for the different components of the beam and their energy spectra. Also not included are corrections like e.g. quark sea effects, c-quark threshold effects, target non-isoscalarity. $R_{\mathrm{NC/CC}}$ represents the measured ratio corrected only for the efficiencies. Like this, it can not be used for e.g. a measurement of the Weinberg angle and compared to the quark-level value [115] for $R_{\mathrm{NC/CC}}$ of (0.3072 ± 0.0033). According to Reference [116] for the given experimental setup the calculated value is $R_{\mathrm{NC/CC}} \simeq (0.40 \pm 0.02)$.

Table 4.11 lists the corresponding numbers for the different data taking periods, where the quoted errors result from the selection efficiencies.

	$N^{\mathrm{corr}}_{\mathrm{CC}}$ $[10^6]$	$N^{\mathrm{lost}}_{\mathrm{CC}}$ $[10^6]$	$N^{\mathrm{corr}}_{\mathrm{NC}}$ $[10^6]$	$R_{\mathrm{NC/CC}}$
96_{ν}	6.143 ± 0.017	1.579 ± 0.013	3.325 ± 0.018	0.541 ± 0.003
97_{ν}	6.846 ± 0.019	1.760 ± 0.015	2.830 ± 0.018	0.413 ± 0.003
98_{ν}	5.224 ± 0.015	1.343 ± 0.011	2.042 ± 0.014	0.391 ± 0.003

Table 4.11: *Efficiency corrected numbers of neutral and charged current interactions and the ratio $R_{NC/CC}$.*

The values for the periods 1997 and 1998 agree well whereas the value obtained from the 1996 data is too high. As will be shown in Section 4.3.6 the number of charged current interactions agrees with the calculated estimates, so that the number of neutral current events is overestimated for the 1996 period. The results also reflect the fact that the 1996 and *MonteCarlo* ν_{μ}^{CC} and ν^{NC} data samples

have been processed with a different (older) version of the reconstruction program than the 1997 and 1998 samples (see also Section 6.1).

Taking the average of the values obtained from the 1997 and 1998 data samples and including a 5% systematic uncertainty yields:

$$R_{\mathrm{NC/CC}} = 0.402 \pm 0.002(\mathrm{stat.}) \pm 0.021(\mathrm{sys.}) \tag{4.30}$$

This agrees with the calculated value of Reference [116].

4.3.6 Calculated neutrino event rate

The number of neutrino charged current interactions in the FCAL can be estimated by a first-principles calculation of the neutrino event rate and combining the neutrino flux and cross-section with the detector material density using

$$N_{CC}^{\mathrm{calc}} = \int \phi \cdot \sigma_{CC}(E_\nu) \cdot \rho L N_{\mathrm{A}}\, dE\, dA\,, \tag{4.31}$$

where ρ is the material density (7.87 g/cm^3 for iron), L the length of the detector ($20 \cdot 4.9$ cm) and N_{A} Avogadro's number ($6.022 \cdot 10^{23}$ nucleons/g).

The neutrino cross-section $\sigma_{CC}(E_\nu)$ grows linear with the neutrino energy, and can be conveniently redefined as $\sigma_{CC}(E_\nu) \equiv \frac{\sigma_{CC}}{E_\nu} \times E_\nu$, where $\frac{\sigma_{CC}}{E_\nu}$ could be approximated as a constant: $\sigma_0^{\nu N} = 0.677 \cdot 10^{-38}\mathrm{cm}^2/\mathrm{GeV}$ for the νN cross-section and $\sigma_0^{\overline{\nu} N} = 0.342 \cdot 10^{-38}\mathrm{cm}^2/\mathrm{GeV}$ for the $\overline{\nu} N$ cross-section.

The neutrino flux per unit area and neutrino energy $\phi(x, y; E_\nu)$ integrated over the detector area yields the number of incident neutrinos traversing the detector

$$\Phi(E_\nu) \equiv \int \phi(x, y; E_\nu)\, dA\,. \tag{4.32}$$

Replacing the integration in Equation 4.31 by a sum over the energy weighted average flux in the ith bin $\Phi_i \equiv \Phi(E_i) \cdot E_i$ yields

$$N_{CC}^{\mathrm{calc}} = \sum_i \Phi_i \cdot \sigma_0^{\nu N} \cdot \rho L N_{\mathrm{A}}\,. \tag{4.33}$$

The NOMAD beam *MonteCarlo* NUBEAM [80] can be used to calculate the numbers for $\sum_i \Phi_i$ per *p.o.t.*'s and for the different neutrino species. Table 4.12 summarizes the results for the different components of the neutrino beam. Also listed are the mean values of the different energy spectra together with the ratio of the different neutrino species. The last column represents the calculated number of expected neutrino charged current interactions in the FCAL for (1.8 m)^2 and 10^{19} *p.o.t.'s*. The quoted errors are obtained by varying the fiducial area by 5% and represent an estimation for the systematic error. Together with the total numbers of *p.o.t.*'s listed as $\sum BCT_{\mathrm{SPS}}$ in Table 4.1 this provides the calculated

Component	$< E_\nu >$ [GeV]	Relative flux	$\sum \Phi_i$ [GeV/10^{19} *p.o.t.*]	$N_{CC}^{\rm calc}$ per [10^{19} *p.o.t.*]
ν_μ	25.9	100%	$(15.30 \pm 0.76) \cdot 10^6$	$(4.81 \pm 0.24) \cdot 10^6$
$\overline{\nu}_\mu$	17.7	4.7%	$(7.18 \pm 0.36) \cdot 10^5$	$(1.14 \pm 0.06) \cdot 10^5$
ν_e	38.1	1.4%	$(2.20 \pm 0.11) \cdot 10^5$	$(6.92 \pm 0.35) \cdot 10^4$
$\overline{\nu}_e$	28.9	0.3%	$(3.96 \pm 0.20) \cdot 10^4$	$(0.63 \pm 0.31) \cdot 10^4$

Table 4.12: *Predicted flux at FCAL for a fiducial area of* $(1.8\ m)^2$ *and* 10^{19} *p.o.t.*.

number of FCAL neutrino charged current interactions $N_{CC}^{\rm calc}$ in the different data taking periods in Table 4.14.

To compare the calculated to the measured number of events, the charged current efficiency corrected number of neutrino charged current interactions $N_{\rm CC}^{\rm corr}$ calculated in Section 4.3.5 has to be corrected for several factors.

The lifetime of the NOMAD experiment can be estimated using the delivered total numbers of *p.o.t.*'s $\sum BCT_{\rm SPS}$ and the delivered numbers of *p.o.t.*'s when the experiment was up and taking data, $\sum BCT_{\rm NOMAD}$:

$$LT_{NOMAD} = \frac{\sum BCT_{\rm NOMAD}}{\sum BCT_{\rm SPS}} \,. \tag{4.34}$$

Losses during processing and reconstruction of the recorded data are approximated by the numbers of delivered *p.o.t.*'s for reconstructed runs:

$$\varepsilon_{\rm rec} = \frac{\sum BCT_{\rm FCAL}}{\sum BCT_{\rm NOMAD}} \,. \tag{4.35}$$

Combining both yields:

$$LT_{NOMAD} \times \varepsilon_{\rm rec} = \frac{\sum BCT_{\rm FCAL}}{\sum BCT_{\rm SPS}} \tag{4.36}$$

In addition, the lifetimes of the FCAL triggers (cf. Section 2.3)

$$LT_{\rm trig} = (90 \pm 3)\% \tag{4.37}$$

have to be considered, representing the fraction of time during the runs where the experiment could register interactions.

The latter two are listed in Table 4.13 together with the resulting correction factor for $N_{\rm CC}^{\rm corr}$:

$$\varepsilon_{\rm tot} = LT_{NOMAD} \times LT_{\rm trig} \times \varepsilon_{\rm rec} \,. \tag{4.38}$$

Applied to the values of Table 4.11, the fully corrected number of measured neutrino charged current interactions for the different data taking periods are

	$LT_{NOMAD} \times \varepsilon_{\text{rec}}$	LT_{trig}	ε_{tot}
96_ν	$(93.15 \pm 0.81)\%$	$(90 \pm 3)\%$	$(83.8 \pm 2.9)\%$
97_ν	$(93.37 \pm 0.82)\%$	$(90 \pm 3)\%$	$(84.0 \pm 2.9)\%$
98_ν	$(89.55 \pm 1.00)\%$	$(90 \pm 3)\%$	$(80.6 \pm 2.8)\%$

Table 4.13: *Total NOMAD and FCAL efficiencies.*

compared to the equivalent calculated event numbers in Table 4.14. The calculated numbers are slightly lower than the measured but agree well within the errors for all the single periods. In contrast to Table 4.11 also the values for 1996 agree, indicating that in Section 4.3.5 the number of neutral current interactions was overestimated for this period.

	$N_{\text{CC}}^{\text{corr}}/\varepsilon_{\text{tot}}$ $[10^6]$	N_{CC}^{calc} $[10^6]$	Ratio
96_ν	7.33 ± 0.25	7.02 ± 0.35	1.04 ± 0.06
97_ν	8.15 ± 0.28	7.99 ± 0.40	1.02 ± 0.06
98_ν	6.48 ± 0.23	6.45 ± 0.32	1.01 ± 0.06

Table 4.14: *Fully corrected measured and calculated numbers of ν_μ^{CC} events.*

4.4 Reconstruction of ν_μ^{CC} events

Neutrino charged current interactions are selected using the selection criteria described before in this chapter. For the applied calibration procedure, established in Chapter 3, a comparison between the *MonteCarlo* simulated and reconstructed informations is performed, as well as a comparison between real data and the *MonteCarlo*. To demonstrate the achieved level of agreement, the visible hadronic energy, the energy of the primary muon and the visible neutrino energy distributions are chosen. These may be compared to the ones in References [93] and [94].

4.4.1 Comparison simulated and reconstructed

In order to compare simulated and reconstructed distributions the *Quality* of a variable is introduced.

Quality

The quality of reconstruction of any variable, X, may be defined as

$$Q(X) \equiv \frac{X^{\text{sim}} - X^{\text{rec}}}{X^{\text{sim}}} \tag{4.39}$$

where X^{sim} represents the value of the variable X before detector smearing and reconstruction has been applied to the event (the simulated value) and X^{rec} is the value of X after the event has been passed through the detector simulation and reconstruction algorithms. In this chapter, unless otherwise stated, the term "quality" is synonymous with "quality of reconstruction" and refers to Definition 4.39. The "resolution" and "bias" of a variable are defined to be the width and mean of the quality distribution respectively.

The studied sample is the generated ν_μ^{CC} *MonteCarlo* events. In all comparisons the simulated distributions are shown as histograms and the reconstructed distributions as points.

Hadronic energy resolution

The visible hadronic energy of the event, $E_{\text{had}}^{\text{vis}}$, is constructed as the sum of:

- the visible energy deposited in the FCAL using the algorithms developed in Chapter 3
- and the energy of charged tracks leaking into the drift chambers, assigning a pion mass to those particles which have not been identified.

The energy of the leakage tracks is a second order contribution to the total energy and as such no attempt was made to add tracks arising from secondary interactions in the drift chamber region. Contributions from neutral hadrons measured in the HCAL or from unassociated clusters in the ECAL have been neglected as well. Like this, it is assumed that most of the event energy is absorbed in the FCAL material. This is a safe assumption for interactions occurring in Stacks 1 and 2, and, to a somewhat lesser extend for interactions in Stacks 3. Events in Stack 4 are expected to be dominated by leakage effects and not providing reliable energy measurements.

Figures 4.4 and 4.5 show the comparison of *MonteCarlo* input and reconstructed hadronic energies for interactions originating in the different FCAL stacks. The top plots are simple comparisons in a logarithmic scale, followed by the qualities. The bottom plots show the bias as a function of the measured variable, here $E_{\text{had}}^{\text{vis}}$. As expected, the energy measurement for events occurring in Stack 1 and 2 are reasonably accurate. Leakage effects and unmeasured energy in form of neutral particles become more important for interactions occurring towards the back face of the FCAL, namely Stack 3 and 4.

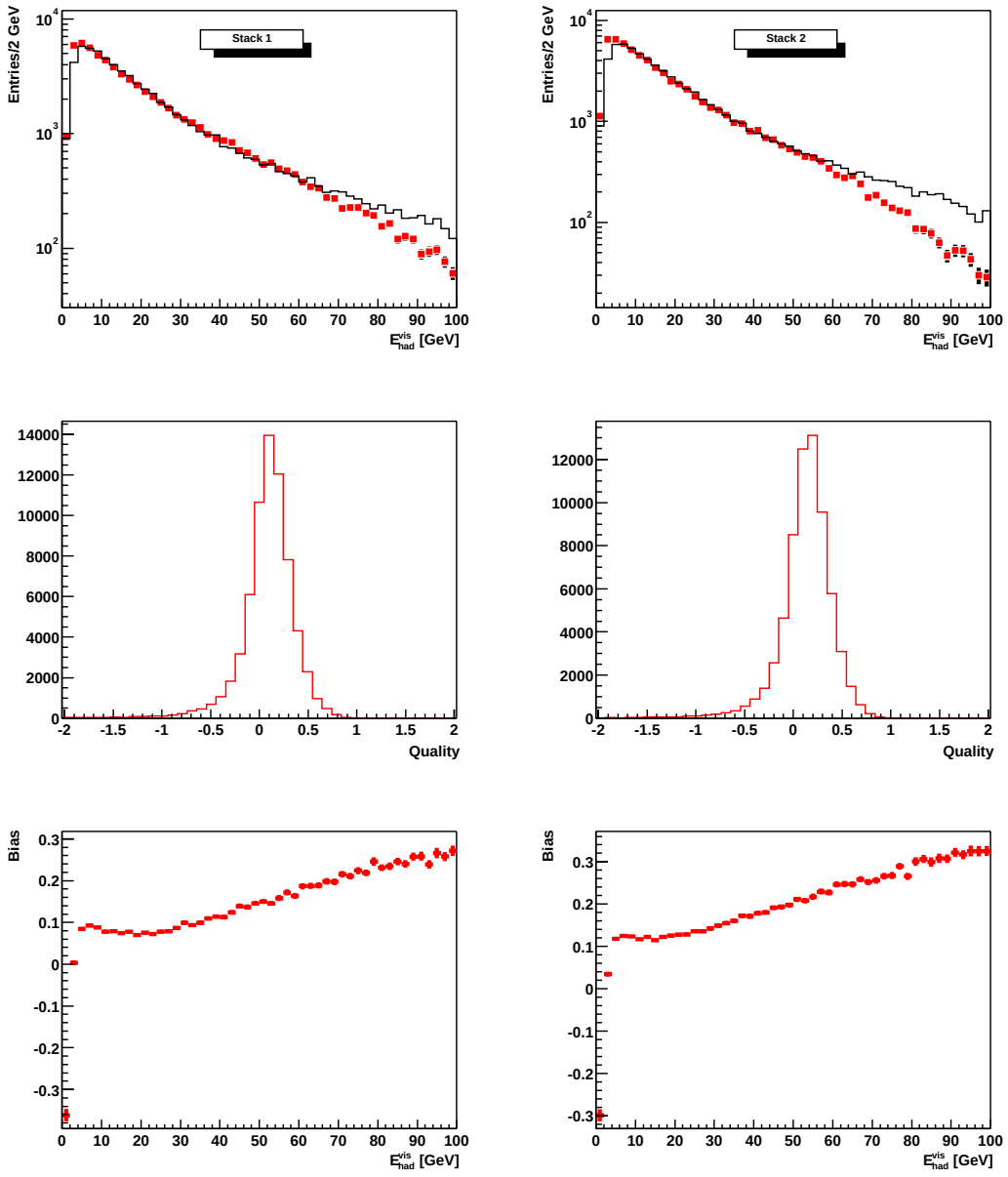

Figure 4.4: *Comparison of MonteCarlo simulated and reconstructed visible hadronic energy E_{had}^{vis} for Stack 1 (left) Stack 2 (right).*

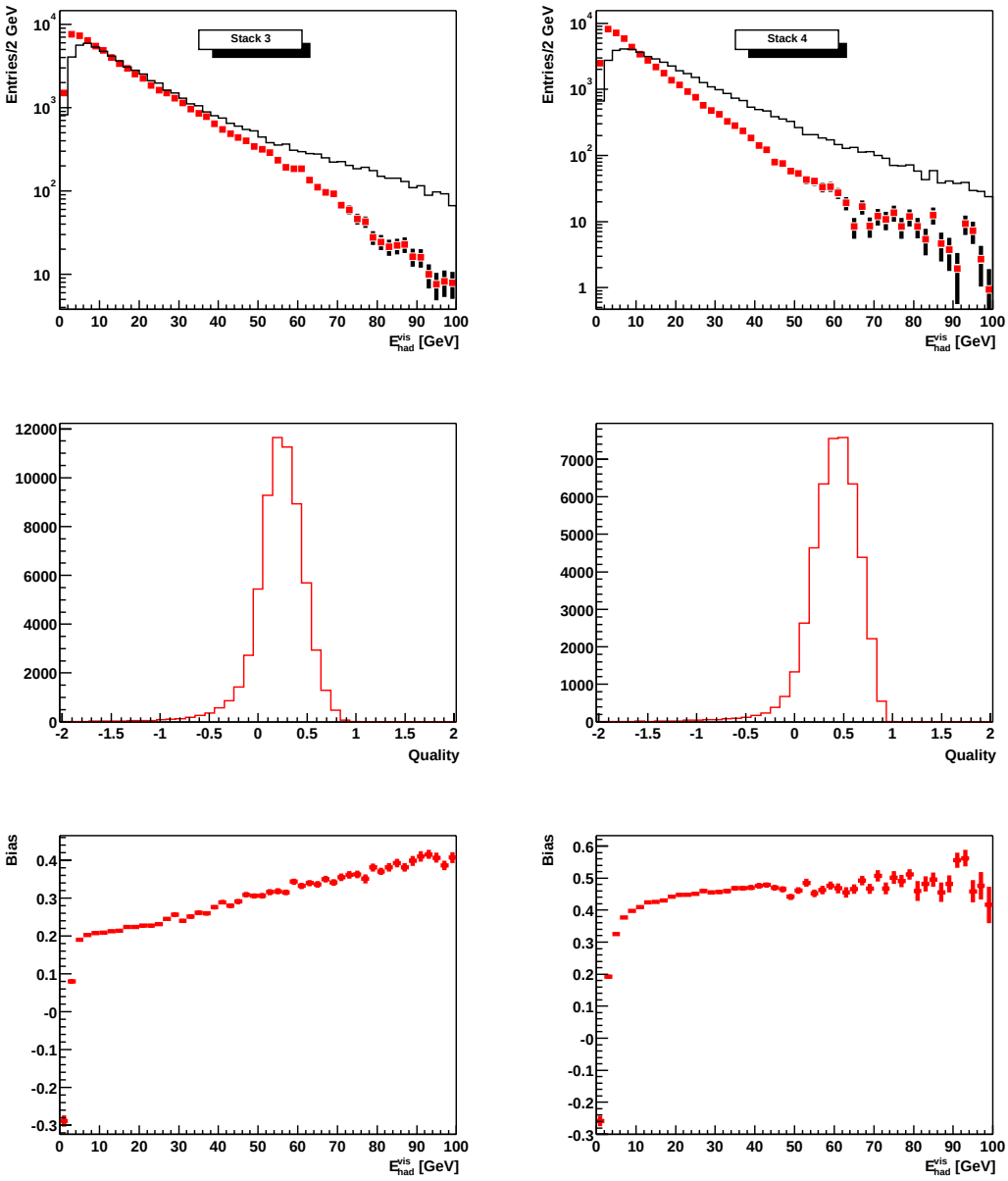

Figure 4.5: *Comparison of MonteCarlo simulated and reconstructed visible hadronic energy E_{had}^{vis} for Stack 3 (left) Stack 4 (right).*

Muon energy resolution

Figure 4.6 shows the reconstruction quality for the energy of the primary muon corrected for the energy loss in the FCAL and coil material as described in Section 4.2.3. Again the top plot is a comparison of simulated and reconstructed values in a logarithmic scale, followed by the quality and the bias as a function of the muon energy. The slight asymmetry in the quality distribution indicates the presence of muons which undergo catastrophic energy loss. As can bee seen, the muon energy is measured with a precision of better than 2% over three orders of magnitude.

Neutrino energy resolution

The visible neutrino energy, E_ν^{vis}, is simply the sum of the visible hadronic energy and the energy of the primary muon and is a good approximation to the actual neutrino energy. The quality of the reconstruction of the neutrino energy is shown in Figures 4.7 and 4.8.

The distributions for E_ν^{vis} show the same qualitative features as those for E_{had}. The resolution is better than the one for E_{had} due to the (usually) well-reconstructed muon.

4.4.2 Comparison data and *MonteCarlo*

In this section the reconstructed hadronic, muon and neutrino energies for muon neutrino charged current interactions in *MonteCarlo* and data are compared.

The *MonteCarlo* sample consists of the simulated ν_μ^{CC} events and the used data sample is that of the 1996 data taking period. All distributions being compared are normalized to the same number of events, where the histograms represents the *MonteCarlo* and the points the data distributions.

Figures 4.9, 4.10 and 4.11 show the distributions for the visible hadronic energy $E_{\text{had}}^{\text{vis}}$, the energy of the primary muon E_μ and the visible neutrino energy E_ν^{vis}, respectively, for events originating in the different FCAL stacks (in a logarithmic scale).

The distributions for $E_{\text{had}}^{\text{vis}}$ agree well for all four stacks. The number of events in the lowest bin is underestimated in the *MonteCarlo* for all stacks. A small excess can be seen for data in the mid energy range for Stacks 2 and 3, and Stack 4 differs slightly in the high energy range.

The shape of the distributions for the muon and neutrino energies differs slightly above an energy of $\simeq 60$ GeV. The neutrino beam consists predominantly of ν_μ arising from the decay of π^+ and K^+ mesons in the beam. Neutrinos with energies less than 60 GeV come mainly from π^+ decays, whereas those possessing and energy above 60 GeV originate from K^+ decays. The shape of the neutrino spectrum, and hence the shape of the primary muon energy spectrum, is therefore

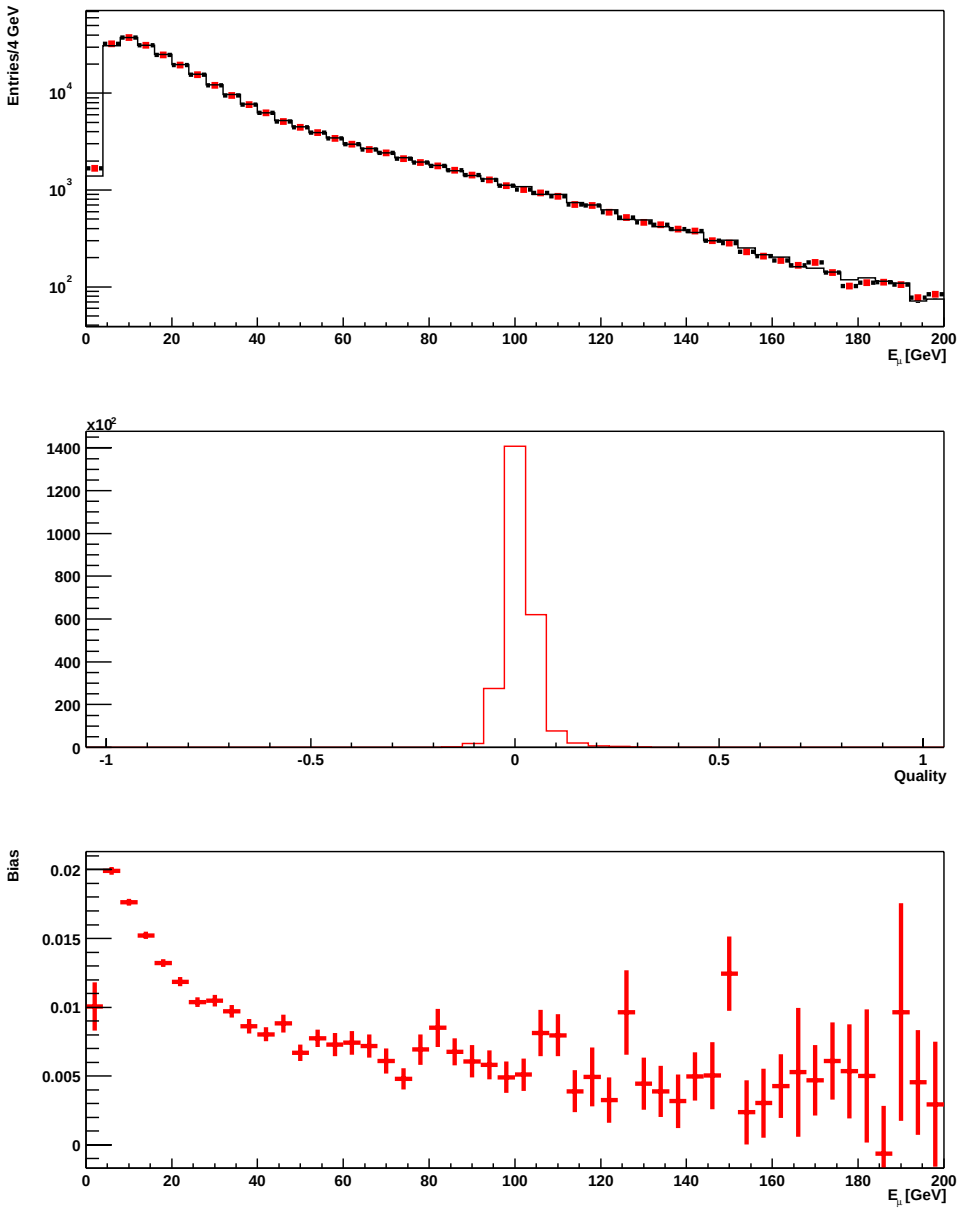

Figure 4.6: *Comparison of MonteCarlo simulated and reconstructed primary muon energy* E_μ.

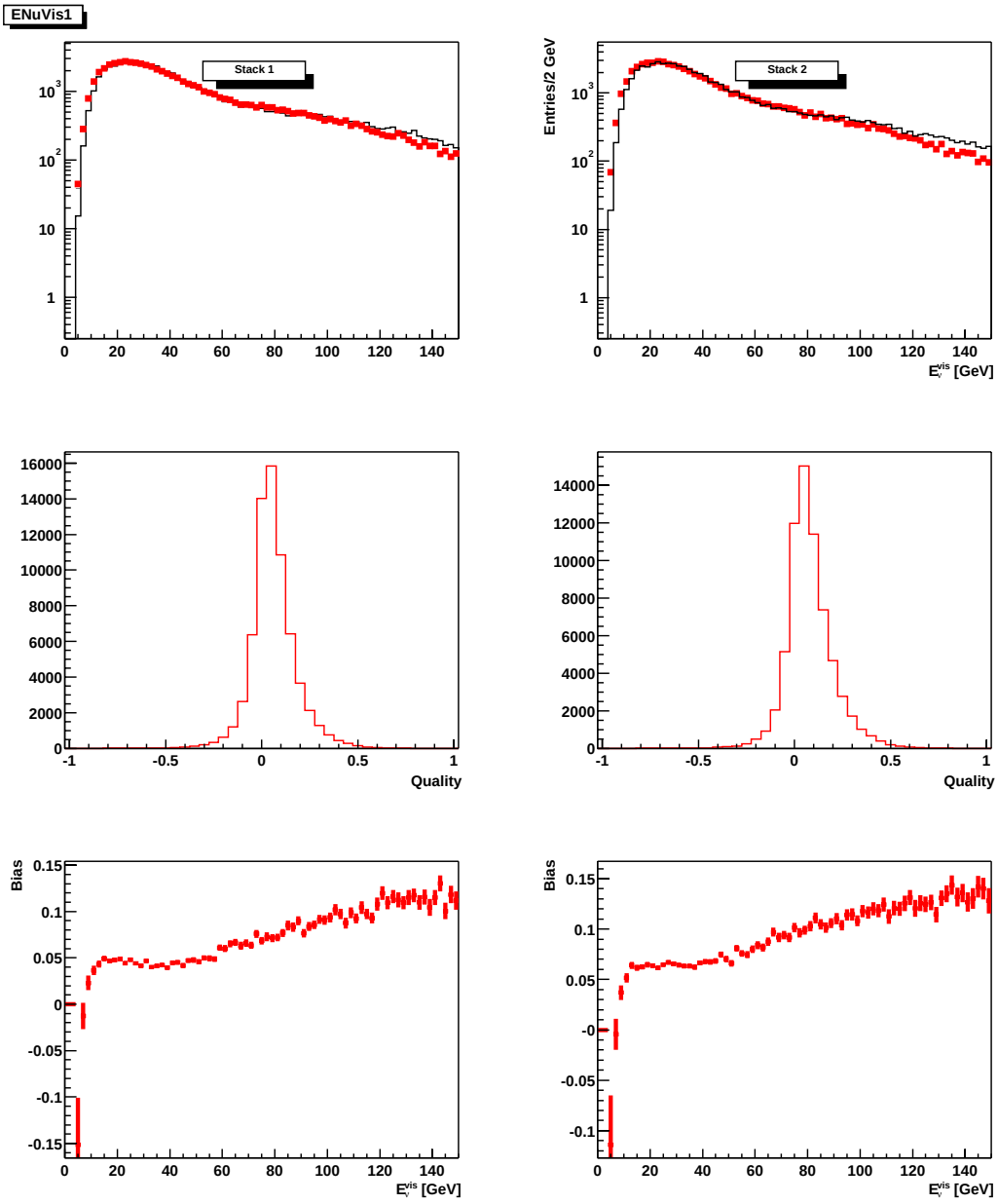

Figure 4.7: *Comparison of MonteCarlo simulated and reconstructed visible neutrino energy E_ν^{vis} for Stack 1 (left) Stack 2 (right).*

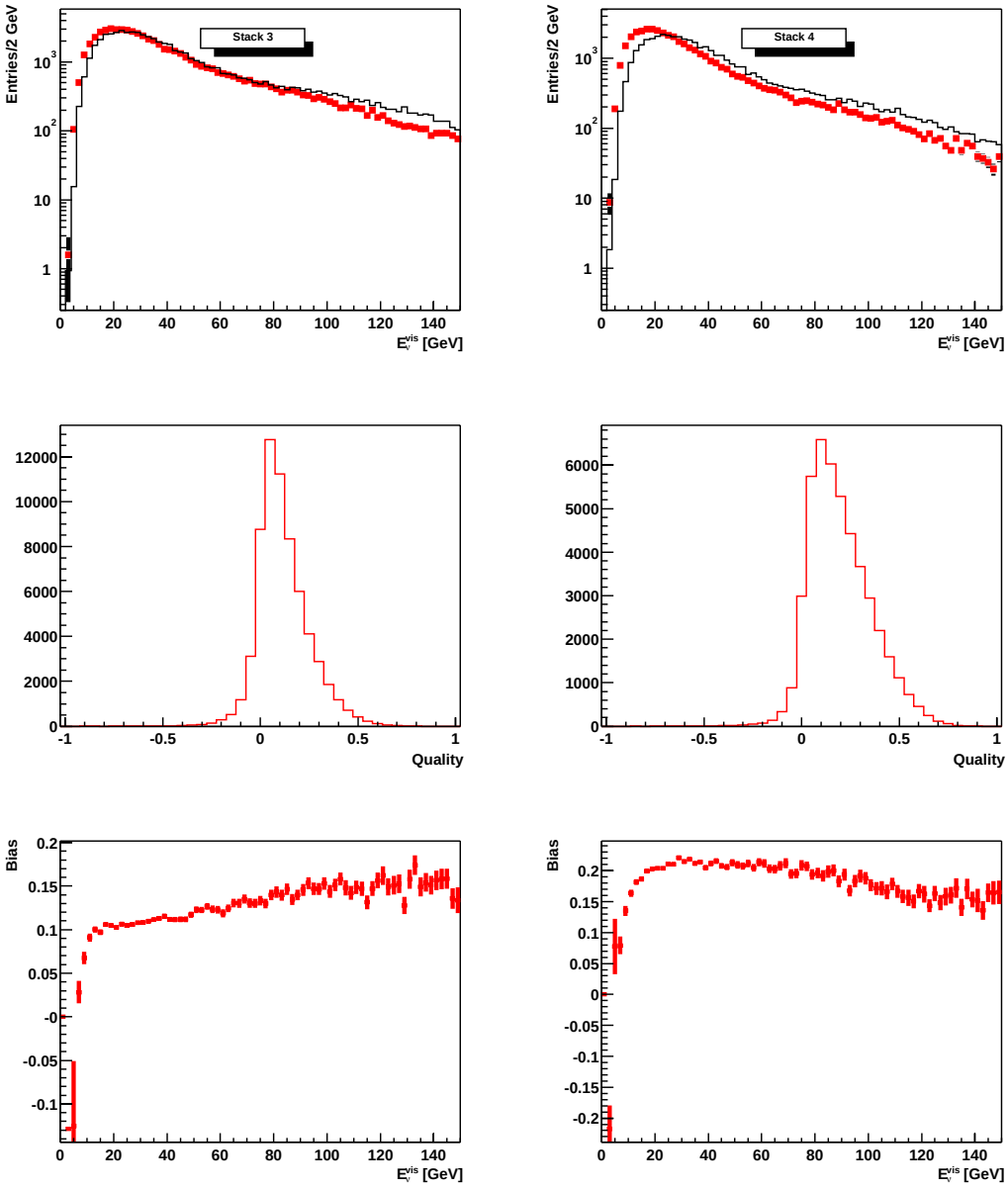

Figure 4.8: *Comparison of MonteCarlo simulated and reconstructed visible neutrino energy E_ν^{vis} for Stack 3 (left) Stack 4 (right).*

dependent upon the ratio of pions to kaons produced in the proton-beryllium target. Another possible reason for the discrepancy might be that the structure functions used in the calculation of the cross-section do not exactly describe the NOMAD data.

However, it should be noted that the remaining discrepancy is small and the agreement is good.

4.5 Event timing

When the trigger system establishes that a required condition of subdetector signals is fulfilled and the complete detector readout is initiated, signal timing information is recorded within the event. This makes it possible to decide at the analysis level if the signals of the various subdetectors are correlated in time (within a certain resolution) and belong to the same neutrino interaction and to reject events consisting of a random overlay of a neutrino interaction in one detector with a second neutrino or cosmic ray interaction in another subdetector.

In this section the *Common Stop* of the NOMAD trigger is introduced followed by an explanation of the available time information of the two main subdetectors used in the further analysis, the front calorimeter and the drift chambers, before they are combined to measure the timing resolution. A detailed description is given, since the FCAL timing information and the method of combining these subdetector informations have not been used before in other analyses.

Trigger timing and *Common Stop*

When an interaction in of one of the subdetectors occurs signals are formed in an electronics chain specific for each detector. Typically other subdetectors are also traversed by particles produced in the primary interaction and also send out signals. All these information is collected at a central place to form the trigger signals, the trigger system MOTRINO.

A particle traversing a detector with a dimension of about 10 meters at the speed of light ($\simeq 30$ cm/ns) produces signals with non-negligible time differences. In addition each subdetector system has different signal propagation times due to the type of detector, cabling ($\simeq 5$ ns/m) and electronics.

After the trigger system has synchronized and combined the different signals needed to form a selected trigger such as $(\overline{V}_8 \times \mathrm{FCAL}' \times T_1 \times T_2)$ it sends out a so-called *Common Stop* signal to all subdetectors and the data acquisition system indicating a complete detector readout will follow.

At the time of the readout each subdetector has to provide the event information which has a different time stamp *w.r.t.* to the *Common Stop*. For the FCAL *ADC* signals e.g. an additional 400 ns delay (see Section 3.2.4) had to be introduced to make it possible to synchronize it with the readout gate signal.

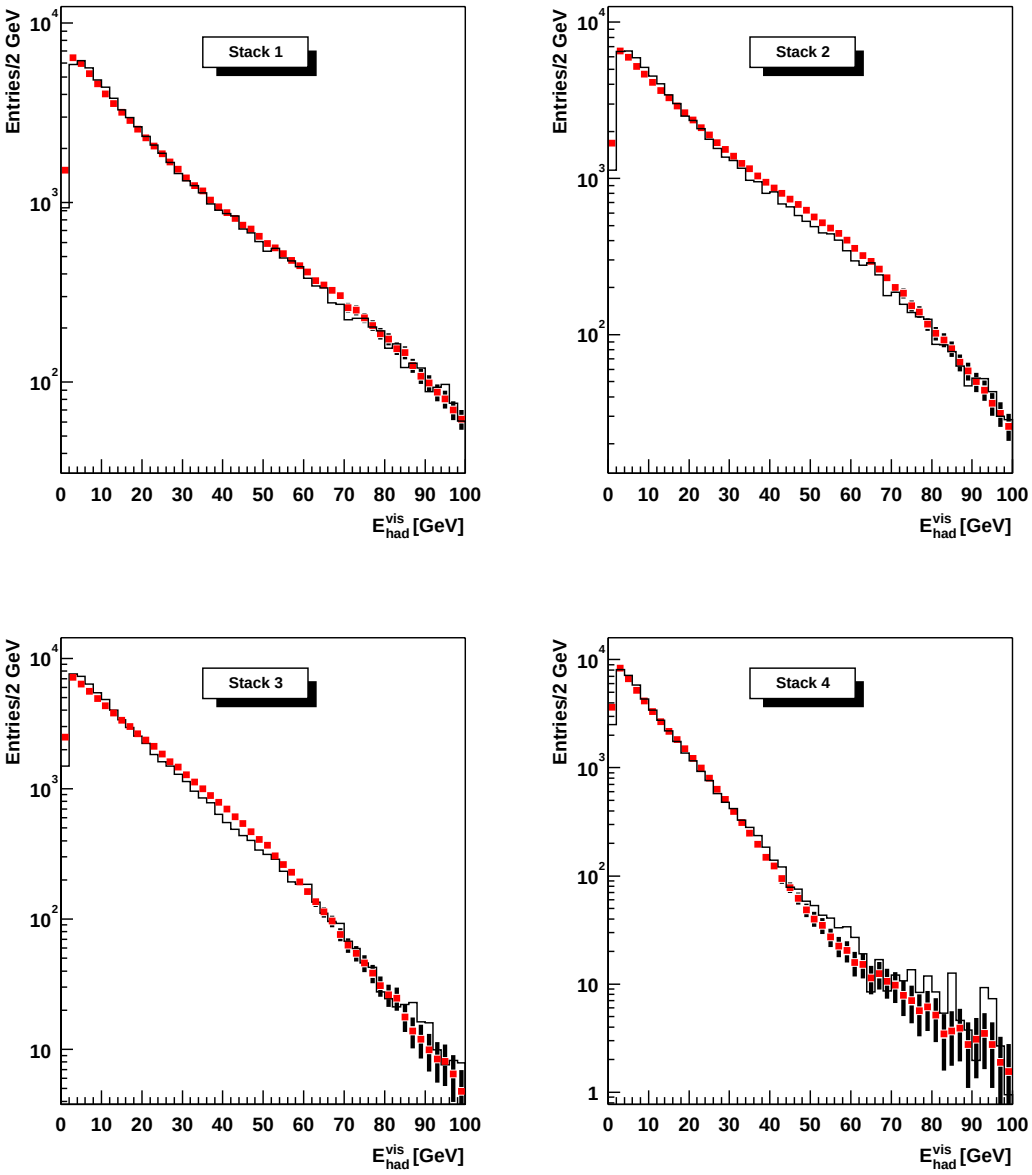

Figure 4.9: *Comparison of data and MonteCarlo distributions for the visible hadronic energy E^{vis}_{had} for events originating in the different stacks.*

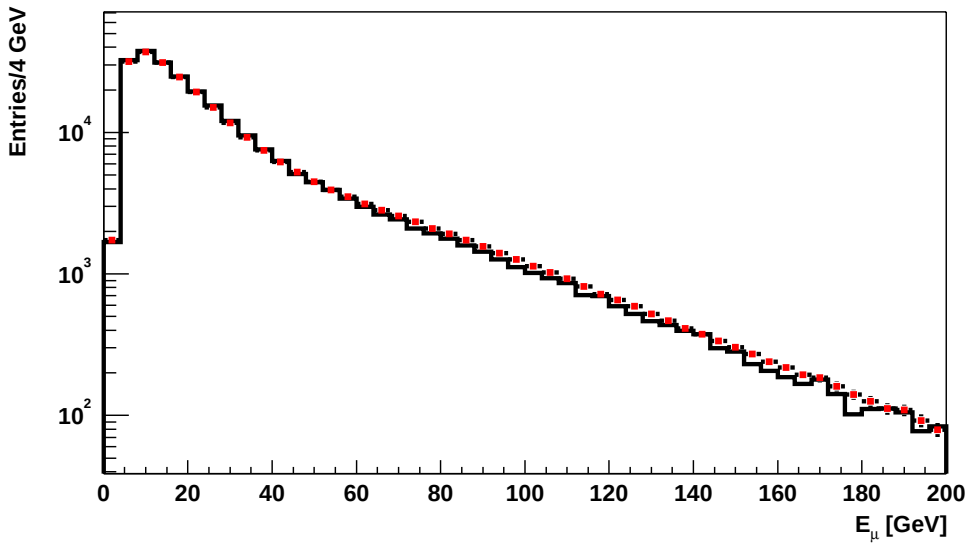

Figure 4.10: *Comparison of data and MonteCarlo distributions for the muon energy E_μ for events originating in the different stacks.*

FCAL timing

The data acquisition system reads out the FCAL *TDCs* (64 μs time window with 1 ns resolution) and stores two buffer entries representing the minimal and maximal time of an entry *w.r.t.* the *Common Stop*, $t_{0,\min}$ and $t_{0,\max}$, for each module. The occupancies of the *TDC* buffers are low, typically even $t_{0,\min} = t_{0,\max}$.

To estimate the overall event time of the FCAL the energy weighted mean of all module times is build

$$T_0 \equiv < t_0 >= \frac{\sum_i t_{0,i} \cdot E_i}{\sum_i E_i} \tag{4.40}$$

Since for each module two times $t_{0,\min}$ and $t_{0,\max}$ are available, the ones are selected which minimize the variance of the mean (a kind of truncated mean)

$$\sigma^2_{<t_0>} = \frac{\sum_i (t_{0,i} - < t_0 >)^2 \cdot E_i}{\sum_i E_i} \tag{4.41}$$

Modifications in the trigger system or changes in the signal propagation times (e.g. caused by temperature effects) can shift these values. In the detector simulation only particle propagation in the detector is included for the simulated timing information, so typical values are near zero. To make the calculation of the FCAL time independent of effects like these, the mean values $< T_0 >_{\text{trig}}$ for

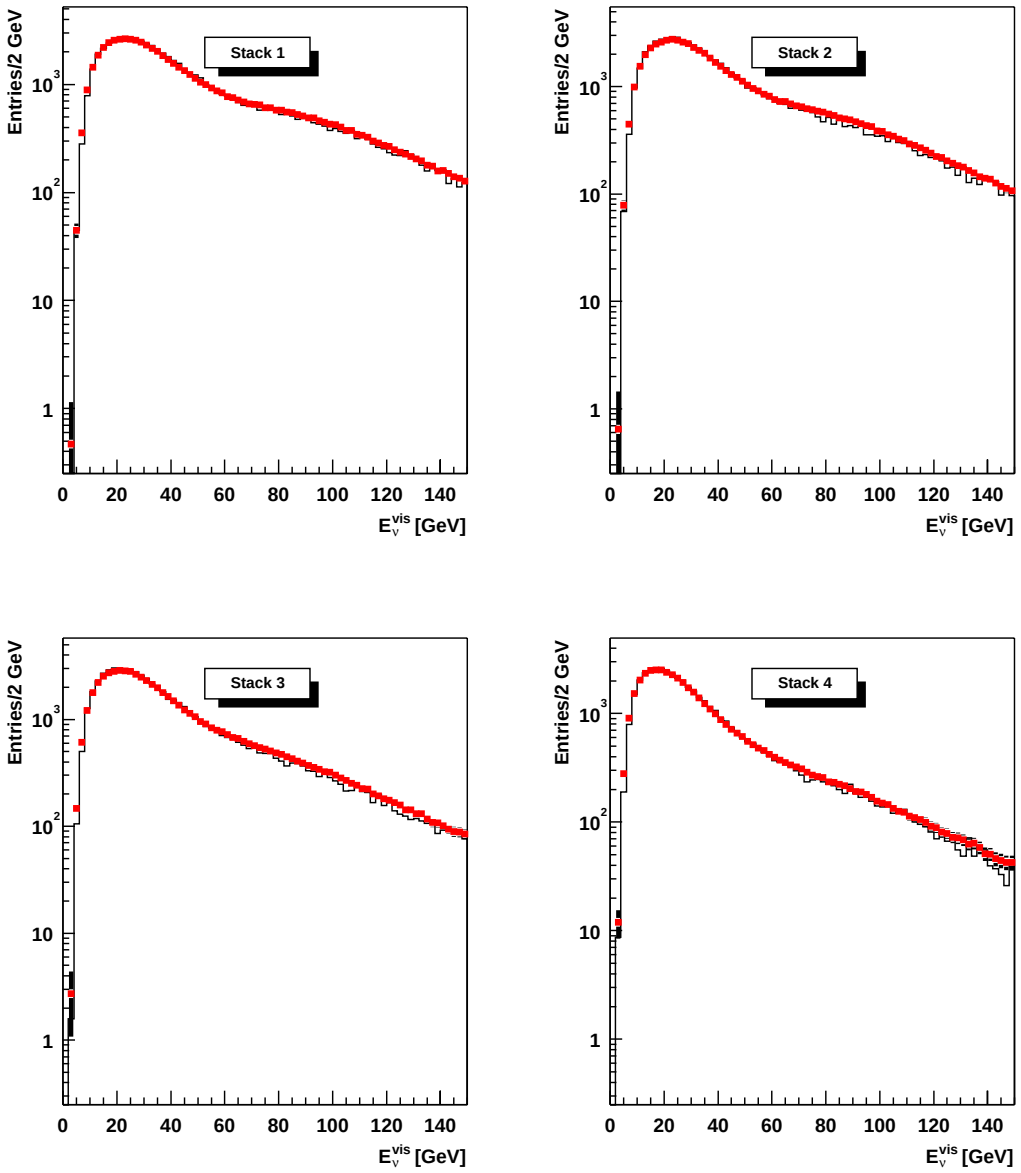

Figure 4.11: *Comparison of data and MonteCarlo distributions for the visible neutrino energy E_ν^{vis} for events originating in the different stacks.*

both FCAL triggers for each run (typically several hours of data taking) were calculated and each FCAL event in such a run gets its attributed time:

$$T_{\mathrm{FCAL}} = < T_0 >_{\mathrm{trig}} - T_0 \tag{4.42}$$

Positive times mean that the event occurs later than the average time, because FCAL times are not corrected for the *Common Stop* time difference.

Drift chamber track timing

Track finding and fitting in the NOMAD drift chamber reconstruction process can be divided into four phases:

- **Triplet finding**: The NOMAD drift chambers are made of three sensitive planes at 0° and ±5° stereo angles, thus the right combination of three hits has to be found.

- **Helix search**: With at least three triplets a test of whether they belong to the same helix may be performed. A helix is uniquely defined by six parameters.

- **Triplet collection**: With approximate initial values for the helix parameters triplets in a road around the helix can be collected and assigned to tracks.

- **Track fitting**: Track candidates can now be fitted, i.e. position, direction and curvature can be estimated by a procedure which should be optimal in the statistical sense.

For a track in vacuum the knowledge of the six helix parameters for a single point would be sufficient to describe the helix in each point. In the presence of matter random perturbations such as multiple scattering have to be taken into account, complicating the fitting procedure. Therefore in NOMAD the so-called Kalman filter technique [117] was chosen. The parameters fitted are the coordinates x and y, the signed radius $1/R$, the so-called dip angle $\tan\lambda$, the angle ϕ of the helix tangent to the bending plane and t_0. The latter makes it possible to cope with trigger time jitter and to enable fitting of off-time tracks in a certain time window. At the level of the analysis the t_0 of the track at its first hit is available; it is already corrected for the *Common Stop* offset (given as a constant for each trigger type by the reconstruction program) in such way that a greater value means later in time. The track fitting technique is able to reconstruct tracks within a time window of $\simeq 30$ ns around this starting value with high efficiency.

As for the FCAL (see previous section) the t_0 at its first hit is corrected by the average run track time calculated from the muon tracks of ν_μ^{CC} interactions:

$$T_{\rm Trk} =< t_0 >_{\rm trig} - t_0 \tag{4.43}$$

Here positive times mean that the track occurs earlier than the average time.

Assuming that the track is originating from an interaction in the FCAL it is flight time corrected:

$$T_{\rm Trk}^{\rm c} = T_{\rm Trk} - \Delta r/\beta c \tag{4.44}$$

using the track parameters at its first hit

$$\beta = |\vec{p}_{\rm Trk}|c/E_{\rm Trk} \tag{4.45}$$

and the distance in space between the primary vertex (PV) and the first hit position of the track

$$\Delta r = |\vec{r}_{\rm Trk} - \vec{r}_{\rm PV}| \tag{4.46}$$

Combination of FCAL and DC timing information

To build the time difference of the FCAL and DC timing signals Equations 4.42 and 4.44 have to be *added* (because of their different internal time arrows or signs, see explanations before):

$$\Delta t^{\rm c} = T_{\rm FCAL} + T_{\rm Trk}^{\rm c} \tag{4.47}$$

By this definition the resulting sign of $\Delta t^{\rm c}$ represents:

$$\Delta t^{\rm c} \ < 0: \quad \text{DC later than FCAL} \tag{4.48}$$

$$\Delta t^{\rm c} \ > 0: \quad \text{DC before FCAL} \tag{4.49}$$

Figure 4.5 shows $\Delta t^{\rm c}$ for primary muons of ν_μ^{CC} interactions (data) in the FCAL. Because of their high and well measured momentum the resolutions for primary muons can be considered as the best possible ones.

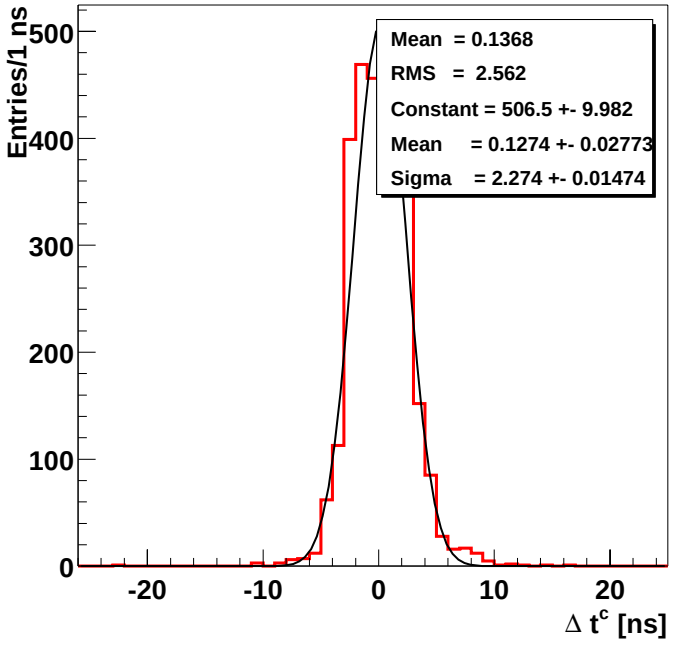

Figure 4.12: *Timing resolution of muons from FCAL* ν_μ^{CC} *interactions (data).*

Chapter 5

Simulation of Neutral Heavy Leptons

In this chapter the applied method for *MonteCarlo* generation of neutral heavy lepton events is described and results from the simulations are discussed.

5.1 Production and decay

Neutral heavy lepton events are generated in the framework of the NOMAD event generator NEGLIB [82] (see Chapter 2.4) modified according to the GLR model [11] described in Section 1.6.1 with the relevant equations recalled below.

In a Standard Model weak neutral current interaction $\nu_\mu N \to \nu_\mu X$ the outgoing massless lepton is replaced by the massive neutral heavy lepton. Events are only generated if the fraction of center of mass energy carried by the struck quark is above the neutral heavy lepton mass threshold to be generated ($xs > m^2_{\mathcal{N}_\mu}$) and into the event kinematics the mixing parameter $|U_{\mu\mu}|^2$ as well as the proper mass suppression factor $S_m = \left(1 - \frac{m^2_{\mathcal{N}_\mu}}{xs}\right)^2$ are included (Equation 1.34):

$$\begin{aligned} d\sigma(\nu_\mu N \to \mathcal{N}_\mu X) =& d\sigma(\nu_\mu N \to \nu_\mu X) \times \\ & |U_{\mu\mu}|^2 \times \left(1 - \frac{m^2_{\mathcal{N}_\mu}}{xs}\right)^2 \times \Theta(xs - m^2_{\mathcal{N}_\mu}) \times \mathrm{BR}. \end{aligned} \tag{5.1}$$

Within the event generator the LEPTO [83] package then takes care about the NHL production event kinematics.

The neutral heavy lepton decay is handled by the JETSET [85] package taking into account the proper lifetime (Equation 1.38):

$$\tau_{\mathcal{N}_\mu} = 4.51 \cdot 10^{-12}\ \mathrm{sec} \cdot \left(\frac{m_{\mathcal{N}_\mu}}{1\ \mathrm{GeV}/c^2}\right)^{-5.19} \cdot |U_{\mu\mu}|^{-2} \tag{5.2}$$

Within JETSET the NHL decay modes listed in Table 1.1 were included according to their branching ratios BR and can be selected individually or as bundles. The NHL decay is implemented using a rather simple phase-space type generator, i.e. no dynamics (matrix elements) is involved to avoid additional model dependent assumptions about NHL properties. This means e.g. polarization effects resulting in non-isotropic distributions of the decay products are not simulated.

5.2 Results from simulation

Neutral heavy lepton events in the NOMAD front calorimeter with masses 1 to 6 GeV/c^2 were generated in steps of 0.5 GeV/c^2 with mixing parameters corresponding to the estimated sensitivity calculated in [67] shown in Figure 1.4 for the three decay modes relevant for this analysis:

$$\mathcal{N}_\mu \rightarrow \mu^- \mu^+ \nu_\mu$$

$$\mathcal{N}_\mu \rightarrow \mu^- e^+ \nu_e$$

$$\mathcal{N}_\mu \rightarrow \mu^- X$$

Figures 5.1, 5.2 and 5.3 show displays of generated events [118, 119] for the different decay types with $m_{\mathcal{N}_\mu} = 3$ GeV/c^2. Only the reconstructed information from FCAL, drift and muon chambers are depicted in the four different views.

Neutrino energy, NHL energy and production angle

The energy distribution E_ν of incoming neutrinos ν_μ producing neutral heavy leptons $\mathcal{N}_\mu$ of mass 3 GeV/c^2 is shown in Figure 5.4. Figures 5.5 and 5.6 show the corresponding neutral heavy lepton energy spectrum E_{NHL} and the opening angle Θ_{NHL} of the produced NHL *w.r.t.* the neutrino beam respectively.

To illustrate the effect of the neutral heavy lepton mass, the means and widths (as the RMS [1]) of these distributions are shown in Figures 5.7, 5.8 and 5.9 vs. the NHL mass generated. For increasing mass only incoming neutrinos with sufficient energy are able to produce the heavier $NHLs$, shifting the mean to higher values. Therefore also the mean energy of the produced $NHLs$ becomes higher and the opening angle decreases because of the resulting Lorentz boost (from the rest frame of the NHL to the laboratory system).

[1] **R**oot **M**ean **S**quare

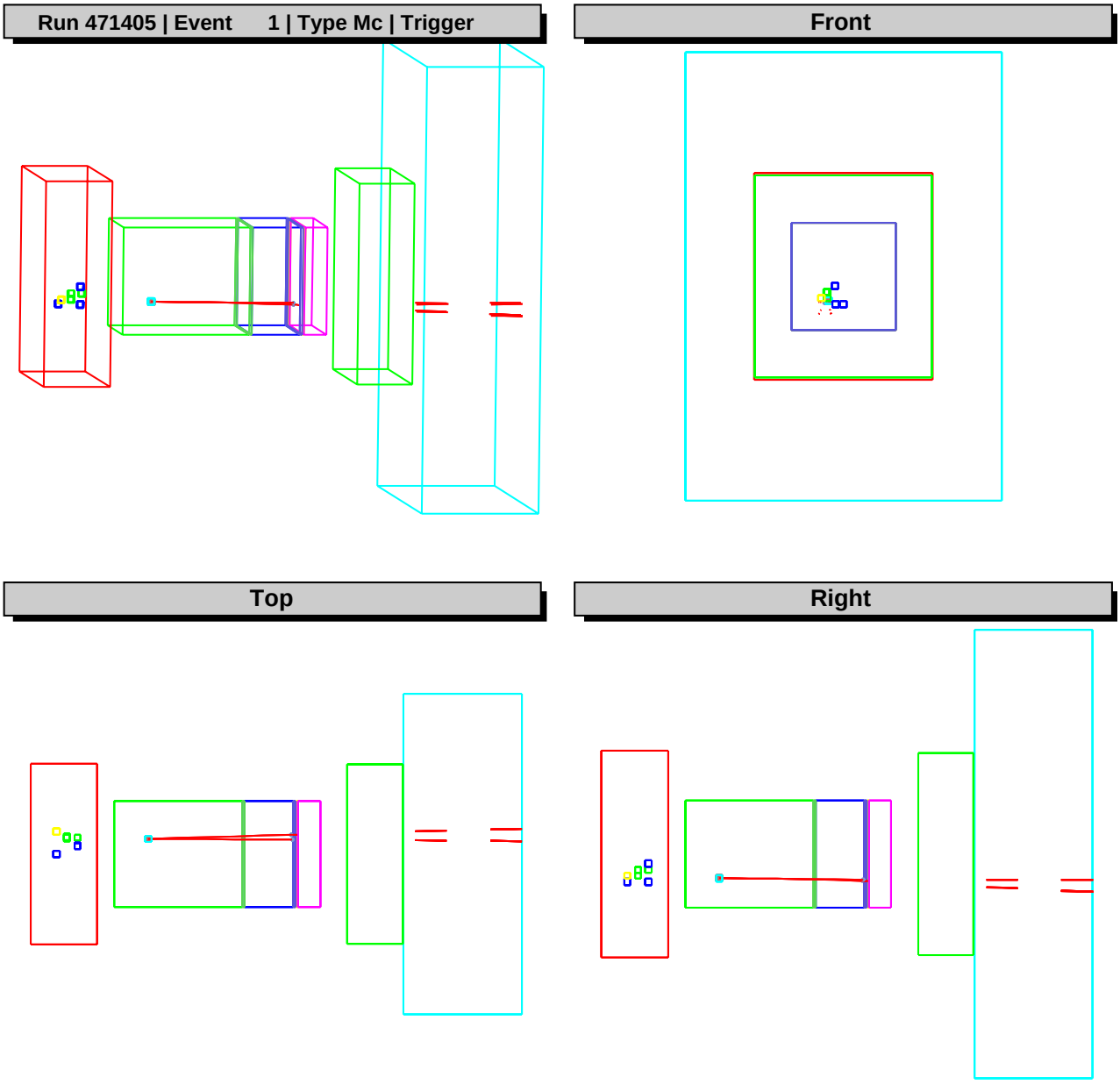

Figure 5.1: *Event display of a simulated* $\mathcal{N}_\mu \rightarrow \mu^-\mu^+\nu_\mu$ *event.*

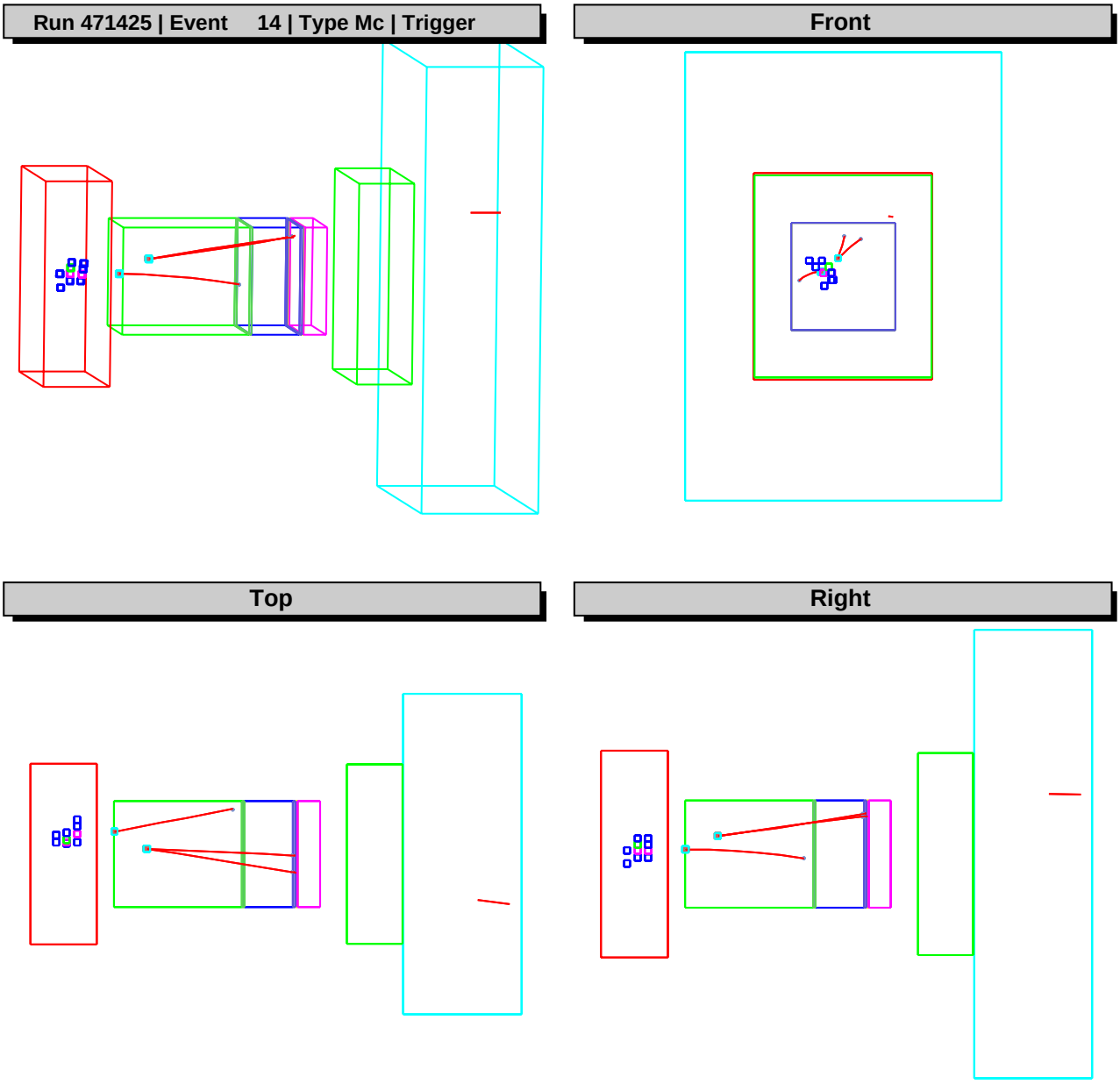

Figure 5.2: *Event display of a simulated* $\mathcal{N}_\mu \to \mu^- e^+ \nu_e$ *event.*

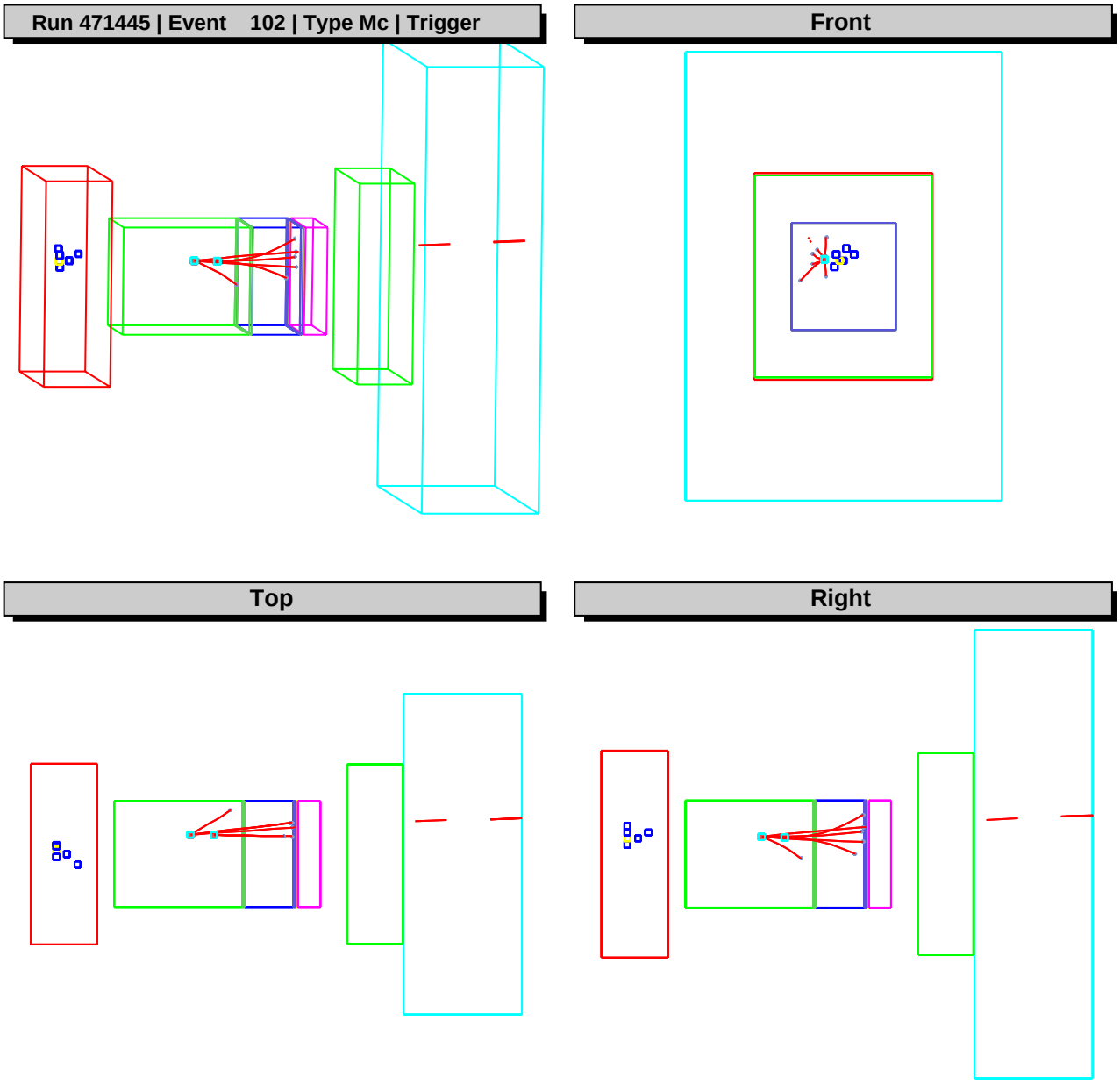

Figure 5.3: *Event display of a simulated* $\mathcal{N}_\mu \to \mu^- X$ *event.*

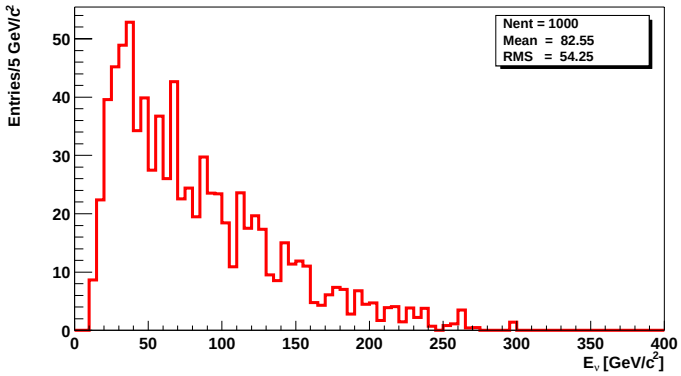

Figure 5.4: *Energy distribution of incoming neutrino for production of NHL with mass 3 GeV/c^2.*

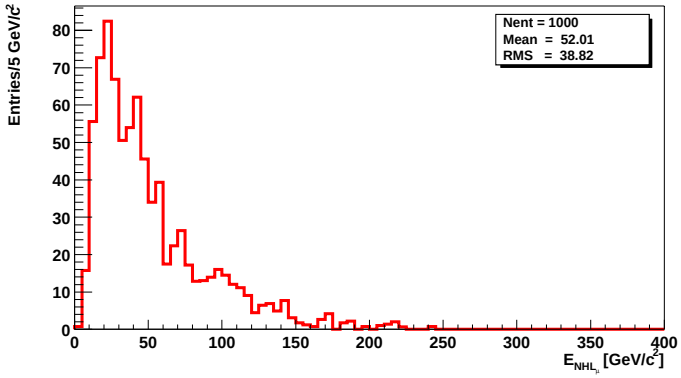

Figure 5.5: *Energy distribution of produced NHL with mass 3 GeV/c^2.*

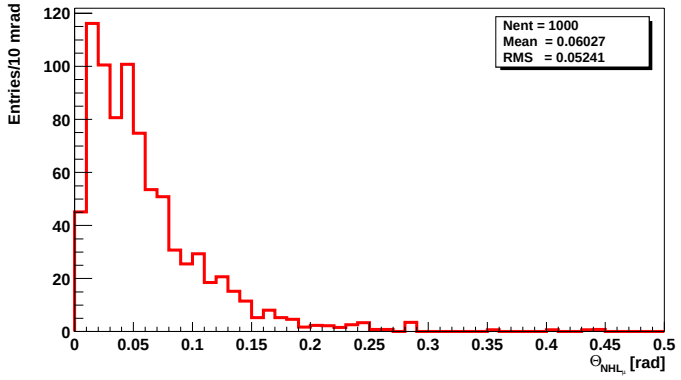

Figure 5.6: *Angular distribution of produced NHL w.r.t. neutrino beam for NHL with mass 3 GeV/c^2.*

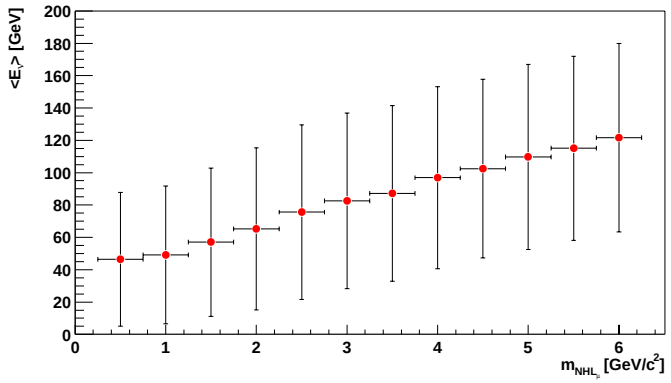

Figure 5.7: *Mean neutrino energy and width (error bars indicate RMS) for NHL production vs. NHL mass.*

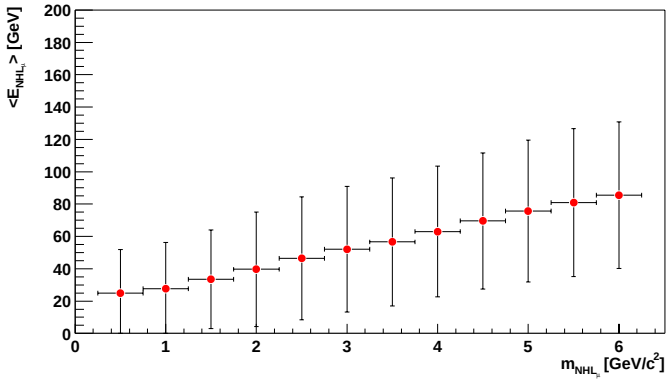

Figure 5.8: *Mean energy and width of produced NHL (error bars indicate RMS) vs. NHL mass.*

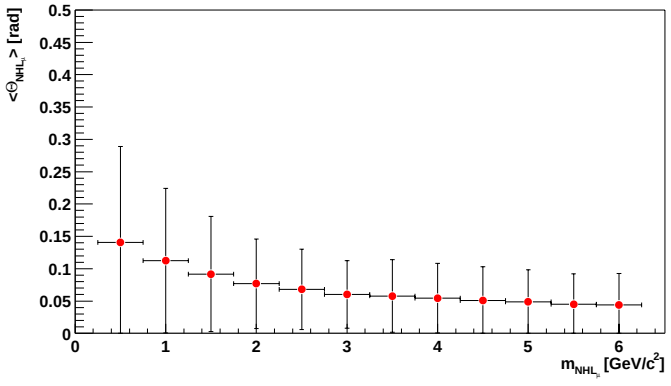

Figure 5.9: *Mean angle and width (error bars indicate RMS) of produced NHL w.r.t. neutrino beam vs. NHL mass.*

Mass suppression factor

The kinematic suppression factor

$$S_m = \left(1 - \frac{m^2_{\mathcal{N}_\mu}}{xs}\right)^2 \quad \text{with} \quad s = 2E_\nu m_{\text{nucleon}} + m^2_{\text{nucleon}}, \tag{5.3}$$

where E_ν = energy of the incident neutrino and m_{nucleon} = mass of the involved nucleon, enters directly into the neutral heavy lepton production and depends on the present neutrino beam spectrum as well on the neutral heavy lepton mass.

Using the NOMAD beam simulation NUBEAM [80] (see Section 2.4) providing the simulated muon neutrino energy spectrum $\Phi(E_\nu)$ of the SPS wideband beam in combination with Equation 5.1 one can calculate the integrated suppression factor as a function of the NHL mass:

$$S_m(m_{\mathcal{N}_\mu}) = \frac{\int \left(1 - \frac{m^2_{\mathcal{N}_\mu}}{xs}\right)^2 \Phi(E_\nu) dE_\nu}{\int \Phi(E_\nu) dE_\nu}. \tag{5.4}$$

The resulting $S_m(m_{\mathcal{N}_\mu})$ shown in Figure 5.10 can be interpreted as a multiplicative factor in the neutral heavy lepton production probability (with $|U_{\mu\mu}|^2 = 1$) reducing the sensitivity of this experiment by a factor of $\simeq 10$ for NHL masses $\gtrsim 4.5$ GeV/c^2.

Production probability

Building the ratio of the integrated cross-sections for neutral heavy lepton production and standard ν_μ weak neutral current interactions via Equation 5.1 folded in the geometrical acceptance, i.e. that the neutral heavy lepton is produced inside the FCAL volume and the decay occurs inside the NOMAD drift chamber volume, provides the NHL production probability *w.r.t.* standard ν_μ weak neutral current interactions in the $|U_{\mu\mu}|^2 \times m_{\mathcal{N}_\mu}$ plane:

$$P_{\mathcal{N}_\mu} = \frac{\int d\sigma(E_\nu, |U_{\mu\mu}|^2, m_{\mathcal{N}_\mu}) \Phi(E_\nu) dE_\nu}{\int d\sigma(E_\nu, m = 0) \Phi(E_\nu) dE_\nu}. \tag{5.5}$$

The result is shown in Figure 5.11 as a contour plot for different probabilities.

Together with the total number of ν_μ^{NC} events and folding in the reconstruction and selection efficiencies (to be determined in Chapter 6) these probabilities determine the sensitivity of the experiment in the $|U_{\mu\mu}|^2 \times m_{\mathcal{N}_\mu}$ plane.

The shape of the contours can be understood by the interplay of the NHL mass and the mixing parameter $|U_{\mu\mu}|^2$ on the NHL lifetime Equation 5.2: for the given experimental setup, the NHL generated in the FCAL target has to travel some distance to enter the drift chamber decay volume, so it needs to have some minimal lifetime to reach the decay volume and on the other hand, if the lifetime is too large, a great fraction decays having passed the analyzer.

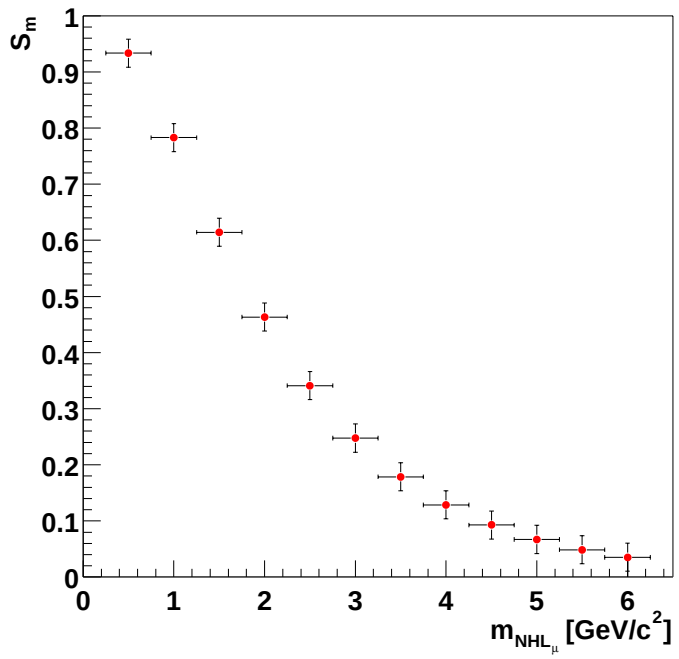

Figure 5.10: *Integrated mass suppression factor as a function of the neutral heavy lepton mass.*

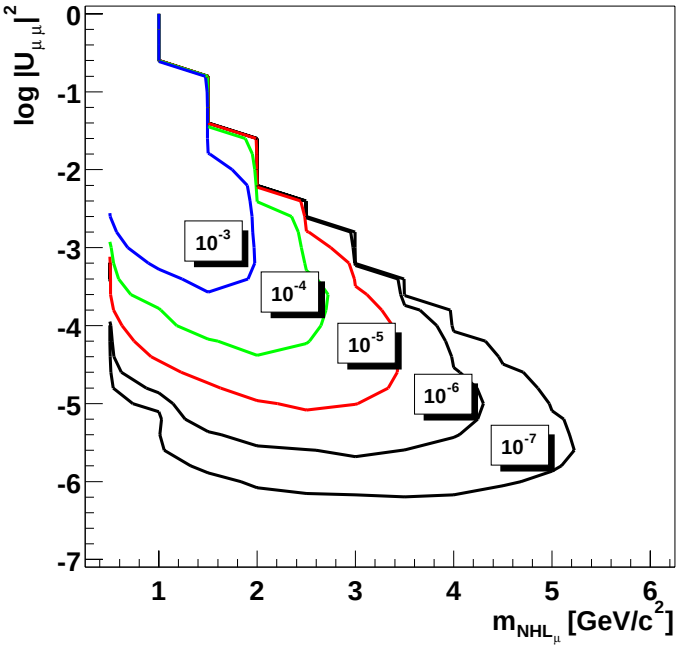

Figure 5.11: *NHL production probability w.r.t. standard neutral current interactions in the* $|U_{\mu\mu}|^2 \times m_{\mathcal{N}_\mu}$ *plane.*

Chapter 6

Search for Neutral Heavy Leptons

As already outlined, the combination of an instrumented neutrino target (FCAL) followed by an instrumented decay region (NOMAD detector) allows to study the production and decay of an anomalous or non-Standard-Model neutral heavy particle. The heavy target is providing a large event statistics, while the light decay analyzer with its excellent measurement capabilities allows to study the properties of the decay products and to keep the number of possible background events small.

An neutral heavy particle $\mathcal{N}$, once produced in the FCAL in a neutrino or "neutrino-like" neutral current interaction, would traverse into the NOMAD detector. The search strategy is to locate a deep-inelastic neutral current interaction in the FCAL detector and to look for a temporally and kinematically correlated decay vertex in the NOMAD detector using:

- the very good lepton identification ($e^{\pm}$,$\mu^{\pm}$) in NOMAD
- the kinematical reconstruction capabilities of NOMAD
- the precise event timing measurement of both detectors

The experimental search is limited by two main sources of background which on the other hand can be measured in the experiment with the help of the available statistics of charged current events:

- **Overlays**
  The random overlap of two uncorrelated neutrino interactions in the upstream detector and in the analyzer volume. The lightness of NOMAD and a good time resolution in both detectors ($\lesssim$ 10 ns) reduce this background. Further, overlay background events of random coincidences of two CC events make it possible to measure the overlay background.

- **Neutral hadron punchthrough**
  The interaction and decay of secondary neutral hadrons produced at the primary interaction vertex in the FCAL. Charged current events occurring in the FCAL provide an *in situ* measure of the hadron punchthrough rates and properties.

Further reduction of background may be achieved by the precise measurement of particle momenta in the NOMAD drift chambers, comparing kinematical quantities of the neutral heavy particle decay products with the background sources.

The possibility to very cleanly study the various decay modes of the heavy particle allows to perform a quasi model-independent analysis, free from assumptions of production, the Lorentz structure of the currents, and most importantly the decay modes of the neutral heavy particle.

In this thesis the results of the search are interpreted in the context of a neutral heavy lepton as described in Chapter 1. A search for a muon type neutral heavy lepton $\mathcal{N}_\mu$ is performed with its two leptonic and one semi-leptonic decay modes:

- **Muonic**: $\mathcal{N}_\mu \rightarrow \mu^- \mu^+ \nu_\mu$
- **Electronic**: $\mathcal{N}_\mu \rightarrow \mu^- e^+ \nu_e$
- **Hadronic**: $\mathcal{N}_\mu \rightarrow \mu^- X$

In this chapter first an event preselection common for all three NHL decay modes is performed. The concept of a "blind box" analysis is introduced and applied to the NHL search. The two pure leptonic channels using the good lepton identification of the NOMAD detector are studied followed by the semi-leptonic channel. Predictions of the expected numbers of events for null hypotheses are given and compared to the found numbers of events inside the "box".

6.1 Event preselection

The available very large statistic of FCAL neutrino interactions collected makes it necessary to preselect events with a topology of a neutral heavy lepton as well as of background measurement events. That is a neutrino neutral or charged current interaction in the FCAL accompanied by an activity in the NOMAD drift chamber volume.

To select FCAL interactions the selection and classification criteria of Section 4.2 are used:

- **Trigger condition**
  one of the two FCAL triggers is required to have fired:

$$FCAL \equiv (\overline{V}_8 \times \mathrm{FCAL}) \tag{6.1}$$

$$FCAL' \equiv (\overline{V}_8 \times \mathrm{FCAL}' \times T_1 \times T_2) \tag{6.2}$$

- **FCAL fiducial volume**
  the reconstructed primary vertex must be in the volume

$$|x| < 90.0 \text{ cm}, \;\; |y| < 90.0 \text{ cm} \;\text{ and }\; -240.15 \text{ cm} < z < -116.15 \text{ cm} \quad (6.3)$$

- **Interaction type classification**
  events are classified as

$$\text{muon neutrino charged current} \qquad \nu_\mu^{CC} \qquad (6.4)$$
$$\text{muon anti neutrino charged current} \qquad \overline{\nu}_\mu^{CC} \qquad (6.5)$$
$$\text{neutrino neutral current} \qquad \nu^{NC} \qquad (6.6)$$
$$\text{cosmic ray} \qquad \text{cosmic} \qquad (6.7)$$

MonteCarlo events are preselected having been generated in the FCAL fiducial volume. Further, events tagged as with problems during data taking (online errors), reconstruction (offline errors) or at generation level (MC truncated) are excluded from analyses.

Events are further required to have at least one drift chamber vertex passing the following criteria:

- **Parent track** (Par)
  To not select vertices produced in charged particle interactions and decays, no incoming charged track producing the vertex ("parent") is requested to be present. Neutral tracks are of course not reconstructed in a detector such as the drift chambers.

- **Daughter tracks** (Dau)
  The vertex must be formed with at least 2 tracks required to fulfill some basic quality criteria. The outgoing tracks ("daughters") are labelled as "good" if:

  - forward pointing $p_z > 0$
  - charge $q \neq 0$
  - length ≥ 10 cm
  - number of hits (used for the track fit) ≥ 7

- **Drift chamber fiducial volume**

$$|x| \leq 130 \text{ cm}, -125 \text{ cm} \leq y \leq 135 \text{ cm} \;\text{ and }\; z_{\min} \leq z \leq 405 \text{ cm} \quad (6.8)$$

$$\text{where } \; z_{\min} = \begin{cases} 20 \text{ cm} & \text{for } MC \\ 20 \text{ cm} & \text{for 96} \\ 50 \text{ cm} & \text{for 97 and 98} \end{cases} \quad (6.9)$$

The fiducial cut is asymmetric in y because the sensitive area of the drift chambers is not centered in y and different in $z_{\min}$ because at the beginning of the 1997 data taking period the first three drift chambers of module 1 were removed to insert an additional subdetector.

- **Muon** (μ@vtx)
  A positive or negative muon must be attached to the vertex, The algorithm used to identify muons (*loose muon id*) consists of the matching of the drift chamber information with that of the muon chambers: the drift chamber track can be extrapolated forward to at least one of the muon chamber stations within a transverse distance of 40 cm to a track in station 1 or 50 cm in station 2. Particles outside the geometrical acceptance of the muon chambers, or ranging out in the detector material can fail this criterion. A minimum track momentum cut (at its first hit in the drift chambers) of 2.5 GeV/c is applied to reduce background from π/K decays and hadron "punchthrough" from particles created either in the FCAL or in coil interactions.

Tables 6.1, 6.2 and 6.3 show the event reduction obtained by applying these criteria to the data and *MonteCarlo* samples. Also listed are the relative cut efficiencies ε_{rel} (*w.r.t.* to its predecessor) and the absolute efficiencies ε_{tot} (*w.r.t.* the total number of events, see Section 4.3.3). The events are further classified at two different cut levels, after the drift chamber fiducial cuts and after the requirement of a muon attached to the vertex.

The large difference of selected events with a muon at the drift chamber "secondary" vertex in the event samples indicates a problem due to the version of reconstruction program used: data from 1996 and the *MonteCarlo* samples were processed with an older version than data from 1997 and 1998. A closer look on the selected events together with the also evident difference between the selected number of charged and neutral current events manifests the problem as misreconstructed FCAL primary muons. Two different cases could be identified:

- **Broken tracks**: the muon track entering the drift chambers is broken into two disconnected track segments e.g. due to a misalignment between two drift chambers used by the reconstruction program. The two track segments may be used to form a common vertex where at least one of the tracks is identified as a muon mimicking a vertex to be selected.

- **Interactions**: the muon is interacting with the drift chamber material e.g. knocking off an electron of the atomic shell (producing a δ-ray electron). Again the two muon track segments do not compose a continous track, whereas the electron together with the outgoing track, identified as a muon, form a vertex passing the selection criteria.

	96_ν			97_ν		
Cut	#	ε_{rel} [%]	ε_{tot} [%]	#	ε_{rel} [%]	ε_{tot} [%]
total	9.682.872	100.00	100.00	9.742.543	100.00	100.00
Vtx	6.352.630	65.61	65.61	6.729.270	69.07	69.07
Par & Dau	1.495.441	23.54	15.44	1.675.025	24.89	17.19
DC_X	1.492.883	99.83	15.42	1.671.983	99.82	17.16
DC_Y	1.488.956	99.74	15.38	1.667.777	99.75	17.12
$DC_{Z\text{min}}$	241.378	16.21	2.49	244.446	14.66	2.51
$DC_{Z\text{max}}$	236.521	97.99	2.44	237.182	97.03	2.43
ν_μ^{CC}	108.426	45.84	1.12	125.203	52.79	1.29
$\overline{\nu}_\mu^{CC}$	2.040	0.86	0.02	2.518	1.06	0.03
ν^{NC}	125.272	52.97	1.29	109.461	46.15	1.12
cosmic	783	0.33	0.01	0	0	0
μ@vtx	20.535	8.68	0.21	4.162	1.75	0.04
ν_μ^{CC}	298	1.45	0.0031	240	5.27	0.0025
$\overline{\nu}_\mu^{CC}$	41	0.20	0.0004	12	0.29	0.0021
ν^{NC}	20.101	97.89	0.2076	3.910	93.95	0.0401
cosmic	95	0.46	0.0010	0	0	0

Table 6.1: *Event selection for data events 1996 and 1997.*

	98_ν			$98_{\overline{\nu}}$		
Cut	#	ε_{rel} [%]	ε_{tot} [%]	#	ε_{rel} [%]	ε_{tot} [%]
total	7.152.686	100.00	100.00	1.066.230	100.00	100.00
Vtx	5.121.813	71.61	71.61	687.426	64.47	64.47
Par & Dau	1.296.230	25.31	18.12	136.279	19.82	12.78
DC_X	1.294.004	99.83	18.09	135.994	99.79	12.75
DC_Y	1.291.463	99.80	18.06	135.761	99.83	12.73
$DC_{Z\text{min}}$	186.453	14.44	2.61	19.180	14.13	1.80
$DC_{Z\text{max}}$	180.739	96.94	2.53	18.632	97.14	1.75
ν_μ^{CC}	95.619	52.90	1.34	4.974	26.70	0.47
$\overline{\nu}_\mu^{CC}$	1.995	1.10	0.03	5.255	28.20	0.49
ν^{NC}	83.125	45.99	1.16	8.403	45.10	0.79
cosmic	0	0	0	0	0	0
μ@vtx	3.155	1.75	0.04	416	0.02	0.04
ν_μ^{CC}	174	5.52	0.0024	8	1.92	0.0008
$\overline{\nu}_\mu^{CC}$	3	0.10	0.0004	13	3.13	0.0012
ν^{NC}	2.978	94.39	0.0416	395	94.95	0.0370
cosmic	0	0	0	0	0	0

Table 6.2: *Event selection for data events 1998 (ν and $\overline{\nu}$ periods).*

	ν_μ^{CC}			ν_μ^{NC}		
Cut	#	ε_{rel} [%]	ε_{tot} [%]	#	ε_{rel} [%]	ε_{tot} [%]
total	448.158	100.00	100.00	166.809	100.00	100.00
Vtx	416.662	92.97	92.97	67.190	40.28	40.28
Par & Dau	141.547	33.97	31.58	32.126	47.81	19.26
DC_X	141.499	99.97	31.58	32.080	99.86	19.23
DC_Y	141.474	99.98	31.57	32.066	99.96	19.22
$DC_{Z\text{min}}$	19.179	13.56	4.28	7.455	23.25	4.47
$DC_{Z\text{max}}$	18.746	97.74	4.18	7.270	97.52	4.36
ν_μ^{CC}	12.888	68.75	2.72	13	0.18	0.008
$\overline{\nu}_\mu^{CC}$	473	2.52	0.11	11	0.15	0.007
ν^{NC}	5.362	28.60	1.20	7.246	99.67	4.34
cosmic	23	0.12	0.01	0	0	0
μ@vtx	1.126	6.01	0.25	6	0.08	0.004
ν_μ^{CC}	29	2.58	$6.47 \cdot 10^{-3}$	0	0	0
$\overline{\nu}_\mu^{CC}$	18	1.60	$4.02 \cdot 10^{-3}$	0	0	0
ν^{NC}	1.077	95.65	$2.40 \cdot 10^{-1}$	6	100.00	$3.60 \cdot 10^{-3}$
cosmic	2	0.18	$4.46 \cdot 10^{-4}$	0	0	0

Table 6.3: *Event selection for MonteCarlo ν_μ^{CC} and ν_μ^{NC} events.*

For both cases also muons tracks could be identified where the incoming track segment is fitted to the vertex, but as backward going track i.e. with reversed momentum. These misreconstructed primary muons appear in all used event samples but with different occurrence depending on the reconstruction version used.

Due to the unidentified primary lepton the event is classified as a neutral current interaction in the FCAL and the formed vertex mimics a neutral heavy particle decay vertex.

Therefore a set of cuts has been established to reject this kind of "artificial" background events, described below.

Rejection of events with misidentified primary muon

For both types of misreconstructed primary muons (see previous section) the track entering the drift chambers is not fitted as a through-going single track but as two track segments. Near the point where the track is broken, the two segments point in the same or opposite direction. In addition the δ-ray electron may be present, with also parallel momentum. A set of cuts is described below to handle all the different possible errors in the reconstruction, rejecting this kind of vertices otherwise passing the selection criteria of neutral heavy lepton decays with a muon at its decay vertex. At the same time these cuts assure some basic criteria of proper decay vertices while retaining the selection efficiency.

- The maximum of the transverse momentum of any vertex track *w.r.t.* the vertex momentum $p^v_{T,\max}$ (build from the sum of all vertex tracks) is small for parallel tracks. A cut on

$$p^v_{T,\max} \geq 30 \text{ MeV}/c \tag{6.10}$$

  standard in NOMAD analyses [120], is used. This also cuts out electrons from photon conversions $\gamma \rightarrow e^+e^-$.

- To select clean decay vertices there should be no activity around the vertex:
  - the transverse distance of any track starting and ending upstream of the vertex extrapolated to the z-position of the vertex should be: Approach ≥ 2.5 cm
  - tracks passing by are required to have a minimal transverse distance of: $\text{Approach}_{\text{Prox}} \geq 10$ cm
  - any track end vertex should be separated at least: $\text{Close}_{\text{End}} \geq 30$ cm
  - any track beginning vertex must be outside: $\text{Close}_{\text{Beg}} \geq 20$ cm
  - and the distance of any hit belonging to a track not attached to the vertex is required to be: $\text{Close}_{\text{Hit}} \geq 15$ cm

- Angles between tracks:
  - The minimum angle between any two tracks of the vertex must be $(1 + \cos\theta^v_{min}) \geq 0.02$
  - The angle between any upstream track (beginning and ending upstream of the vertex) pointing to the vertex (i.e. extrapolated within 10 cm transverse distance at the z-position of the vertex) and any track of the vertex should be $(1 \pm \cos\theta^{up}_{min}) \geq 0.02$

- Basic quality of the vertex: the χ^2 of the vertex fit is required to be $\chi^2_{\text{Vtx}} \leq 50$

- Veto and tube hits:
  - The number of hits in the veto drift chamber (most upstream chamber) 2.5 cm around the point at which a backward extrapolation of the track intersects it:

$$N_{\text{DcVeto}} \begin{cases} \leq 1 & \text{for } N^{\text{v}}_{\text{Trk}} = 2 \\ \leq 3 & \text{for } N^{\text{v}}_{\text{Trk}} = 3 \\ - & \text{for } N^{\text{v}}_{\text{Trk}} > 3 \end{cases} \tag{6.11}$$

  - number of hits collected in a tube backwards 3 cm wide and 50 cm long from the start of the track:

$$N_{\text{Tube}} \begin{cases} \leq 10 & \text{for } N^{\text{v}}_{\text{Trk}} = 2 \\ - & \text{for } N^{\text{v}}_{\text{Trk}} > 2 \end{cases} \tag{6.12}$$

- No track of the vertex should end at a position upstream of the fiducial volume.

The breakdown in the event selection for the data taking periods and for the simulated events is shown in Tables 6.4, 6.5 and 6.6. The effects of the single cuts can be compared in the different samples by the quoted relative breakdown *w.r.t.* its predecessor, ε_{rel}. Also listed are the ratios of the remaining events and the total numbers of events (see Section 6.1). As can be expected, the 1996 and *MonteCarlo* samples show similar behavior and 1997 can be compared with 1998 because of the reconstruction program versions applied.

	96_ν			97_ν		
Cut	#	ε_{rel} [%]	ε_{tot} [%]	#	ε_{rel} [%]	ε_{tot} [%]
μ@vtx	20.535	100.00	$2.12 \cdot 10^{-1}$	4.162	100.00	$4.27 \cdot 10^{-2}$
$p^v_{T,\text{max}}$	7.754	37.76	$8.01 \cdot 10^{-2}$	2.508	60.26	$2.57 \cdot 10^{-2}$
Approach	4.426	57.08	$4.57 \cdot 10^{-2}$	2.144	85.49	$2.20 \cdot 10^{-2}$
$\text{Close}_{\text{Beg}}$	3.956	89.38	$4.09 \cdot 10^{-2}$	1.950	90.95	$2.00 \cdot 10^{-2}$
$\text{Close}_{\text{Hit}}$	3.641	92.04	$3.76 \cdot 10^{-2}$	1.899	97.38	$1.95 \cdot 10^{-2}$
$\text{Close}_{\text{End}}$	3.295	90.50	$3.40 \cdot 10^{-2}$	892	46.97	$9.16 \cdot 10^{-3}$
$\text{Approach}_{\text{Prox}}$	3.004	91.17	$3.10 \cdot 10^{-2}$	828	92.83	$8.50 \cdot 10^{-3}$
$\cos\theta^{up}_{min}$	2.994	99.67	$3.09 \cdot 10^{-2}$	806	97.34	$8.27 \cdot 10^{-3}$
$\cos\theta^{v}_{min}$	2.966	99.06	$3.06 \cdot 10^{-2}$	601	74.57	$6.17 \cdot 10^{-3}$
χ^2_{Vtx}	2.593	87.42	$2.68 \cdot 10^{-2}$	562	93.51	$5.77 \cdot 10^{-3}$
N_{DcVeto}	207	7.98	$2.14 \cdot 10^{-3}$	257	45.73	$2.64 \cdot 10^{-3}$
N_{Tube}	197	95.17	$2.03 \cdot 10^{-3}$	243	94.55	$2.49 \cdot 10^{-3}$
$\text{Track}_{\text{ZMin}}$	170	86.29	$1.76 \cdot 10^{-3}$	201	82.72	$2.06 \cdot 10^{-3}$
ν_μ^{CC}	50	29.41	$5.16 \cdot 10^{-4}$	63	31.34	$6.47 \cdot 10^{-4}$
$\overline{\nu}_\mu^{CC}$	0	0	0	2	1.00	$2.05 \cdot 10^{-5}$
ν^{NC}	120	70.59	$1.24 \cdot 10^{-3}$	136	67.66	$1.40 \cdot 10^{-3}$
cosmic	0	0	0	0	0	0

Table 6.4: *Event selection for data events 1996 and 1997.*

Because the ratios of the different event types in the three data taking periods are similar after passing the selection cuts, e.g. the ratios of neutral current to charged current events and the number of remaining events in the different samples *w.r.t.* delivered protons on target (see Section 4.3.6), the events are merged to one sample used for the further analysis, listed in Table 6.7. The antineutrino sample $98_{\overline{\nu}}$ is not included, since the neutral heavy leptons are assumed to be produced only in neutrino interactions and, however, its remaining statistic is small.

The factor of 2 between the final data sample neutral and charge current events indicates a bias in the selection of neutral heavy lepton type events (cf. Section 6.7).

	98_{ν}			$98_{\overline{\nu}}$		
Cut	#	ε_{rel} [%]	ε_{tot} [%]	#	ε_{rel} [%]	ε_{tot} [%]
μ@vtx	3.155	100.00	$4.41 \cdot 10^{-2}$	416	100.00	$3.90 \cdot 10^{-2}$
$p^{v}_{T,\text{max}}$	1.875	59.43	$2.62 \cdot 10^{-2}$	237	56.97	$2.22 \cdot 10^{-2}$
Approach	1.611	85.92	$2.25 \cdot 10^{-2}$	209	88.19	$1.96 \cdot 10^{-2}$
$\text{Close}_{\text{Beg}}$	1.488	92.36	$2.08 \cdot 10^{-2}$	193	92.34	$1.81 \cdot 10^{-2}$
$\text{Close}_{\text{Hit}}$	1.452	97.58	$2.03 \cdot 10^{-2}$	187	96.89	$1.75 \cdot 10^{-2}$
$\text{Close}_{\text{End}}$	674	46.42	$9.42 \cdot 10^{-3}$	87	46.52	$8.16 \cdot 10^{-3}$
$\text{Approach}_{\text{Prox}}$	620	91.99	$8.67 \cdot 10^{-3}$	82	94.25	$7.69 \cdot 10^{-3}$
$\cos\theta^{up}_{min}$	612	98.71	$8.56 \cdot 10^{-3}$	81	98.78	$7.60 \cdot 10^{-3}$
$\cos\theta^{v}_{min}$	452	73.86	$6.32 \cdot 10^{-3}$	50	61.73	$4.69 \cdot 10^{-3}$
χ^2_{Vtx}	428	94.69	$5.98 \cdot 10^{-3}$	46	92.00	$4.31 \cdot 10^{-3}$
N_{DcVeto}	166	38.79	$2.32 \cdot 10^{-3}$	18	39.13	$1.69 \cdot 10^{-3}$
N_{Tube}	159	95.78	$2.22 \cdot 10^{-3}$	16	88.89	$1.50 \cdot 10^{-3}$
$\text{Track}_{\text{ZMin}}$	127	79.87	$1.76 \cdot 10^{-3}$	11	68.75	$1.03 \cdot 10^{-3}$
ν^{CC}_{μ}	43	33.86	$6.01 \cdot 10^{-4}$	2	18.18	$1.86 \cdot 10^{-4}$
$\overline{\nu}^{CC}_{\mu}$	0	0	0	1	0.09	$9.38 \cdot 10^{-5}$
ν^{NC}	84	66.14	$1.17 \cdot 10^{-3}$	8	72.73	$7.50 \cdot 10^{-4}$
cosmic	0	0	0	0	0	0

Table 6.5: *Event selection data events 1998 (ν and $\overline{\nu}$ periods).*

	ν^{CC}_{μ}			ν^{NC}_{μ}		
Cut	#	ε_{rel} [%]	ε_{tot} [%]	#	ε_{rel} [%]	ε_{tot} [%]
μ@vtx	1.126	100.00	$0.25 \cdot 10^{-1}$	6	100.00	$3.60 \cdot 10^{-3}$
$p^{v}_{T,\text{max}}$	357	31.71	$7.97 \cdot 10^{-2}$	6	100.00	$3.60 \cdot 10^{-3}$
Approach	186	52.10	$4.15 \cdot 10^{-2}$	2	33.33	$1.20 \cdot 10^{-3}$
$\text{Close}_{\text{Beg}}$	167	89.78	$3.73 \cdot 10^{-2}$	2	100.00	$1.20 \cdot 10^{-3}$
$\text{Close}_{\text{Hit}}$	154	92.22	$3.44 \cdot 10^{-2}$	2	100.00	$1.20 \cdot 10^{-3}$
$\text{Close}_{\text{End}}$	145	94.16	$3.24 \cdot 10^{-2}$	2	100.00	$1.20 \cdot 10^{-3}$
$\text{Approach}_{\text{Prox}}$	128	88.28	$2.86 \cdot 10^{-2}$	1	50.00	$5.99 \cdot 10^{-4}$
$\cos\theta^{up}_{min}$	128	100.00	$2.86 \cdot 10^{-2}$	1	100.00	$5.99 \cdot 10^{-4}$
$\cos\theta^{v}_{min}$	126	98.44	$2.81 \cdot 10^{-2}$	1	100.00	$5.99 \cdot 10^{-4}$
χ^2_{Vtx}	123	97.62	$2.74 \cdot 10^{-2}$	1	100.00	$5.99 \cdot 10^{-4}$
N_{DcVeto}	10	8.13	$2.23 \cdot 10^{-3}$	1	100.00	$5.99 \cdot 10^{-4}$
N_{Tube}	10	100.00	$2.23 \cdot 10^{-3}$	1	100.00	$5.99 \cdot 10^{-4}$
$\text{Track}_{\text{ZMin}}$	9	90.00	$2.01 \cdot 10^{-3}$	1	100.00	$5.99 \cdot 10^{-4}$
ν^{CC}_{μ}	6	66.67	$1.34 \cdot 10^{-3}$	0	0	0
$\overline{\nu}^{CC}_{\mu}$	0	0	0	0	0	0
ν^{NC}	3	33.33	$6.69 \cdot 10^{-4}$	1	100.00	$5.99 \cdot 10^{-4}$
cosmic	0	0	0	0	0	0

Table 6.6: *Event selection for MonteCarlo ν^{CC}_{μ} and ν^{NC}_{μ} events.*

	96_ν	97_ν	98_ν	$\sum_\nu$
Type	#	#	#	#
all	170	201	127	498
ν_μ^{CC}	50	63	43	156
$\overline{\nu}_\mu^{CC}$	0	2	0	2
ν^{NC}	120	136	84	340
cosmic	0	0	0	0

Table 6.7: *Final data samples.*

The remaining simulated ν_μ^{NC} and ν_μ^{CC} events passing the selection cuts consist of neutral hadron punchthrough. Investigating the simulated particle information, they can be identified as one neutron, one pion and dominantly K_L^0 and K_S^0 interacting or decaying in the drift chambers. One of the produced particles is identified as a muon, misidentified or because a produced pion decays into a muon and neutrino where the reconstruction can not distinguish between the pion and the muon.

Because the available remaining *MonteCarlo* statistic is too low for further comparisons to data events subsets of the data itself, where no neutral heavy lepton signal can be expected, will be used instead to further study and reduce the remaining background events, as outlined in the following section.

6.2 Blind analysis

An analysis like the search for neutral heavy particles or neutrino oscillations is looking for a small number of signal events in a huge number of "standard" physics events, partially acting as background for the search. An analysis method avoiding biases from the researchers prejudice on the existence or not of a signal is the so-called "blind analysis" method. This implies not looking at the relevant event topologies or distributions of certain variables for real data, characteristic for the signal when setting up the analysis strategy. In this way, the selection criteria are based purely on the modeled *MonteCarlo* and/or the rejection of known background. The region where the signal is expected to be found is called the "box", whereas everything outside acts as a "control sample". Once the box is defined the sensitivity of the analysis can be calculated. After demonstrating good control over the background the box may be opened and by definition, the result has to be accepted unless a clear error is evident, showing that there was no control over the background.

In the search for a neutral heavy particle the control samples might be chosen as:

- **Neutrino charged current events**:
  Neutral heavy leptons are assumed to be produced via mixing with standard neutrinos, i.e. the neutrino of the neutral current interaction in the FCAL and not in FCAL charged current events.

- **Like-sign decay vertices**:
  The decay products of the neutral heavy lepton should form a neutral vertex, i.e. in the drift chambers.

- **Out-of-time events**:
  The decay of the neutral heavy particle should be temporally correlated with the drift chamber vertex.

The analysis strategy is to get control over these background types: to calculate or if possible eliminate them. Depending on the results of the control sample studies one may decide to chose further criteria or to "open the box". The used control samples may also vary depending on the decay channel. For the further analyses of the three different decay modes FCAL neutrino charged current events are used as the main control sample.

According to Section 4.3.3 the measured number of neutral and charged current interactions is in the same order of magnitude. Thus, using the ν_μ^{CC} final sample as a control sample to predict the number of signal plus background ν^{NC} events does not allow to scale down the statistical uncertainty. For the prediction of neutral from charged current events an unbiased (see Page 106) factor of 1 is used, discussed with the systematic uncertainties (Section 6.7).

6.3 $\mathcal{N}_\mu \to \mu^-\mu^+\nu_\mu$ event selection

The signature consists of a two track vertex where both tracks are identified as muons. Using the excellent muon identification capabilities of the detector and the fact that no standard physics process is able to produce such a signature, no background is expected.

Table 6.8 shows the remaining events passing the selection criteria in the final charged current event sample acting as a control sample. The identification of the additional second muon is the same loose muon identification as used for the first one (see Page 102).

No event passed these cuts. No requirements are imposed on the total vertex charge ($\mu^+\mu^-$) and the correlation in time between the drift chamber vertex and the FCAL vertex ($\Delta t^{\mathrm{c}}_{\mathrm{Vtx}}$). Assuming that the control sample ν_μ^{CC} events are not different from ν^{NC} events, the predicted number of events in the neutral current

sample	ν_μ^{CC}
all	156
2 Tracks	73
$+\mu$	0

Table 6.8: *Selection of* $\mathcal{N}_\mu \to \mu^-\mu^+\nu_\mu$ *events.*

final sample is:

$$\boxed{N_{\mu\mu} = 0^{+1}_{-0}} \tag{6.13}$$

To calculate the (signal) efficiency the same cuts were applied to the generated neutral heavy leptons for this decay mode (see Chapter 5). Figure 6.1 (cf. Tables A.1 and A.2) shows the relative efficiencies of the two muon IDs and the total selection efficiency. The NOMAD single muon identification efficiency is approximately 80%; because of the presence of two muons, the efficiency of the first muon ID requirement is about $(0.80 \times (1-0.80) \cdot 0.80 \simeq 95\%)$. The total efficiency is $\simeq 40\%$ for NHL masses $\gtrsim 2$ GeV/c^2.

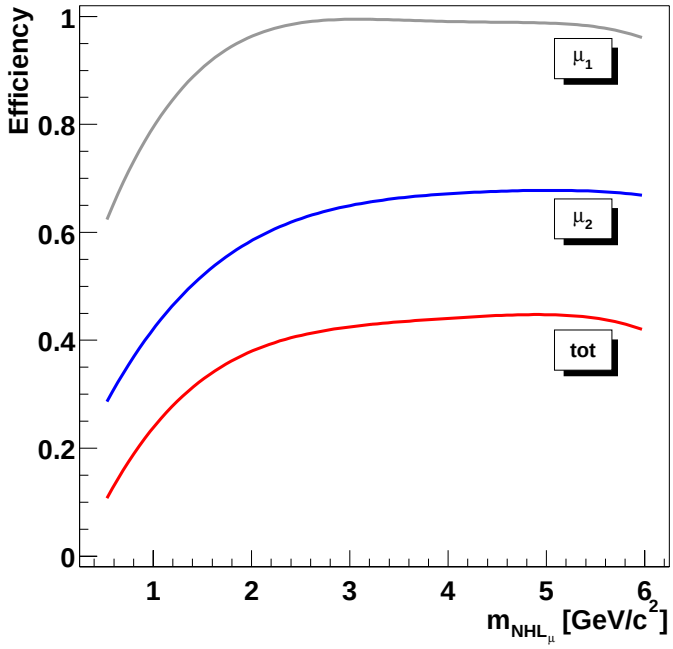

Figure 6.1: *Selection efficiency vs. mass for* $\mathcal{N}_\mu \to \mu^-\mu^+\nu_\mu$.

6.4 $\mathcal{N}_\mu \to \mu^- e^+ \nu_e$ event selection

In the GLR [11] model used in this analysis a muon type neutral heavy lepton may decay into a negative muon and a positron plus a neutrino. In order to keep the search as model independent as possible, no requirements on the charge of the two leptons is made.

Similar to the NHL decay mode with two muons in the final state the event selection for $\mathcal{N}_\mu \to \mu^- e^+ \nu_e$ consists of vertices with two tracks, where one is identified as a muon and one as an electron (or positron).

The search for the electronic decay mode of the neutral heavy particle requires detection capability for electrons. The identification method employed is described below.

Electron identification

The information of several NOMAD subdetectors may be used and combined to identify electrons. The interplay of the TRD, the PRS and the ECAL (see Chapter 2) provides a good rejection factor against charged hadrons, while retaining a reasonable electron identification efficiency. In this analysis the informations from the transition radiation detector and the electromagnetic calorimeter are used.

Using the transition radiation detector:
The NOMAD transition radiation detector is designed to separate electrons from heavier charged particles, mainly pions. Electron recognition in the TRD is based on a likelihood function calculated from the energy deposited in the nine detection planes and from the incident track momentum. Energy depositions are compared to the expectations for two possible hypotheses: electron and pion. The momentum of the particle measured in the drift chambers is taken into account to evaluate the expected energy deposition.

Depending on the topology of the event, isolated and non-isolated particles in the TRD, two different procedures are applied. A detailed description of the procedures can be found in References [121] and [122]. Here only the algorithm for isolated tracks is outlined since this is the main signature of neutral heavy lepton decays.

The likelihood ratio $\mathcal{L}$ is computed from the responses of all the detection planes crossed by an incident track:

$$\mathcal{L} = \sum_{i=1}^{N} \log \frac{P(\epsilon_i|e;p)}{P(\epsilon_i|\pi;p)} \tag{6.14}$$

where N is the number of hits assigned to a track. $P(\epsilon_i|e;p)$ and $P(\epsilon_i|\pi;p)$ are the probability density functions for an electron e and a pion π with

a given momentum p to deposit the energy ϵ_i in the ith detection plane hit. The distributions of probability density that a given energy deposition, generated either by an electron or a pion, have been obtained from detailed simulation, extensive test beam, and *in situ* measurements (for details see Reference [123]). The desired electron efficiency defines a threshold on the total likelihood ratio, see Figure 6.2. An electron (pion) is associated with a likelihood ratio above (below) this threshold. A pion rejection factor better than 1000 at 90% electron efficiency has been achieved for isolated particles crossing all nine TRD modules in a momentum range from 1 to 50 GeV/c.

Using the electromagnetic calorimeter:
In the ECAL electron identification is based on the shape of the shower profile. In addition, the momentum p_{fin} measured in the drift chambers must be compatible with the energy E_{cal} deposited in the electromagnetic calorimeter. In contrast, most of the charged hadrons reaching the ECAL deposit only a fraction of their energy. The average value of $(E_{\text{cal}} - p_{\text{fin}})/(E_{\text{cal}} + p_{\text{fin}})$ (see Figure 6.3) is slightly shifted to positive values because the momentum p_{fin} is measured at the end of the track. Thus, electrons may loose some energy due to dE/dx and bremsstrahlung, which is however measured in the ECAL cluster assigned to the electron track.

Since the event topology for the electronic decay of neutral heavy particles is much simpler compared to e.g. electron neutrino charged current interactions a loose electron identification criterion is used, based only on the TRD and ECAL:

- The pion contamination for a track reconstructed in the drift chambers and matched to a TRD track must be less than 1%.

- The momentum measured in the drift chambers must be compatible with the energy deposited in the electromagnetic calorimeter:

$$-0.25 < \frac{E_{\text{cal}} - p_{\text{fin}}}{E_{\text{cal}} + p_{\text{fin}}} < +0.50 \tag{6.15}$$

In Table 6.9 the control sample events passing the selection cuts are listed.

sample	ν_μ^{CC}
all	156
2 Tracks	73
+e	0

Table 6.9: *Selection of* $\mathcal{N}_\mu \to \mu^- e^+ \nu_e$ *events.*

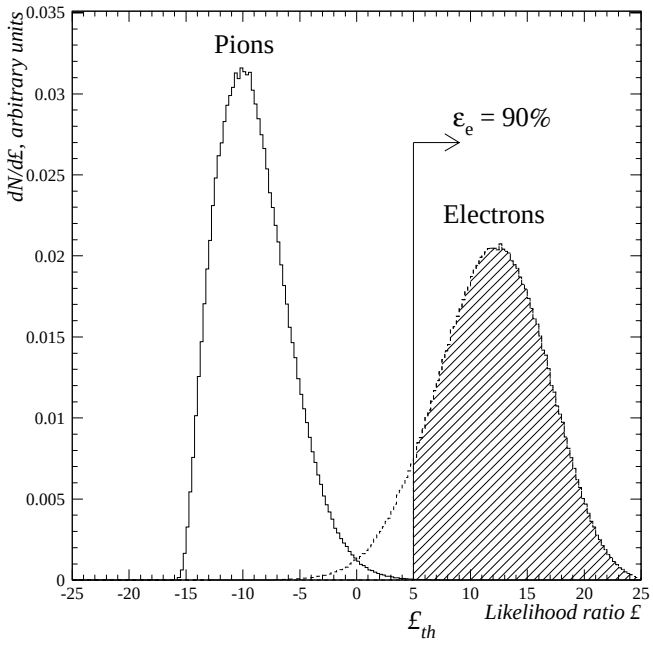

Figure 6.2: *The likelihood ratio distributions for pions and electrons with track momenta* 10 *GeV/c crossing nine TRD modules (MonteCarlo simulation). Pion rejection is better than 1000:1 at 90% electron efficiency.*

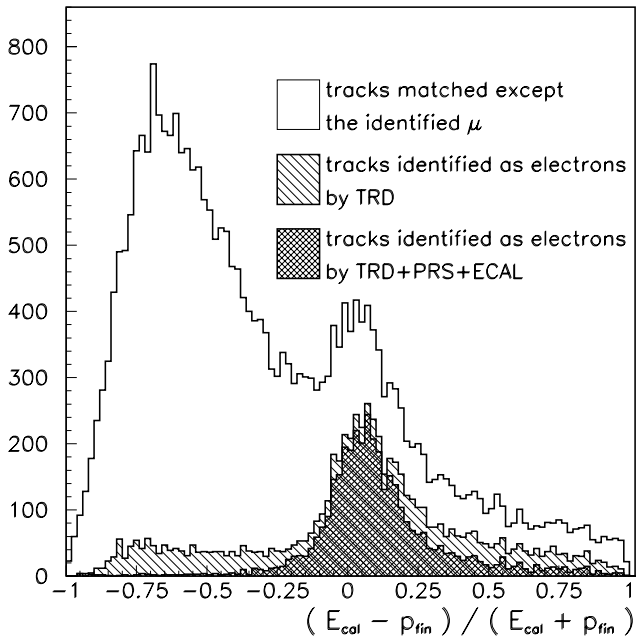

Figure 6.3: *The* $(E_{\text{cal}} - p_{\text{fin}})/(E_{\text{cal}} + p_{\text{fin}})$ *distribution for all tracks (except the muon) in* ν_μ^{CC} *interactions and after successive cuts against hadrons based on the TRD signal and PRS/ECAL consistency.*

Again, no requirements on the total vertex charge and temporal correlation are imposed. No events passed the second lepton cut and the predicted number of events in the neutral current final event sample is:

$$\boxed{N_{\mu e} = 0^{+1}_{-0}} \tag{6.16}$$

The same selection cuts were applied to the generated $\mathcal{N}_\mu \to \mu^- e^+ \nu_e$ events and the relative efficiencies of the lepton ID cuts as well as the total efficiency as a function of the neutral heavy lepton mass is shown in Figure 6.4 (cf. Tables A.3 and A.4). The efficiency for the electron is $\simeq 60\%$. The muon efficiency is $\simeq 85\%$ and the total efficiency is $\simeq 35\%$ for masses $\gtrsim 2$ GeV/c^2.

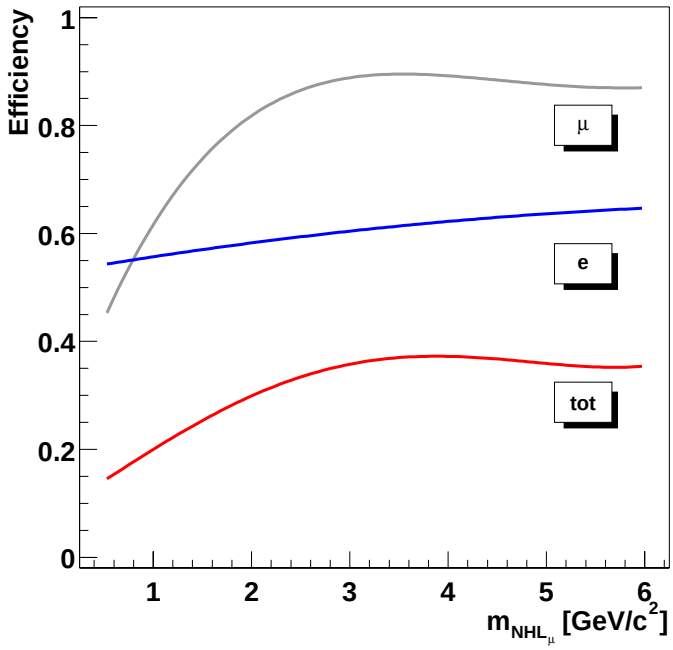

Figure 6.4: *Selection efficiency vs. mass for* $\mathcal{N}_\mu \to \mu^- e^+ \nu_e$.

6.5 $\mathcal{N}_\mu \to \mu^- X$ event selection

The signature of the neutral heavy lepton decay mode $\mathcal{N}_\mu \to \mu^- X$ is a vertex with one identified muon together with a system X, where X stands for any number of tracks not necessarily identified (but reconstructed). This contains also the decay modes $\mathcal{N}_\mu \to \mu^- \mu^+ \nu_\mu$ and $\mathcal{N}_\mu \to \mu^- e^+ \nu_e$.

To further select only well reconstructed vertices additional requirements are imposed on the quality of the tracks forming the vertex, in such a way, that at least 2 tracks fulfill the following criteria:

- **Quality of vertex tracks**
  - the radial distance of the track first hit and the vertex is within:

$$-5 \text{ cm} \leq |\vec{r}_{\text{first hit}} - \vec{r}_{\text{Vtx}}| \leq 15 \text{ cm} \tag{6.17}$$

  - the relative error on the magnitude of momentum $\delta p/p$ is less than 50%. With the error on the magnitude of the 3-momentum:

$$\delta p = \vec{p} \cdot (\sigma_p \cdot \vec{p})/|\vec{p}|^2 \tag{6.18}$$

    for given momentum $\vec{p}$ and covariance matrix σ_p.
  - the χ^2 of the track fit is $\chi^2_{\text{Trk}} \leq 250$

459 out of the 498 final sample events pass these criteria (see N_{good} in Table 6.10). Figure 6.5 shows the longitudinal (z) distribution of the secondary vertices in the drift chambers.

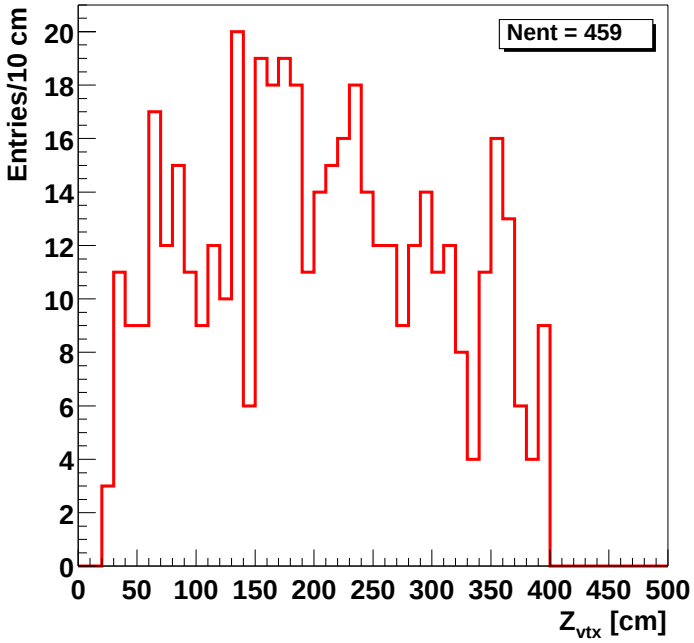

Figure 6.5: *Vertex z distribution of selected $\mathcal{N}_\mu \to \mu^- X$ vertices.*

In order to identify and reject K^0_S and K^0_L punchthrough decaying in the drift chambers contaminating the sample, as indicated by the surviving ν_μ^{CC} and ν^{NC} *MonteCarlo* events (see Page 108), a K^0_S hypothesis is imposed. That is, for any two track vertex, a particle ID of two pions is assumed for which the invariant mass $m_{K^0_S}$ of the vertex, as well as the transverse momentum $p^v_{T,+}$ of one of the tracks (by convention the positive; if both have the same charge, the one with the highest momentum is chosen) to the total vertex momentum (formed by the sum of the two track momenta) is calculated.

$$\begin{aligned} m_{K^0_S} &= \sqrt{E^2_{K^0_S} - \vec{p}^2_{\pi^\pm}} \\ \text{with :} \quad & E_{\pi^\pm} = \sqrt{\vec{p}^2_{\pi^\pm} + m^2_{\pi^\pm}} \\ \text{and} \quad & E_{K^0_S} = E_{\pi^+} + E_{\pi^-} \end{aligned} \tag{6.19}$$

Figure 6.5 shows the so calculated invariant K^0_S mass distribution for the vertices passing the selection cuts and Figure 6.5 for the vertices with $30 < p^v_{T,+} < 230$ MeV/c (see also [120]). The criteria for decaying K^0_L and K^0_S

$$K^0_L \longrightarrow \pi^\pm \mu^\mp \nu \quad \text{called } K^0_{\mu 3} \tag{6.20}$$

$$K^0_S \to \pi^+\pi^- \text{ with one } \pi^\pm \to \mu^\pm \nu \tag{6.21}$$

are chosen as:

$$\begin{array}{rcccl} 300 & \text{MeV}/c^2 & \leq & m_{K^0_S} & \leq \quad 550 \quad \text{MeV}/c^2 \\ 30 & \text{MeV}/c & \leq & p^v_{T,+} & \leq \quad 230 \quad \text{MeV}/c \end{array} \tag{6.22}$$

The cut on the mass is asymmetric around $m_{K^0_S} = 497.8$ MeV/c^2 [1] because of the possible missing momentum carried by the invisible neutrino from the pion decay. The resolution of the K^0_S mass is $\simeq 12$ MeV/c^2 [120].

all	498
N_{good}	459
K^0_S	382
ν_μ^{CC}	114
$\overline{\nu}_\mu^{CC}$	1
ν^{NC}	267

Table 6.10: *Selection of* $\mathcal{N}_\mu \to \mu^- X$ *events.*

77 vertices are identified as K^0_L/K^0_S (see Table 6.10). Lack of large *Monte-Carlo* statistics prevents checking the K^0_S candidates. However, a K^0_S survival

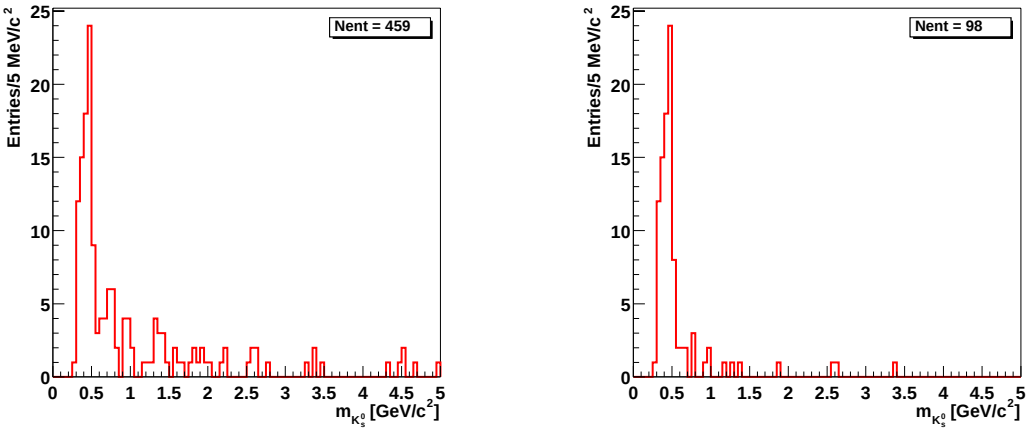

Figure 6.6: K^0_S *hypothesis mass (left) and for* $30 < p^v_{T,+} < 230$ *MeV/c (right).*

probability calculation using 30000 simulated "stretched" K^0_S events yields a number within a factor of 2 of 77. "Stretched" means that K^0_S produced at the primary interaction vertex in the FCAL are translated 250 cm along their momentum direction into the drift chamber volume and forced to decay into a π^+ π^- pair to get a sufficient statistic of such kind of events.

In order to predict the number of in-time neutral current events with total vertex charge zero, the "box", the control sample of charged current events is studied.

Figure 6.7 shows the distribution of flight time corrected time difference between the FCAL primary event vertex and the drift chamber vertex. $\Delta t^c_{\mathrm{Vtx}}$ is calculated in analogy to Section 4.5 where the drift chamber single track time is replaced by the track length weighted times of the vertex tracks and the energy used for the flight time correction is the sum of the vertex tracks $E_{\mathrm{Vtx}} = \sum E_{\mathrm{Trk}}$. Only two track vertices and vertices with more than two tracks with a charge sum of $-1 \leq Q_{\mathrm{Vtx}} \leq +2$ are included. Other vertices are considered as not well reconstructed. The asymmetry reflects the different resulting charge in the final state of *NC* and *CC* interactions. As a cross-check, the $\Delta t^c_{\mathrm{Vtx}}$ distribution of the identified K^0_S can be used (Figure 6.8). The asymmetry of the distribution can be interpreted as the effect of the invisible neutrino: the visible vertex energy used for the flight time correction is smaller than the true value.

The in-time window is chosen as:

$$|\Delta t^c_{\mathrm{Vtx}}| < 10 \text{ ns} \tag{6.23}$$

Table 6.11 lists the in-time charged and neutral current events according to their vertex charge sum (see notes on Figure 6.7 before). The empty columns are the signal "box".

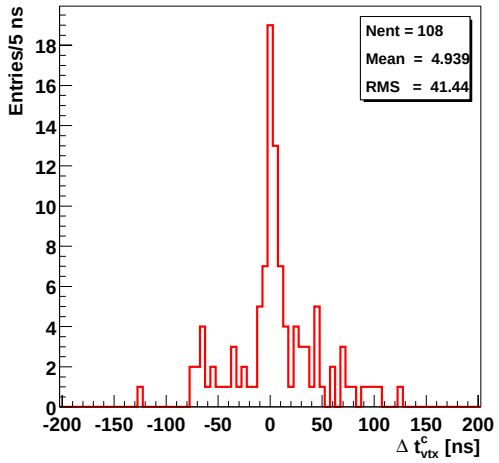

Figure 6.7: Δt^c_{Vtx} *of the* ν_μ^{CC} *control sample.*

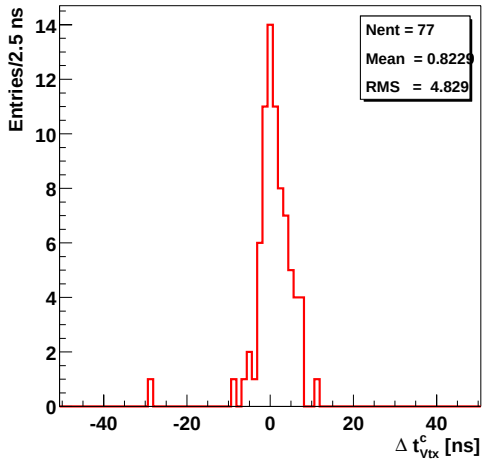

Figure 6.8: Δt^c_{Vtx} *of identified* K^0_S.

sample	ν_μ^{CC}			ν^{NC}		
charge	$\sum$	$Q_{\mathrm{Vtx}} \neq 0$	$Q_{\mathrm{Vtx}} = 0$	$\sum$	$Q_{\mathrm{Vtx}} \neq 0$	$Q_{\mathrm{Vtx}} = 0$
in-time	48	20	28	–	36	–

Table 6.11: *In-time control sample* $\mathcal{N}_\mu \rightarrow \mu^- X$ *events.*

Assuming no principal difference in the remaining in-time events between neutral and charged current events the neutral current in-time events with charge sum zero can be estimated as:

$$N^{\text{in}}_{NC}(Q_{\text{Vtx}} = 0) = \frac{N^{\text{in}}_{NC}(Q_{\text{Vtx}} \neq 0)}{N^{\text{in}}_{CC}(Q_{\text{Vtx}} \neq 0)} \times N^{\text{in}}_{CC}(Q_{\text{Vtx}} = 0) \tag{6.24}$$

$$\boxed{N_{\mu X} = N^{\text{in}}_{NC}(Q_{\text{Vtx}} = 0) = 50 \pm 17} \tag{6.25}$$

where the error estimate is statistical.

Further reduction of control sample background events would require that kinematical cuts using specific properties of the NHL were to be applied. In order to perform a model independent analysis and because of unavoidable background from overlay events which can only be measured, it was decided not to apply further selection criteria.

The same set of cuts applied to $\mathcal{N}_\mu \rightarrow \mu^- X$ *MonteCarlo* events yields the selection efficiency vs. the neutral heavy lepton mass in Figure 6.9 (cf. Tables A.5 and A.6). The relative efficiency of the muon identification dominates the overall efficiency for low masses whereas for masses above $\gtrsim 3$ GeV/c^2 the efficiency is dominated by track and vertex reconstruction inefficiencies.

6.6 Box opening

Having established the neutral heavy lepton selection criteria for the three NHL decay modes on the control samples outside the signal region (neutrino charged current interactions) the results of the neutral heavy lepton search are obtained from the events inside the signal "box".

For the two leptonic channels $\mathcal{N}_\mu \rightarrow \mu^-\mu^+\nu_\mu$ and $\mathcal{N}_\mu \rightarrow \mu^- e^+ \nu_e$ no neutrino neutral current event is found with a two track drift chamber vertex applying the particle ID criteria. Table 6.12 lists the selected $\mathcal{N}_\mu \rightarrow \mu^-\mu^+\nu_\mu$ and $\mathcal{N}_\mu \rightarrow \mu^- e^+ \nu_e$ neutral heavy lepton events passing the cuts. The null result agrees well with the prediction for both channels of (0^{+1}_{-0}) events (Equations 6.13 and 6.16).

In the signal sample for the semi-leptonic decay channel $\mathcal{N}_\mu \rightarrow \mu^- X$, consisting of in-time neutral current interactions with vertices of charge sum zero, 27 $N^{\text{in}}_{NC}(Q_{\text{Vtx}} = 0)$ events were found (see Table 6.13), $\simeq 1.35\ \sigma$ less than the prediction of $N_{\mu X} = (50 \pm 17)$ events (see Equation 6.25) and consistent with a negative result for the search.

Figures 6.10, 6.11 and 6.12 show displays [118] (cf. Page 90) of three signal sample events passing the $\mathcal{N}_\mu \rightarrow \mu^- X$ selection cuts. Figures 6.10 and 6.11 are possible canditates for neutral hadron "punchthrough", while Figure 6.12 is a possible in-time overlay event.

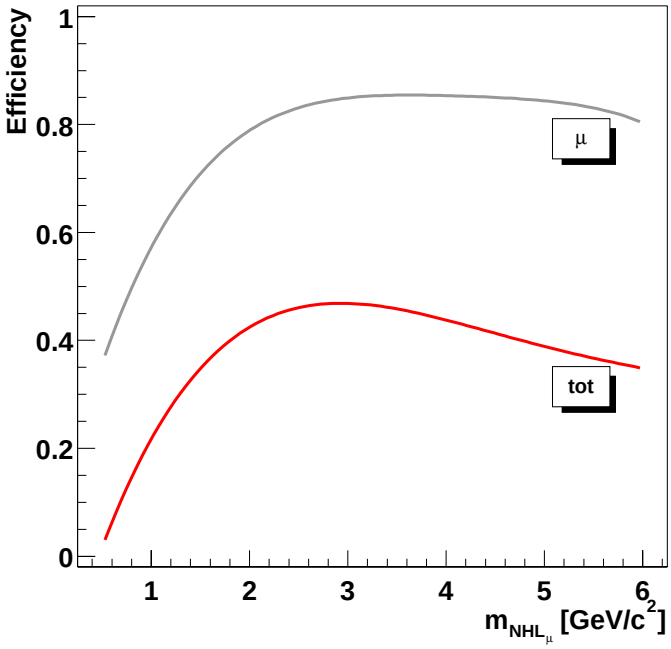

Figure 6.9: *Selection efficiency vs. mass for* $\mathcal{N}_\mu \to \mu^- X$.

sample	ν_μ^{CC}	ν^{NC}
all	156	340
2 Tracks	73	122
$+\mu/$ +e	0 / 0	0 / 0

Table 6.12: $\mathcal{N}_\mu \to \mu^-\mu^+\nu_\mu$ *and* $\mathcal{N}_\mu \to \mu^- e^+ \nu_e$ *event selection in* ν_μ^{CC} *and* ν^{NC} *data samples.*

sample	ν_μ^{CC}			ν^{NC}		
charge	$\sum$	$Q_{\mathrm{Vtx}} \neq 0$	$Q_{\mathrm{Vtx}} = 0$	$\sum$	$Q_{\mathrm{Vtx}} \neq 0$	$Q_{\mathrm{Vtx}} = 0$
in-time	48	20	28	63	36	27

Table 6.13: $\mathcal{N}_\mu \to \mu^- X$ *event selection in* ν_μ^{CC} *and* ν^{NC} *data samples.*

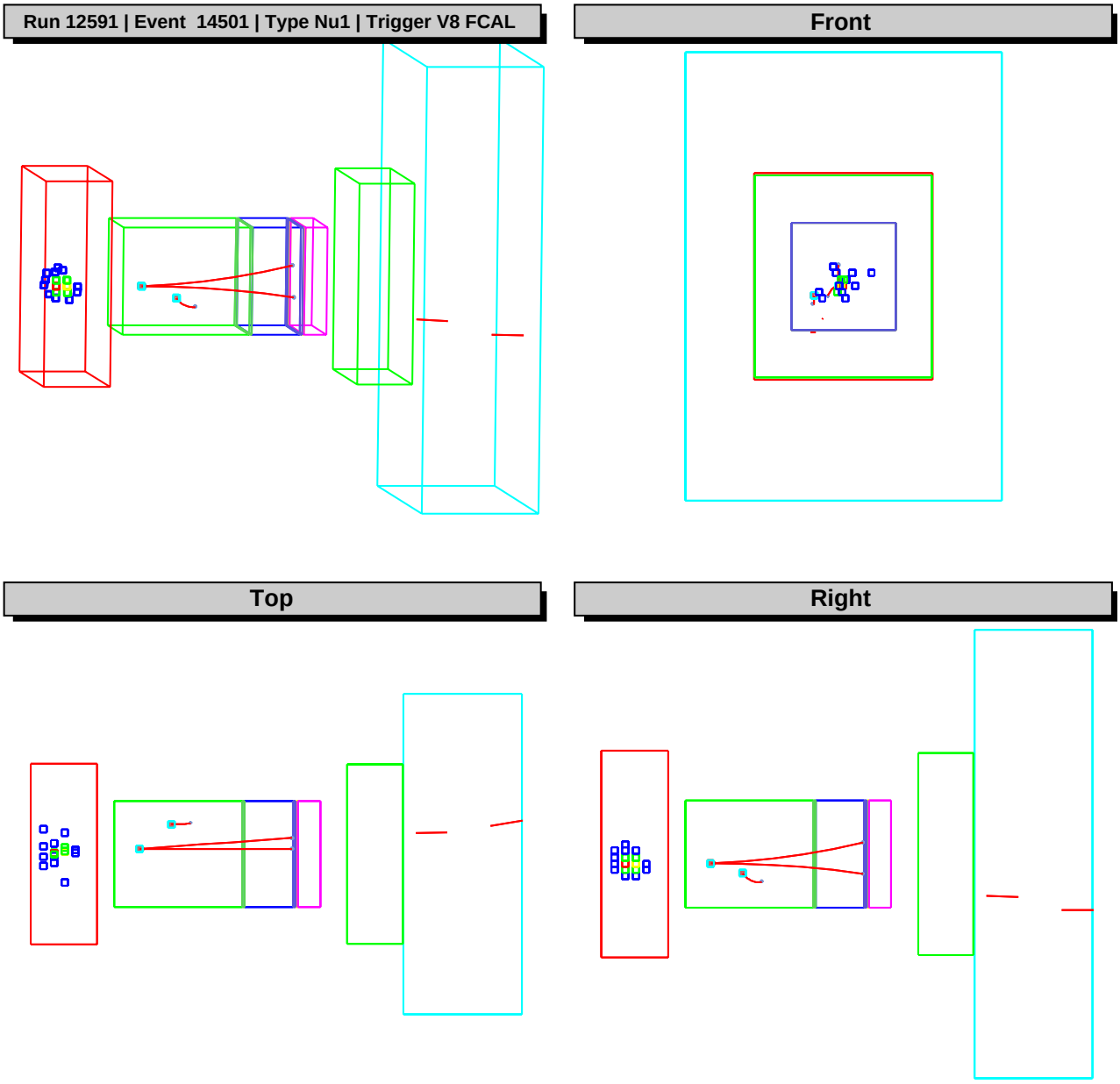

Figure 6.10: *Signal sample* $\mathcal{N}_\mu \to \mu^- X$ *survivor.*

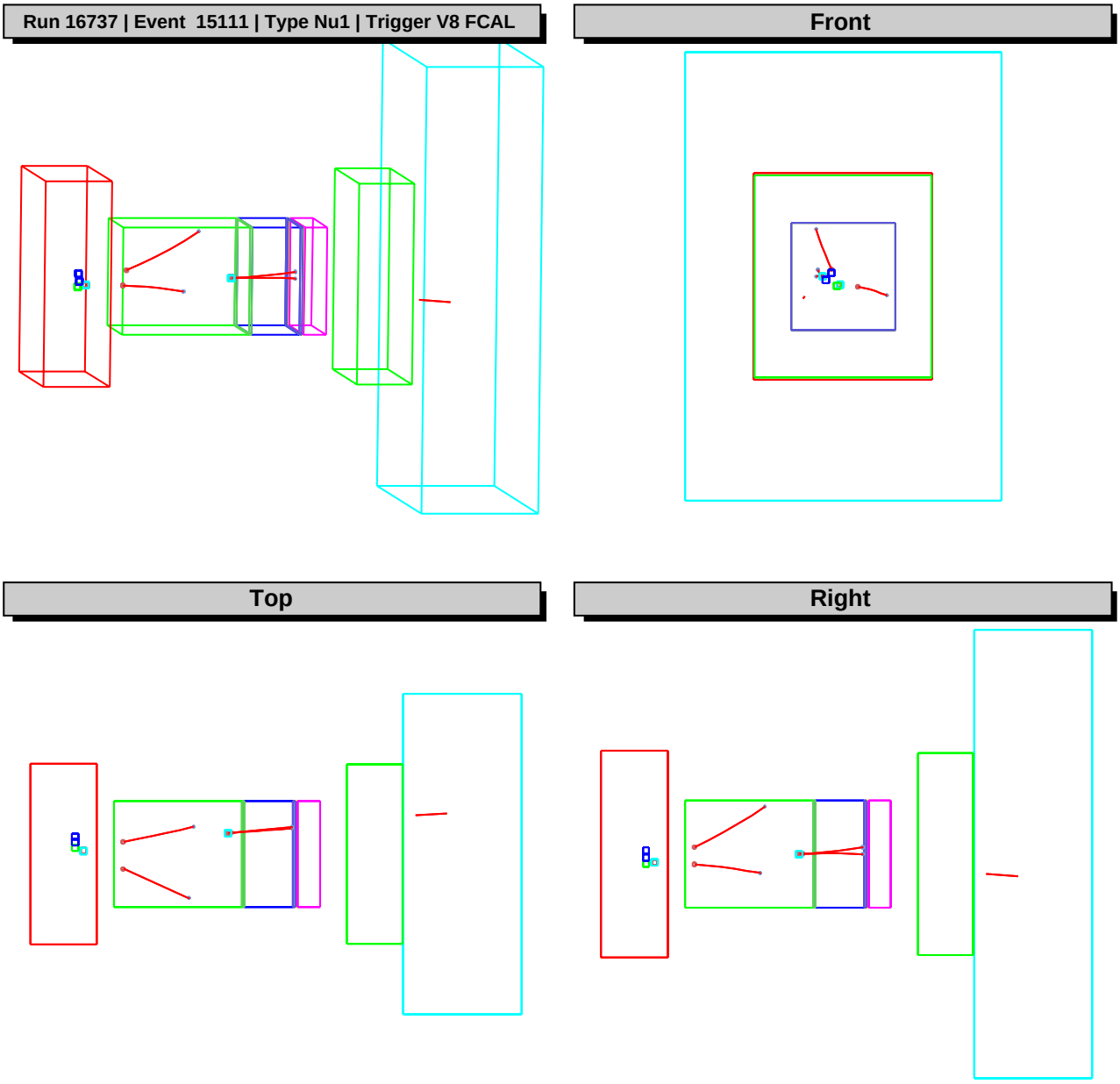

Figure 6.11: *Signal sample* $\mathcal{N}_\mu \to \mu^- X$ *survivor.*

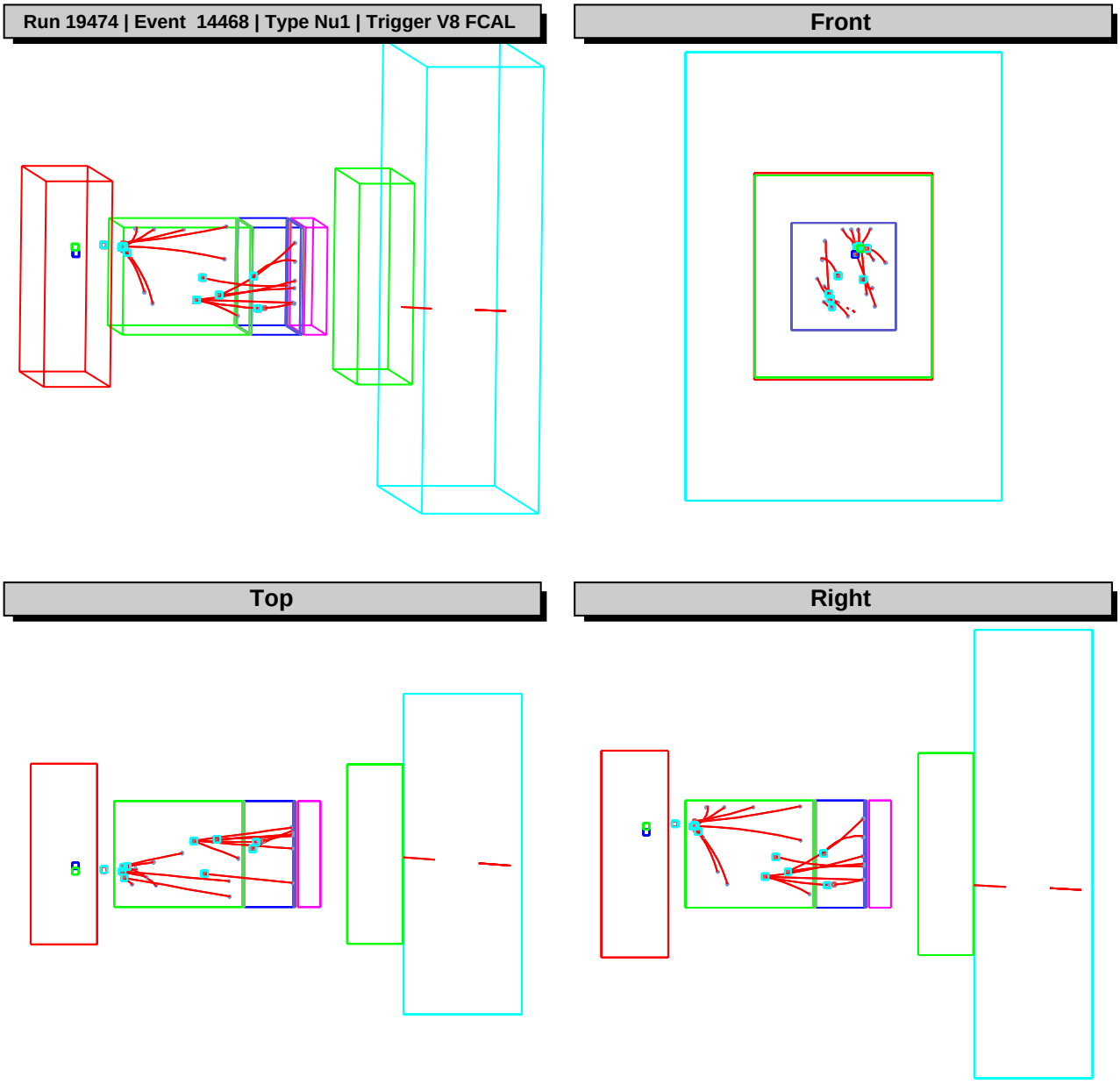

Figure 6.12: *Signal sample* $\mathcal{N}_\mu \to \mu^- X$ *survivor.*

6.7 Systematic uncertainties

Systematics enter in this analysis and in particular in the calculation of the sensitivity and the exclusion limits mainly from the following sources:

- **Differences between *MonteCarlo* and data**
  The neutral heavy lepton selection efficiencies are determined using *MonteCarlo* events. Because the event reconstruction for simulated and real data events is known to be slightly different, the calculated number of generated *MonteCarlo* events passing the selection cuts may vary.

- **Difference between signal and control sample**
  The neutrino charged current control sample is used to predict the number of signal events in neutral current interactions. The presence of the primary muon emerging from the FCAL may affect the selection of the secondary vertices.

- **Number of weak neutral current events**
  The sensitivities and limits are calculated using the number of neutral current events N_{NC}, so uncertainties enter directly.

Systematic uncertainties were in general small for this analysis. The different sources are discussed below.

Differences between *MonteCarlo* and data

The selection of neutral heavy lepton decay vertices can be compared to the selection efficiency of K^0_S with its similar topology. For K^0_S emerging from the FCAL the difference in reconstruction and selection between *MonteCarlo* and real data events was measured to be $\lesssim 1\%$ [124].

The differences in the particle identification for muons and leptons inside the NOMAD drift chambers are $\lesssim 1\%$ and $\lesssim 2\%$ [125] respectively.

Difference between signal and control sample

Using "stretched" K^0_S (cf. Page 117) *MonteCarlo* events, generated as neutral and charged current FCAL interactions and applying the neutral heavy lepton selection criteria, the effect of the existing primary muon is found to be $\lesssim 2\%$.

Number of weak neutral current events

The number of neutral current events is calculated using the measured number of charged current events in combination with their efficiency and the ratio of neutral current to charged current events (cf. Section 4.3). The overall systematic error is estimated as 5% for N_{NC}.

In the final event sample the ratio of neutral to charged current interactions is $\simeq 2$, in contrast to the measured (see Section 4.3)

$$\frac{n_{NC}}{n_{CC}} \simeq \frac{R_{\mathrm{NC/CC}} + (1 - \varepsilon_{\mathrm{CC}})}{\varepsilon_{\mathrm{CC}}} \simeq \frac{0.4 + (1 - 0.7)}{0.7} = 1 \tag{6.26}$$

indicating a bias (cf. Page 106) in the selection of neutral heavy lepton type events. A factor of 1 (cf. Page 109) has been used to predict the signal (neutral current) from the control sample (charge current) events. In the two leptonic decay modes zero events have been predicted and found, and in the semi-leptonic channel the error on the predicted and found events is large compared to the uncertainty on the applied factor 1.

Using the ν_{μ}^{CC} final sample as a control sample to predict the number of signal plus background ν^{NC} events does not allow to scale down the statistical uncertainty, because the number of events, the two samples are composed of, are in the same order of magnitude. On the other hand, the use of data events (control sample) to predict the number of expected data (signal sample) reduces the number of possible sources of uncertainties, as compared to the use of *MonteCarlo* events.

Chapter 7

Extraction of sensitivities and limits

In this chapter the results of the measurements of the studied neutral heavy lepton decay modes are used to calculate the sensitivities of the experiment and the upper confidence limits on the presence of $\mathcal{N}_\mu$ with its decay modes. The sensitivities and limits are translated into excluded regions in the $|U_{\mu\mu}|^2 \times m_{\mathcal{N}_\mu}$ plane.

First, the expected numbers of signal events $N_{\mathcal{N}_\mu}$ that pass the selection cuts, as a function of $m_{\mathcal{N}_\mu}$ and decay mode, will be computed.

The sensitivities and limits on the upper numbers of events n_2, consistent with the null hypothesis, are calculated according the Feldman-Cousins approach [126]. For these, the expected number of background events with their uncertainties and the numbers of measured events passing the selection cuts are used.

The expected numbers $N_{\mathcal{N}_\mu}$ and the upper numbers of events n_2 are combined to express the results of the measurements as excluded regions in parameter space.

Number of expected NHL

The expected number of measured muon type neutral heavy leptons produced in the FCAL and decaying in the drift chambers for given mixing parameter $|U_{\mu\mu}|^2$ and mass $m_{\mathcal{N}_\mu}$ can be calculated as (cf. Chapter 1 and 5):

$$N_{\mathcal{N}_\mu} = N_{NC} \times \left(1 - \frac{m^2_{\mathcal{N}_\mu}}{xs}\right)^2 \times |U_{\mu\mu}|^2 \times \varepsilon_{acc} \times BR \times \varepsilon_{rec} \tag{7.1}$$

with:

- N_{NC}: the number of weak neutral current interactions
- $\left(1 - \frac{m^2_{\mathcal{N}_\mu}}{xs}\right)^2$: the kinematical mass suppression factor

- BR: the branching ratio of the decay mode
- ε_{acc}: the geometrical acceptance, that is the NHL produced inside the target fiducial volume and decaying inside the analyzer fiducial volume
- ε_{rec}: the reconstruction and selection efficiencies depending on the NHL mass and decay mode

The number of neutral current interactions N_{NC} in the FCAL is evaluated using the corrected measured number of charged current interactions and the measured ratio of neutral to charged current interactions $R_{\mathrm{NC/CC}}$ (see Chapter 4).

$$\begin{aligned} N_{\mathrm{NC}}^{\mathrm{corr}} &= N_{\mathrm{CC}}^{\mathrm{corr}} \cdot R_{\mathrm{NC/CC}} \\ &= (18.21 \pm 0.03) \cdot 10^6 \times (0.40 \pm 0.02) \\ &= (7.28 \pm 0.36) \cdot 10^6 \end{aligned} \tag{7.2}$$

The branching ratios BR depend on the NHL mass and model. For simplicity, typical values for $m_{\mathcal{N}_\mu} = 2$ GeV/c^2 listed in Table 1.1 are used.

The suppression factor and the geometrical acceptance are calculated using the neutral heavy lepton *MonteCarlo* described in Chapter 5. For each value of $m_{\mathcal{N}_\mu}$ and $|U_{\mu\mu}|^2$ the probability of $NHLs$ produced in the FCAL and decaying inside the drift chambers *w.r.t.* standard neutral current interactions is evaluated (see Figure 5.11).

The reconstruction and selection efficiencies ε_{rec} for the different NHL decay modes were determined as a function of $m_{\mathcal{N}_\mu}$ in the previous chapter.

Sensitivity of the experiment

According to the Feldman-Cousins approach, the sensitivity is defined as "the average upper limit that would be attained by an ensemble of experiments with the same expected background and no true signal". In the absence of signal events, for a given experiment i, the resulting 90% confidence interval of measured events ($n_1^i < n^i < n_2^i$) may vary according to background fluctuations. In order to evaluate the 90% $C.L.$ upper limit n_2, the possible outcomes of the measurements in a large number of N identical experiments are simulated

$$n_2 = \frac{1}{N} \sum_{i=1} n_2^i \ , \tag{7.3}$$

taking into account the predicted number of background events with their uncertainties.

Applied to the situation of the three investigated decay modes

$$\begin{aligned} \mathcal{N}_\mu \to \mu^- \mu^+ \nu_\mu : &\quad 0_{-0}^{+1} \\ \mathcal{N}_\mu \to \mu^- e^+ \nu_e : &\quad 0_{-0}^{+1} \\ \mathcal{N}_\mu \to \mu^- X : &\quad 50 \pm 17 \end{aligned} \tag{7.4}$$

the average 90% *C.L.* sensitivities are calculated as:

$$n_2 = \begin{cases} 2.41 & \text{for } \mathcal{N}_\mu \to \mu^-\mu^+\nu_\mu \text{ and } \mathcal{N}_\mu \to \mu^- e^+\nu_e \\ 27.48 & \text{for } \mathcal{N}_\mu \to \mu^- X \end{cases} \tag{7.5}$$

Upper confidence limits

The 90% *C.L.* upper limits are obtained from the outcome of the actual experiment

$$\begin{aligned} \mathcal{N}_\mu \to \mu^-\mu^+\nu_\mu : &\quad 0 \\ \mathcal{N}_\mu \to \mu^- e^+\nu_e : &\quad 0 \\ \mathcal{N}_\mu \to \mu^- X : &\quad 27 \end{aligned} \tag{7.6}$$

in combination with the estimated backgrounds (cf. Equation 7.4) and evaluated using the Feldman-Cousins approach:

$$n_2 = \begin{cases} 2.42 & \text{for } \mathcal{N}_\mu \to \mu^-\mu^+\nu_\mu \text{ and } \mathcal{N}_\mu \to \mu^- e^+\nu_e \\ 7.56 & \text{for } \mathcal{N}_\mu \to \mu^- X \end{cases} \tag{7.7}$$

In the absence of signal events, the probabilities to obtain the quoted upper limits (cf. Equation 7.7) or lower can be evaluated using the distributions of the upper limits of N identical experiments:

$$P = \begin{cases} 90\% & \text{for } \mathcal{N}_\mu \to \mu^-\mu^+\nu_\mu \text{ and } \mathcal{N}_\mu \to \mu^- e^+\nu_e \\ < 1\% & \text{for } \mathcal{N}_\mu \to \mu^- X \end{cases} \tag{7.8}$$

For the two leptonic decay modes, the sensitivity and the limit agree since the numbers of predicted and measured events coincide. The upper confidence limit on the semi-leptonic channel is lower than the sensitivity of the experiment (cf. Equation 7.5), since the number of observed events is fewer than the estimated background (a "lucky" experiment). The corresponding probability for the limit is low, indicating that the predicted number of background events and/or its uncertainty for this decay mode was too conservative or has some additional systematic error. However, the result represents a measurement 1.35 σ less than the predicted background or 2.8 σ less than the average result obtained from N identical experiments with the same background and no true signal.

Including systematic errors

In order to include the effect of systematic uncertainties in the sensitivities and limits, the calculated upper numbers of events have to be modified, estimated as

$$n_2' = n_2 \times \sqrt{1 + \sum \left(\frac{\delta a}{a}\right)^2}, \tag{7.9}$$

where $(\delta a/a)$ are the fractional errors from all sources of systematic errors (cf. Section 6.7) and added in quadrature. The equation is an approximation that works if the fractional systematic errors are small, which is the case in this analysis.

Excluded regions in the $|U_{\mu\mu}|^2 \times m_{\mathcal{N}_\mu}$ plane

The calculated upper numbers of events for the existence of a $\mathcal{N}_\mu$ with its studied decay modes are translated into excluded regions in the $|U_{\mu\mu}|^2 \times m_{\mathcal{N}_\mu}$ plane. This is done by finding the $|U_{\mu\mu}|^2$ values for each mass $m_{\mathcal{N}_\mu}$ such that

$$N_{\mathcal{N}_\mu} = n_2' \tag{7.10}$$

where $N_{\mathcal{N}_\mu}$ is the number of signal events that pass the selection cuts which depends on the mass $m_{\mathcal{N}_\mu}$ and the decay mode. n_2' is the 90% *C.L.* upper limit on the observed number of events and the expected background events with included systematic errors for the relevant decay mode.

Figures 7.1 and 7.2 show the 90% *C.L.* limits for the leptonic and semileptonic decay modes of a muon type neutral heavy lepton $\mathcal{N}_\mu$ mixing with Standard Model left-handed neutrinos in the $|U_{\mu\mu}|^2 \times m_{\mathcal{N}_\mu}$ plane (solid lines). For comparison, the existing limits from previous experiments CCFR [60], CHARM-II [57] and L3 [51], (the latter represents a 95% *C.L.*), described in Chapter 1, are overlaid (dotted lines). These results may also be compared to the estimated sensitivity from the proposal of this experiment in Figure 1.4. The regions inside the curves are excluded.

The upper limits for each decay mode $\mathcal{N}_\mu \to \mu^-\mu^+\nu_\mu$ and $\mathcal{N}_\mu \to \mu^- e^+ \nu_e$ as well as their combined limit are depicted in Figure 7.1. For the semileptonic channel $\mathcal{N}_\mu \to \mu^- X$ the sensitivity and the upper limit are shown separately in Figure 7.2, as suggested in Reference [1], for the case when the number of observed events is less than the expected background: from the upper limit alone it is impossible to distinguish between a clean experiment with no background and a lucky experiment with fewer observed counts than expected background.

The results from this experiment for the different $\mathcal{N}_\mu$ decay modes are given separately for possible interpretations in the context of any appropriate model.

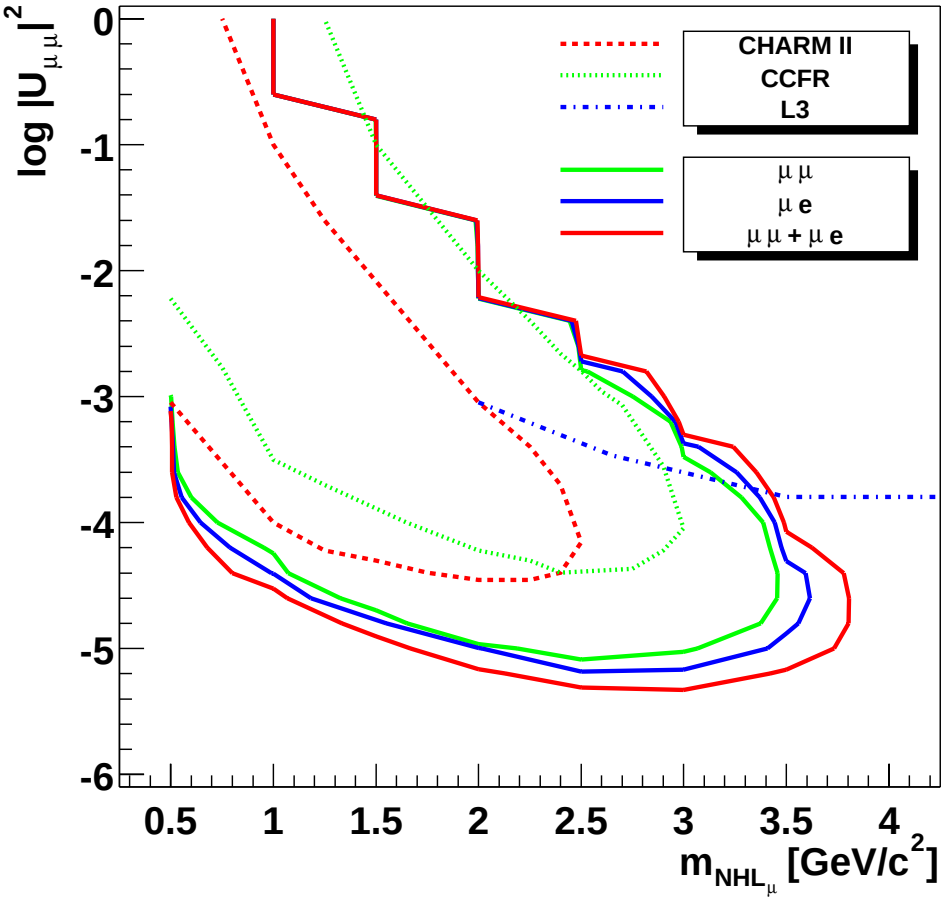

Figure 7.1: *Excluded regions in the* $|U_{\mu\mu}|^2 \times m_{\mathcal{N}_\mu}$ *plane for the decay channels* $\mathcal{N}_\mu \to \mu^-\mu^+\nu_\mu$ *and* $\mathcal{N}_\mu \to \mu^- e^+\nu_e$ *together with existing limits from previous experiments.*

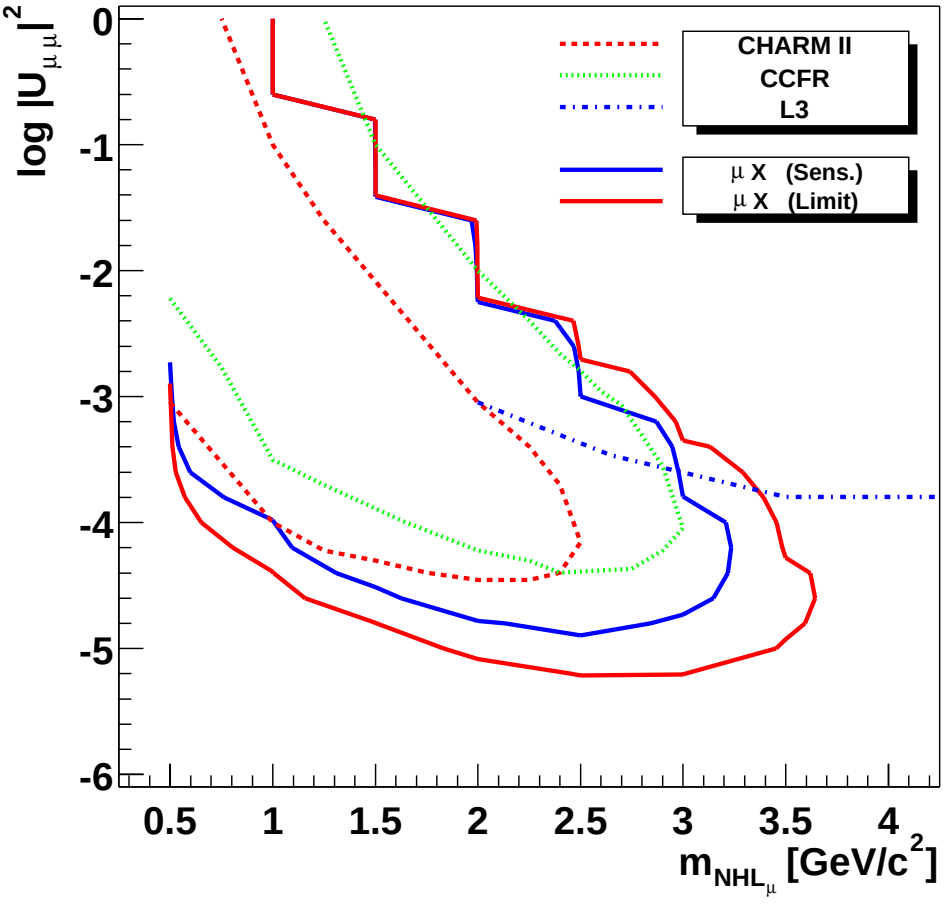

Figure 7.2: *Excluded regions (sensitivity and limit) in the* $|U_{\mu\mu}|^2 \times m_{\mathcal{N}_\mu}$ *plane for the semileptonic channel* $\mathcal{N}_\mu \to \mu^- X$ *together with existing limits from previous experiments.*

Summary and Conclusions

The NOMAD experiment, designed for the ν_τ appearance search via $\nu_\mu \leftrightarrow \nu_\tau$ oscillations in the CERN wideband neutrino beam, was taking data from 1994 to 1998. In 1995, the front iron support was instrumented to form an iron-scintillator sampling calorimeter (FCAL), acting as an additional instrumented heavy neutrino target for the study of several processes, among which are multi-muon production and the search for neutral heavy leptons.

Data collected during the 1996, 1997 and 1998 data taking periods was processed and analyzed. The FCAL has been calibrated by a comparison of *MonteCarlo* and neutrino interaction data. The measured numbers of neutrino interactions and the reconstructions of the visible hadronic energy in the FCAL, as well as the visible neutrino energy in charged current neutrino interactions, are in agreement with the *MonteCarlo* predictions. The FCAL timing resolution, in combination with the drift chamber track timing information, was studied for further use in the neutral heavy lepton analysis.

A search for muon type neutral heavy leptons $\mathcal{N}_\mu$, produced via mixing with Standard Model left-handed neutrinos in the FCAL target and decaying in the NOMAD drift chamber analyzer volume was performed with decay modes having a muon in the final state: $\mathcal{N}_\mu \to \mu^-\mu^+\nu_\mu$, $\mathcal{N}_\mu \to \mu^- e^+ \nu_e$ and $\mathcal{N}_\mu \to \mu^- X$.

The production and decay of the $\mathcal{N}_\mu$ was implemented in the NOMAD neutrino event generator according to the model described by Gronau, Leung and Rosner (GLR) [11].

In the context of the analysis 0^{+1}_{-0} events for the two $\mathcal{N}_\mu$ leptonic decay modes and (50 ± 17) events for the semileptonic decay mode were predicted. 0 and 27 events were observed respectively, consistent with a null hypothesis.

90% *C.L.* sensitivities and upper confidence limits of the experiment for the existence of the muon type neutral heavy lepton, according to the GLR model, have been evaluated in the Feldman-Cousins approach [126], using the expected number of background events, with their uncertainties, and the observed number of events passing the selection cuts. The limits have been translated into excluded regions in the $|U_{\mu\mu}|^2 \times m_{\mathcal{N}_\mu}$ parameter space plane and represent a considerable improvement on existing limits from previous experiments, sensitive in the same region of parameter space.

The result for the semi-leptonic decay mode $\mathcal{N}_\mu \to \mu^- X$ may be improved by imposing additional selection criteria based on the properties of the neutral heavy lepton. These, however, depend on the chosen model, resulting in a loss on generality of the search strategy. Further, additional heavy lepton *neutral current* decay modes, i.e. without a muon in the final state, may be included in the search, thereby also requiring extra assumptions about the $\mathcal{N}_\mu$, caused by the fact that the rejection power of the good lepton identification of the detector is unavailable. Neutral heavy lepton properties, such as the polarization and the mass dependence of the branching ratios, may also be analyzed and considered if one chooses to perform a more model dependent search strategy.

Appendix A

Signal *MonteCarlo* efficiencies

As described in Chapter 5, muon type neutral heavy lepton *MonteCarlo* events were generated for mass values of

$$m_{\mathcal{N}_\mu} = 0.5, 1.0, 1.5, 2.0, 2.5, 3.0, 3.5, 4.0, 4.5, 5.0, 5.5 \text{ and } 6.0 \text{ GeV}/c^2$$

for the three decay modes

$$\mathcal{N}_\mu \to \mu^- \mu^+ \nu_\mu$$

$$\mathcal{N}_\mu \to \mu^- e^+ \nu_e$$

$$\mathcal{N}_\mu \to \mu^- X$$

Within the analysis, selection cuts have been established common for all neutral heavy lepton decay channels (cf. Section 6.1) and specific for each mode (cf. Sections 6.3, 6.4 and 6.5). The breakdown in the generated events together with the relative efficiencies of the cuts (in % *w.r.t.* predecessor) are listed in the Tables

A.1 and A.2 for $\mathcal{N}_\mu \to \mu^- \mu^+ \nu_\mu$
A.3 and A.4 for $\mathcal{N}_\mu \to \mu^- e^+ \nu_e$
A.5 and A.6 for $\mathcal{N}_\mu \to \mu^- X$

The efficiencies in Figures 6.1, 6.4 and 6.9 depict the relative efficiencies of the lepton identification cuts and the overall efficiency for the corresponding decay mode.

These overall efficiencies are also used when evaluating the excluded regions in the $|U_{\mu\mu}|^2 \times m_{\mathcal{N}_\mu}$ parameter plane in Chapter 7.

$m_{\mathcal{N}_\mu}$	0.5		1.0		1.5		2.0		2.5		3.0	
PRE	579	100.00	567	100.00	647	100.00	638	100.00	654	100.00	654	100.00
Trigger	528	91.19	525	92.59	586	90.57	568	89.03	600	91.74	608	92.97
FCAL fid.	499	94.51	492	93.71	561	95.73	541	95.25	574	95.67	583	95.89
ν^{NC}	498	99.80	491	99.80	560	99.82	541	100.00	573	99.83	581	99.66
Vtx	490	100.00	489	100.00	559	100.00	541	100.00	573	100.00	581	100.00
Par & Dau	465	94.90	475	97.14	554	99.11	535	98.89	567	98.95	573	98.62
DC_X	464	99.78	475	100.00	554	100.00	535	100.00	567	100.00	573	100.00
DC_Y	464	100.00	475	100.00	554	100.00	535	100.00	567	100.00	573	100.00
$DC_{Z\min}$	445	95.91	468	98.53	550	99.28	532	99.44	565	99.65	566	98.78
$DC_{Z\max}$	443	99.55	468	100.00	549	99.82	532	100.00	565	100.00	566	100.00
μ@vtx	274	61.85	361	77.14	507	92.35	515	96.80	557	98.58	560	98.94
$p^v_{T,\max}$	256	93.43	357	98.89	500	98.62	511	99.22	556	99.82	559	99.82
Approach	256	100.00	357	100.00	499	99.80	510	99.80	555	99.82	557	99.64
$\text{Close}_{\text{Beg}}$	255	99.61	357	100.00	499	100.00	509	99.80	551	99.28	554	99.46
$\text{Close}_{\text{Hit}}$	255	100.00	357	100.00	498	99.80	508	99.80	550	99.82	554	100.00
$\text{Close}_{\text{End}}$	254	99.61	357	100.00	495	99.40	507	99.80	546	99.27	549	99.10
$\text{Approach}_{\text{Prox}}$	252	99.21	351	98.32	491	99.19	503	99.21	537	98.35	539	98.18
$\cos\theta^{up}_{min}$	252	100.00	351	100.00	490	99.80	503	100.00	537	100.00	539	100.00
$\cos\theta^{v}_{min}$	251	99.60	350	99.72	490	100.00	503	100.00	537	100.00	539	100.00
χ^2_{Vtx}	248	98.80	349	99.71	489	99.80	501	99.60	537	100.00	539	100.00
N_{DcVeto}	228	91.94	327	93.70	457	93.46	460	91.82	488	90.88	480	89.05
N_{Tube}	227	99.56	326	99.69	457	100.00	459	99.78	485	99.39	478	99.58
$\text{Track}_{\text{ZMin}}$	223	98.24	318	97.55	438	95.84	438	95.42	454	93.61	455	95.19
2 Tracks	222	99.55	317	99.69	432	98.63	435	99.32	448	98.68	450	98.90
$+\mu$	63	28.38	128	40.38	223	51.62	271	62.30	273	60.94	280	62.22

Table A.1: *Selection efficiencies for* $\mathcal{N}_\mu \to \mu^-\mu^+\nu_\mu$ *MonteCarlo events.*

$m_{\mathcal{N}_\mu}$	3.5		4.0		4.5		5.0		5.5		6.0	
PRE	647	100.00	640	100.00	627	100.00	584	100.00	598	100.00	574	100.00
Trigger	598	92.43	594	92.81	585	93.30	542	92.81	554	92.64	534	93.03
FCAL fid.	575	96.15	563	94.78	555	94.87	520	95.94	522	94.22	501	93.82
ν^{NC}	574	99.83	563	100.00	554	99.82	517	99.42	518	99.23	500	99.80
Vtx	573	100.00	562	100.00	554	100.00	517	100.00	517	100.00	499	100.00
Par & Dau	569	99.30	556	98.93	545	98.38	510	98.65	510	98.65	490	98.20
DC_X	569	100.00	556	100.00	545	100.00	510	100.00	510	100.00	490	100.00
DC_Y	569	100.00	556	100.00	545	100.00	510	100.00	510	100.00	490	100.00
$DC_{Z\min}$	565	99.30	556	100.00	541	99.27	506	99.22	500	98.04	485	98.98
$DC_{Z\max}$	563	99.65	556	100.00	539	99.63	506	100.00	500	100.00	484	99.79
μ@vtx	555	98.58	554	99.64	536	99.44	500	98.81	488	97.60	465	96.07
$p^v_{T,\max}$	554	99.82	554	100.00	536	100.00	500	100.00	488	100.00	465	100.00
Approach	552	99.64	552	99.64	536	100.00	500	100.00	488	100.00	465	100.00
$\text{Close}_{\text{Beg}}$	551	99.82	550	99.64	530	98.88	497	99.40	484	99.18	459	98.71
$\text{Close}_{\text{Hit}}$	550	99.82	549	99.82	529	99.81	497	100.00	484	100.00	459	100.00
$\text{Close}_{\text{End}}$	545	99.09	548	99.82	520	98.30	490	98.59	482	99.59	458	99.78
$\text{Approach}_{\text{Prox}}$	539	98.90	529	96.53	513	98.65	481	98.16	475	98.55	451	98.47
$\cos\theta^{up}_{min}$	539	100.00	528	99.81	512	99.81	480	99.79	475	100.00	451	100.00
$\cos\theta^{v}_{min}$	539	100.00	528	100.00	512	100.00	480	100.00	475	100.00	451	100.00
χ^2_{Vtx}	539	100.00	527	99.81	512	100.00	480	100.00	475	100.00	451	100.00
N_{DcVeto}	473	87.76	469	88.99	448	87.50	431	89.79	430	90.53	397	88.03
N_{Tube}	472	99.79	467	99.57	447	99.78	429	99.54	429	99.77	397	100.00
$\text{Track}_{\text{ZMin}}$	452	95.97	450	96.36	434	97.09	415	96.74	421	98.14	382	96.22
2 Tracks	448	99.12	444	98.67	430	99.08	412	99.28	415	98.57	380	99.48
$+\mu$	304	67.86	303	68.24	287	66.74	280	67.96	280	67.47	254	66.84

Table A.2: *Selection efficiencies for* $\mathcal{N}_\mu \to \mu^-\mu^+\nu_\mu$ *MonteCarlo events (cont'd).*

$m_{\mathcal{N}_\mu}$	0.5		1.0		1.5		2.0		2.5		3.0	
PRE	495	100.00	489	100.00	545	100.00	532	100.00	534	100.00	545	100.00
Trigger	456	92.12	446	91.21	491	90.09	476	89.47	494	92.51	514	94.31
FCAL fid.	429	94.08	420	94.17	468	95.32	455	95.59	471	95.34	488	94.94
ν^{NC}	429	100.00	420	100.00	467	99.79	454	99.78	471	100.00	485	99.39
Vtx	422	100.00	418	100.00	465	100.00	453	100.00	470	100.00	485	100.00
Par & Dau	387	91.71	399	95.45	453	97.42	443	97.79	459	97.66	474	97.73
DC_X	387	100.00	399	100.00	453	100.00	443	100.00	459	100.00	474	100.00
DC_Y	387	100.00	399	100.00	453	100.00	443	100.00	459	100.00	474	100.00
$DC_{Z\min}$	370	95.61	390	97.74	447	98.68	439	99.10	455	99.13	470	99.16
$DC_{Z\max}$	368	99.46	389	99.74	446	99.78	439	100.00	454	99.78	469	99.79
μ@vtx	166	45.11	231	59.38	332	74.44	364	82.92	398	87.67	413	88.06
$p^v_{T,\max}$	155	93.37	227	98.27	331	99.70	363	99.73	397	99.75	412	99.76
Approach	154	99.35	227	100.00	331	100.00	361	99.45	396	99.75	411	99.76
$\text{Close}_{\text{Beg}}$	154	100.00	226	99.56	331	100.00	359	99.45	395	99.75	409	99.51
$\text{Close}_{\text{Hit}}$	154	100.00	226	100.00	331	100.00	358	99.72	395	100.00	409	100.00
$\text{Close}_{\text{End}}$	153	99.35	225	99.56	328	99.09	357	99.72	391	98.99	408	99.76
$\text{Approach}_{\text{Prox}}$	153	100.00	225	100.00	325	99.09	354	99.16	386	98.72	403	98.77
$\cos\theta^{up}_{min}$	153	100.00	225	100.00	325	100.00	354	100.00	386	100.00	403	100.00
$\cos\theta^{v}_{min}$	153	100.00	225	100.00	325	100.00	354	100.00	386	100.00	403	100.00
χ^2_{Vtx}	149	97.39	222	98.67	323	99.38	346	97.74	384	99.48	397	98.51
N_{DcVeto}	140	93.96	207	93.24	300	92.88	311	89.88	343	89.32	360	90.68
N_{Tube}	139	99.29	205	99.03	298	99.33	311	100.00	343	100.00	358	99.44
$\text{Track}_{\text{ZMin}}$	138	99.28	201	98.05	287	96.31	297	95.50	322	93.88	339	94.69
2 Tracks	137	99.28	197	98.01	286	99.65	293	98.65	319	99.07	333	98.23
+e	82	59.85	99	50.25	160	55.94	156	53.24	201	63.01	204	61.26

Table A.3: *Selection efficiencies for $\mathcal{N}_\mu \to \mu^- e^+ \nu_e$ MonteCarlo events.*

$m_{\mathcal{N}_\mu}$	3.5		4.0		4.5		5.0		5.5		6.0	
PRE	531	100.00	529	100.00	518	100.00	508	100.00	485	100.00	481	100.00
Trigger	490	92.28	496	93.76	469	90.54	475	93.50	456	94.02	447	92.93
FCAL fid.	468	95.51	472	95.16	452	96.38	453	95.37	433	94.96	420	93.96
ν^{NC}	467	99.79	471	99.79	452	100.00	452	99.78	432	99.77	420	100.00
Vtx	467	100.00	470	100.00	452	100.00	451	100.00	430	100.00	420	100.00
Par & Dau	457	97.86	463	98.51	441	97.57	444	98.45	411	95.58	407	96.90
DC_X	457	100.00	463	100.00	441	100.00	444	100.00	411	100.00	407	100.00
DC_Y	457	100.00	463	100.00	441	100.00	444	100.00	411	100.00	407	100.00
$DC_{Z\min}$	454	99.34	462	99.78	437	99.09	441	99.32	407	99.03	401	98.53
$DC_{Z\max}$	454	100.00	460	99.57	436	99.77	441	100.00	407	100.00	401	100.00
μ@vtx	401	88.33	406	88.26	393	90.14	389	88.21	350	86.00	350	87.28
$p^v_{T,\max}$	401	100.00	406	100.00	392	99.75	389	100.00	350	100.00	350	100.00
Approach	400	99.75	405	99.75	390	99.49	388	99.74	350	100.00	348	99.43
$\text{Close}_{\text{Beg}}$	397	99.25	404	99.75	387	99.23	388	100.00	349	99.71	342	98.28
$\text{Close}_{\text{Hit}}$	397	100.00	404	100.00	387	100.00	388	100.00	349	100.00	342	100.00
$\text{Close}_{\text{End}}$	393	98.99	399	98.76	385	99.48	382	98.45	345	98.85	341	99.71
$\text{Approach}_{\text{Prox}}$	384	97.71	385	96.49	381	98.96	378	98.95	340	98.55	335	98.24
$\cos\theta^{up}_{min}$	384	100.00	384	99.74	381	100.00	378	100.00	340	100.00	335	100.00
$\cos\theta^{v}_{min}$	384	100.00	384	100.00	381	100.00	378	100.00	340	100.00	335	100.00
χ^2_{Vtx}	382	99.48	383	99.74	380	99.74	376	99.47	339	99.71	334	99.70
N_{DcVeto}	344	90.05	352	91.91	335	88.16	334	88.83	303	89.38	297	88.92
N_{Tube}	337	97.97	349	99.15	335	100.00	332	99.40	302	99.67	295	99.33
$\text{Track}_{\text{ZMin}}$	327	97.03	337	96.56	320	95.52	323	97.29	296	98.01	284	96.27
2 Tracks	323	98.78	332	98.52	318	99.38	316	97.83	290	97.97	283	99.65
+e	211	65.33	201	60.54	201	63.21	193	61.08	197	67.93	177	62.54

Table A.4: *Selection efficiencies for $\mathcal{N}_\mu \to \mu^- e^+ \nu_e$ MonteCarlo events (cont'd).*

$m_{\mathcal{N}_\mu}$	0.5		1.0		1.5		2.0		2.5		3.0	
PRE	559	100.00	573	100.00	639	100.00	616	100.00	619	100.00	622	100.00
Trigger	515	92.13	526	91.80	574	89.83	556	90.26	572	92.41	572	91.96
FCAL fid.	486	94.37	506	96.20	545	94.95	530	95.32	548	95.80	548	95.80
ν^{NC}	485	99.79	505	99.80	545	100.00	525	99.06	546	99.64	548	100.00
Vtx	480	100.00	499	100.00	544	100.00	525	100.00	546	100.00	548	100.00
Par & Dau	455	94.79	483	96.79	537	98.71	524	99.81	543	99.45	546	99.64
DC_X	455	100.00	483	100.00	537	100.00	524	100.00	543	100.00	546	100.00
DC_Y	455	100.00	483	100.00	537	100.00	524	100.00	543	100.00	546	100.00
$DC_{Z\min}$	442	97.14	475	98.34	534	99.44	520	99.24	542	99.82	546	100.00
$DC_{Z\max}$	437	98.87	473	99.58	530	99.25	519	99.81	542	100.00	543	99.45
μ@vtx	156	35.70	273	57.72	374	70.57	406	78.23	454	83.76	464	85.45
$p^v_{T,\max}$	139	89.10	270	98.90	373	99.73	402	99.01	452	99.56	463	99.78
Approach	133	95.68	268	99.26	372	99.73	398	99.00	445	98.45	453	97.84
$\text{Close}_{\text{Beg}}$	131	98.50	265	98.88	353	94.89	367	92.21	398	89.44	392	86.53
$\text{Close}_{\text{Hit}}$	130	99.24	265	100.00	352	99.72	367	100.00	397	99.75	391	99.74
$\text{Close}_{\text{End}}$	128	98.46	265	100.00	351	99.72	363	98.91	393	98.99	385	98.47
$\text{Approach}_{\text{Prox}}$	128	100.00	264	99.62	347	98.86	356	98.07	384	97.71	381	98.96
$\cos\theta^{up}_{min}$	128	100.00	263	99.62	347	100.00	356	100.00	384	100.00	381	100.00
$\cos\theta^{v}_{min}$	128	100.00	263	100.00	346	99.71	355	99.72	383	99.74	379	99.48
χ^2_{Vtx}	123	96.09	262	99.62	343	99.13	354	99.72	381	99.48	378	99.74
N_{DcVeto}	117	95.12	243	92.75	322	93.88	338	95.48	354	92.91	357	94.44
N_{Tube}	117	100.00	241	99.18	322	100.00	337	99.70	354	100.00	356	99.72
$\text{Track}_{\text{ZMin}}$	113	96.58	236	97.93	315	97.83	323	95.85	340	96.05	342	96.34
$\vec{r}_{\text{first hit}}$	113	100.00	236	100.00	315	100.00	323	100.00	340	100.00	342	100.00
$\delta p/p$	113	100.00	236	100.00	315	100.00	323	100.00	340	100.00	342	100.00
χ^2_{Trk}	113	100.00	236	100.00	315	100.00	323	100.00	340	100.00	342	100.00
N_{good}	101	89.38	217	91.95	302	95.87	308	95.36	326	95.88	331	96.78
K^0_{S}	18	17.82	130	59.91	263	87.09	290	94.16	317	97.24	327	98.79
$q=0$	11	61.11	123	94.62	248	94.30	276	95.17	296	93.38	300	91.74
$\Delta t^{\text{c}}_{\text{Vtx}}$	11	100.00	118	95.93	232	93.55	259	93.84	286	96.62	289	96.33

Table A.5: *Selection efficiencies for* $\mathcal{N}_\mu \to \mu^- X$ *MonteCarlo events.*

$m_{\mathcal{N}_\mu}$	3.5		4.0		4.5		5.0		5.5		6.0	
PRE	619	100.00	603	100.00	577	100.00	550	100.00	539	100.00	517	100.00
Trigger	571	92.25	559	92.70	533	92.37	513	93.27	509	94.43	492	95.16
FCAL fid.	545	95.45	527	94.28	513	96.25	491	95.71	481	94.50	465	94.51
ν^{NC}	544	99.82	525	99.62	511	99.61	489	99.59	481	100.00	465	100.00
Vtx	544	100.00	525	100.00	511	100.00	489	100.00	481	100.00	465	100.00
Par & Dau	540	99.26	523	99.62	507	99.22	483	98.77	473	98.34	464	99.78
DC_X	540	100.00	523	100.00	507	100.00	483	100.00	473	100.00	464	100.00
DC_Y	540	100.00	523	100.00	507	100.00	483	100.00	473	100.00	464	100.00
$DC_{Z\min}$	538	99.63	522	99.81	504	99.41	481	99.59	470	99.37	464	100.00
$DC_{Z\max}$	535	99.44	520	99.62	501	99.40	479	99.58	467	99.36	460	99.14
μ@vtx	458	85.61	436	83.85	431	86.03	403	84.13	389	83.30	369	80.22
$p^v_{T,\max}$	454	99.13	433	99.31	431	100.00	402	99.75	388	99.74	369	100.00
Approach	443	97.58	426	98.38	421	97.68	393	97.76	380	97.94	357	96.75
$\text{Close}_{\text{Beg}}$	377	85.10	360	84.51	340	80.76	293	74.55	290	76.32	265	74.23
$\text{Close}_{\text{Hit}}$	377	100.00	359	99.72	337	99.12	293	100.00	287	98.97	261	98.49
$\text{Close}_{\text{End}}$	375	99.47	354	98.61	328	97.33	286	97.61	285	99.30	256	98.08
$\text{Approach}_{\text{Prox}}$	369	98.40	350	98.87	325	99.09	285	99.65	281	98.60	254	99.22
$\cos\theta^{up}_{min}$	369	100.00	350	100.00	325	100.00	285	100.00	280	99.64	254	100.00
$\cos\theta^{v}_{min}$	368	99.73	349	99.71	325	100.00	284	99.65	280	100.00	253	99.61
χ^2_{Vtx}	368	100.00	347	99.43	325	100.00	282	99.30	279	99.64	253	100.00
N_{DcVeto}	348	94.57	339	97.69	319	98.15	273	96.81	272	97.49	247	97.63
N_{Tube}	348	100.00	338	99.71	318	99.69	273	100.00	272	100.00	245	99.19
$\text{Track}_{\text{ZMin}}$	333	95.69	325	96.15	306	96.23	267	97.80	266	97.79	235	95.92
$\vec{r}_{\text{first hit}}$	333	100.00	325	100.00	306	100.00	267	100.00	266	100.00	235	100.00
$\delta p/p$	333	100.00	325	100.00	306	100.00	267	100.00	266	100.00	235	100.00
χ^2_{Trk}	333	100.00	325	100.00	306	100.00	267	100.00	266	100.00	235	100.00
N_{good}	324	97.30	319	98.15	300	98.04	265	99.25	261	98.12	232	98.72
K^0_{S}	320	98.77	318	99.69	297	99.00	264	99.62	261	100.00	232	100.00
$q=0$	289	90.31	276	86.79	261	87.88	216	81.82	212	81.23	191	82.33
$\Delta t^{\text{c}}_{\text{Vtx}}$	279	96.54	265	96.01	250	95.79	205	94.91	198	93.40	181	94.76

Table A.6: *Selection efficiencies for* $\mathcal{N}_\mu \to \mu^- X$ *MonteCarlo events (cont'd).*

List of Figures

List of Tables

Bibliography

[1] Particle Data Group, *Review of Particle Physics*, Eur. Phys. J. **C3** (1998).

[2] N. Schmitz, *Neutrinophysik*, (B. G. Teubner, 1997).

[3] H. Georgi and S.L. Glashow, *Unity of All Elementary-Particle Forces*, Phys. Rev. Lett. **32**, 438 (1974).

[4] H. Georgi, in *Particles and Fields - 1974*, Proceedings of the Meeting of APS Division of Particles and Fields, Williamsburg, Virginia p. 575, ed. C.E. Carlson (AIP), New York, 1975.

[5] H. Fritsch and P. Minkowski, *Unified Interactions of Leptons and Hadrons*, Ann. Phys. (NY) **93**, 193 (1975).

[6] R.N. Mohapatra, G. Senjanovic, *Neutrino Masses and Mixings in Gauge Models With Spontaneous Parity Violation*, Phys. Rev. **D23**, 165–180 (1981), also in: FERMILAB-Pub-80/61-THY.

[7] M. Gell-Mann *et al.*, *Supergravity* p. 315 (1979), Amsterdam.

[8] P. Langacker, *Neutrino Physics*, (Berlin, 1988).

[9] M. Cvetic (ed.), *Proceedings of TASI-90*, Singapor (1991), World Scientific.

[10] E. Witten, *Neutrino masses in the minimal $O(10)$ Theory*, Phys. Lett. **B91**, 81 (1980).

[11] M. Gronau, C.N. Leung, J.L. Rosner, *Extending limits on neutral heavy leptons*, Phys. Rev. **D29**, 2539 (1984).

[12] C.H. Albright, C. Jarlskog, *Neutrino production of M^+ and E^- heavy leptons*, Nucl. Phys. **B84**, 467–492 (1975).

[13] T. Bolton, *Neutral Heavy Lepton Decays*, NuTeV physics memorandum (1995), http://www-e815.fnal.gov/~e815/physics_memos.html.

[14] A. Hime *et al.*, *On the 17-keV conundrum*, Nucl. Phys. **B31**, 50 (1993).

[15] J.J. Simpson, *Limits on the emission of heavy neutrinos in ^3H decay*, Phys. Rev. **D24**, 2971 (1981).

[16] D.W. Hetherington *et al.*, *Upper limits on the mixing of heavy neutrinos in the beta decay of ^{63}Ni*, TASCC-87-P-5 (1987).

[17] T. Ohi *et al.*, *Search for heavy neutrinos in the beta decay of ^{35}S. Evidence against the 17 keV heavy neutrino*, Phys. Lett. **B160**, 322 (1985).

[18] A.M. Apalikov *et al.*, *Search for heavy neutrinos in β decay*, JETP Lett. **42**, 289 (1985).

[19] J. Markey und F. Boehm, *Search for admixture of heavy neutrinos with masses between 5 and 55 keV*, Phys. Rev. **C32**, 2215 (1985).

[20] K. Schreckenbach *et al.*, *Search for mixing of heavy neutrinos in the β^+ and β^- spectra of the ^{64}Cu decay*, Phys. Lett. **B129**, 265 (1983).

[21] J. Deutsch *et al.*, *Searches for admixture of massive neutrinos into the electron flavour*, Nucl. Phys. **A518**, 149 (1990).

[22] J.C. Hardy *et al.*, *Fermi beta decay and the vector coupling constant: tests of CVC and the Standard Model*, TASC-P-90-7 .

[23] L. Oberauer *et al.*, *Experimental limits on the decay of reactor neutrinos*, Phys. Lett. **B198**, 113 (1987).

[24] V.I. Kopeikin *et al.*, *Search for massive neutrinos at the Rovno nuclear power station reactor*, JETP Lett. **51**, 86 (1990).

[25] C. Hagner *et al.*, *Experimental search for the neutrino decay $\nu_3 \to \nu_j + e^+ + e^-$ and limits on neutrino mixing*, Phys. Rev. **D52**, 1343 (1995).

[26] D.A. Bryman *et al.*, *Search for Massive Neutrinos in the Decay $\pi \to e\nu$*, Phys. Rev. Lett. **50**, 1546 (1983).

[27] G. Azuelos *et al.*, *Constraints on Massive Neutrinos in $\pi \to e\nu$ Decay*, Phys. Rev. Lett. **56**, 2241 (1986).

[28] N. De Leener-Rosier *et al.*, *Search for massive neutrinos in $\pi \to e\nu$ decay*, Phys. Rev. **D43**, 3611 (1991).

[29] G. Bernardi *et al.*, *Further limits on heavy neutrino couplings*, Phys. Lett. **B203**, 332 (1988).

[30] F. Bergsma *et al.*, *A search for decays of heavy neutrinos*, Phys. Lett. **B128**, 361 (1983).

[31] T. Yamazaki *et al.*, *A new improved experiment to search for heavy neutrinos and neutral bosons in kaon decay*, Proc. Neutrino 84 (1984).

[32] J. Dorenbusch *et al.*, *A search for decays of heavy neutrinos in the mass range 0.5-2.8 GeV*, Phys. Lett. **B166**, 473–478 (1986), CERN EP/85-190.

[33] S. Baranov *et al.*, *Search for heavy neutrinos at the IHEP-JINR Neutrino Detector*, Phys. Lett. **B302**, 336 (1993).

[34] A.M. Cooper-Sarkar *et al.*, *Search for heavy neutrino decays in the BEBC beam dump experiment*, Phys. Lett. **B160**, 207 (1985).

[35] M.E. Duffy *et al.*, *Neutrino production by 400-GeV/c protons in a beam-dump experiment*, Phys. Rev. **D38**, 2032 (1988).

[36] J. Badier *et al.*, *Mass and Lifetime Limits on New Long-Lived Particles in 300 GeV/c π^- Interactions*, Z. f. Physik **C31**, 21 (1986).

[37] M. Daum *et al.*, *Search for admixtures of massive neutrinos in the decay* $\pi^+ \to \mu^+ + \nu$, Phys. Rev. **D36**, 2624 (1987).

[38] R.C. Minehart *et al.*, *Search for Admixture of Massive Neutrinos in the decay* $\pi^+ \to \mu^+ + \overline{\nu}$, Phys. Rev. Lett. **52**, 804 (1984).

[39] R. Abela *et al.*, *Search for an admixture of heavy neutrino states in pion decay*, Phys. Lett. **B105**, 263 (1981).

[40] F.P. Calaprice *et al.*, *Search for finite-mass neutrinos in the decay* $\pi^+ \to \mu^+\nu_\mu$, Phys. Lett. **B106**, 175 (1981).

[41] D.A. Bryman and T. Numao, *Search for massive neutrinos in* $\pi^+ \to \mu^+\nu$ *decay*, Phys. Rev. **D53**, 558 (1996).

[42] R.S. Hayano *et al.*, *Heavy-Neutrino search using* $K_{\mu 2}$ *decay*, Phys. Rev. Lett. **49**, 1305 (1982).

[43] Y. Asano *et al.*, *Search for a heavy neutrino emitted in* $K^+ \to \mu^+\nu$ *decay*, Phys. Lett. **B104**, 84 (1981).

[44] C.Y. Pang *et al.*, *Search for Rare K^+ Decays. I.* $K^+ \to \mu^+\nu\overline{\nu}\nu^*$, Phys. Rev. **D8**, 1989 (1973).

[45] R.B. Drucker *et al.*, *Search for Neutral Heavy Leptons in the NuTeV Experiment at Fermilab*, hep-ex/9811036 .

[46] E. Gallas *et al.*, *Search for neutral weakly interacting massive particles in the Fermilab Tevatron wideband neutrino beam*, Phys. Rev. **D52**, 6 (1995).

[47] A. Vaitaitis *et al.*, *Search for neutral heavy leptons in a high-energy neutrino beam*, Phys. Rev. Lett. **83**, 4943–4946 (1999).

[48] A. Vaitaitis, *Search for neutral heavy leptons in a high-energy neutrino beam*, Ph.D. thesis, Columbia University, New York (2000).

[49] L. Bryant *et al.*, *Search for Isosinglet Neutral Heavy Leptons in ALEPH*, ALEPH 97-079 (1997).

[50] P. Abreu *et al.*, *Search for Neutral Heavy Leptons Produced in Z Decays*, CERN-PPE/96-195 (1996).

[51] O. Adriani *et al.*, *Search for isosinglet neutral heavy leptons in Z^0 decays*, Phys. Lett. **B295**, 371 (1992).

[52] M.Z. Akrawy *et al.*, *Limits on neutral heavy lepton production from Z^0 decay*, Phys. Lett. **B247**, 448 (1990).

[53] A.N. Diddens *et al.*, CHARM Collaboration, *A detector for neutral-current interactions of high-energy neutrinos*, Nucl. Inst. & Meth. **178**, 24–48 (1980).

[54] J. Dorenbusch *et al.*, CHARM Collaboration, *Calibration of the CHARM fine-grained calorimeter*, Nucl. Inst. & Meth. **A253**, 203–221 (1987).

[55] W.K. Sakamoto *et al.*, CCFR Collaboration, *Calibration of the CCFR target calorimeter*, Nucl. Inst. & Meth. **A294**, 179–192 (1990).

[56] B.J. King *et al.*, CCFR Collaboration, *Measuring muon momenta with the CCFR neutrino detector*, Nucl. Inst. & Meth. **A302**, 254–260 (1991).

[57] P. Vilain *et al.*, *Search for heavy isosinglet neutrinos*, Phys. Lett. **B343**, 453–458 (1995).

[58] P. de Barbaro *et al.*, *A study of double vertex events in the neutrino-nucleon interactions*, UR-1291 (1992).

[59] P. de Barbaro, *Search for neutral heavy leptons in neutrino-nucleon interactions at the FNAL tevatron*, Ph.D. thesis, University of Rochester, Rochester, New York (1990).

[60] S.R. Mishra *et al.*, *Search for Neutral Heavy Leptons from $\nu - N$ Scattering*, Phys. Rev. Lett. **59**, 1397–1400 (1987).

[61] B. Armbruster *et al.*, *Anomaly in the time distribution of neutrinos from a pulsed beam stop source*, Phys. Lett. **B348**, 19 (1995).

[62] R. Bilger et al., *Search for the hypothetical $\pi \to \mu x$ decay*, Phys. Lett. **B363**, 41 (1995).

[63] M. Daum et al., *Search for a neutral particle of mass 33.9 MeV in pion decay*, Phys. Lett. **B361**, 179 (1995).

[64] M. Daum et al., *Search for a neutral particle of mass 33.9 MeV in pion decay* (1997), http://www1.psi.ch/~jschott/index.html#heavy.

[65] S.N. Gninenko und N.V. Krasnikov, *Exotic muon decays and the KARMEN anomaly*, Phys. Lett. **B434**, 163 (1998).

[66] R. Bilger et al., *Search for Exotic Muon Decays*, Phys. Lett. **B446**, 363 (1999).

[67] J. Altegoer *et al.*, *Instrumenting the Front 'I's of NOMAD*, NOMAD memo 95-011 (1995), CERN, Geneva.

[68] NOMAD Collaboration, P. Astier *et al.*, *NOMAD proposal: search for the oscillation ν_μ–ν_τ*, CERN-SPSLC/91-21 (1991); SPSLC P 261 (1991), CERN Geneva, Add. 1: CERN-SPSLC/91-48 (1991), Add. 2: CERN-SPSLC/91-53 (1991).

[69] CHORUS Collaboration, *CHORUS proposal: A new search for $\nu_\mu - \nu_\tau$ oscillations*, CERN-SPSC/90-42 (1990) .

[70] NOMAD Collaboration, J. Altegoer *et al.*, *A search for $\nu_\mu \leftrightarrow \nu_\tau$ oscillations using the NOMAD detector*, Phys. Lett. **B431**, 219–236 (1998).

[71] NOMAD Collaboration, J. Altegoer *et al.*, *A more sensitive search for $\nu_\mu \leftrightarrow \nu_\tau$ oscillations in NOMAD*, Phys. Lett. **B453**, 169–186 (1999).

[72] *GEANT: Detector description and simulation tool*, CERN Programming Library Long Writeup W5013 .

[73] B. Van de Vyver, P. Zucchelli - CHORUS Collaboration, *Prompt ν_τ background in Wide Band ν_μ Beams*, CERN PPE/96-113 (August 1996).

[74] M.C. Gonzalez-Garcia, J.J. Gomez-Cadenas, *Prompt ν_τ Fluxes in Present and Future Tau Neutrino Experiments*, CERN TH/96-220 (August 1996).

[75] NOMAD Collaboration, J. Altegoer *et al.*, *The NOMAD experiment at the CERN SPS*, Nucl. Inst. & Meth. **A404**, 96–128 (1998).

[76] A. Geiser, J. Gosset and F. Weber, *Conventions for the NOMAD Coordinate System*, NOMAD memo 94-080 (1994), CERN, Geneva.

[77] J. Altegoer *et al.*, *The trigger system of the NOMAD experiment*, Nucl. Inst. & Meth. **A428**, 299–316 (1999).

[78] B. Schmidt, *Study of ν_μ-Charged-Current Interactions and Search for $\nu_\mu \leftrightarrow \nu_\tau$ Oscillations in the Channel $\tau^- \rightarrow \mu^- \overline{\nu}_\mu \nu_\tau$ with the NOMAD Detector at the CERN Wideband Neutrino beam*, Doktorarbeit, Universität Dortmund, Germany (1997).

[79] T. Wolff, *Suche nach neutralen schweren Leptonen*, Doktorarbeit, Universität Münster, Germany (2000).

[80] T. Weiße, *Comparison of muonic and electronic final states in the NOMAD experiment at the CERN wide-band neutrino beam*, Doktorarbeit, Universität Dortmund, Germany (1997).

[81] A. Fasso *et al.*, *FLUKA92*, Proc. of the Workshop on Simulating Accelerator Radiation Environments (1993), Santa Fe, USA.

[82] J.P. Meyer, A. Rubbia, *NOMAD Event Generator Off-line Manual* (1996).

[83] G. Ingelman, A. Edin and J. Rathsman, *LEPTO 6.5 - A Monte Carlo Generator for Deep Inelastic Lepton-Nucleon Scattering*, Comp. Phys. Comm. **101**, 108–134 (1997), hep-ph/9605286, DESY-96-057.

[84] B. Andersson, G. Gustafson, G. Ingelman, T. Sjöstrand, *Parton Fragmentation and String Dynamics*, Phys. Rep. **97**, 31 (1983).

[85] T. Sjöstrand, *High-energy-physics event generation with PYTHIA 5.7 and JETSET 7.4*, Comp. Phys. Comm. **82**, 74–89 (1994).

[86] M. Glück, E. Reya, A. Vogt, *Parton distributions for high energy collisions*, Z. f. Physik **C53**, 127–134 (1992).

[87] H. Plothow-Besch, *PDFLIB: a library of all available parton density functions of the nucleon, pion and the photon and the corresponding α_s calculations*, Comp. Phys. Comm. **75**, 396 (1993).

[88] S. Jadach, B.F.L Ward, Z. Was, *The Monte Carlo program KORALZ version 3.8 for the lepton or quark pair production at LEP/SLC energies*, Comp. Phys. Comm. **66**, 276 (1991), also in: CERN-TH-5994 preprint.

[89] S. Jadach, B.F.L Ward, Z. Was, *The Monte Carlo program KORALZ version 4.0 for the lepton or quark pair production at LEP/SLC energies*, Comp. Phys. Comm. **79**, 503 (1994), also in: CERN-TH-7075 preprint, 1993.

[90] S. Jadach, Z. Was, J.H. Kühn, *TAUOLA - a library of Monte Carlo programs to simulate decays of polarized τ leptons*, Comp. Phys. Comm. **64**, 275–299 (1991), also in: CERN-TH-5856 preprint.

[91] M. Jezabek, Z. Was, S. Jadach, J.H. Kühn, *The τ decay library TAUOLA, update with exact $\mathcal{O}(\alpha)$ QED corrections in $\tau \to \mu(e)\nu\overline{\nu}$ decay modes*, Comp. Phys. Comm. **70**, 69–76 (1992), also in: CERN-TH-6195 preprint.

[92] J. Altegoer *et al.*, *NOMAD GEANT Off-line Manual* (1994).

[93] S.B. Boyd, *A Study of ν_μ^{CC} Interactions in the FCAL*, NOMAD memo 98-015 (1998), CERN, Geneva.

[94] D. Geppert, *Bau von Komponenten eines Szintillator-Hadron-Kalorimeters und dessen Kalibrierung im NOMAD-Experiment*, Diplomarbeit, Universität Dortmund, Germany (1995).

[95] S.B. Boyd, *Neutrino production of opposite sign dimuons in the NOMAD experiment*, Phys. Lett. **B486**, 35–48 (2000), NOMAD memo 98-022, CERN, Geneva 1998.

[96] S.B. Boyd, *Neutrino Production of Opposite Sign Dimuons in the NOMAD Experiment*, Ph.D. thesis, University of Sydney, Australia (1998).

[97] NOMAD Collaboration, P. Astier *et al.*, *Neutrino Production of Opposite Sign Dimuons in the NOMAD Experiment*, CERN EP/2000-072 (2000).

[98] P. Riemann, *Suche nach J/ψ-Mesonen im Frontkalorimeter des NOMAD-Detektors*, Diplomarbeit, Universität Dortmund, Germany (1999).

[99] P.H. Sandler *et al.*, *Neutrino production of same-sign dimuons at the Fermilab Tevatron*, Z. f. Physik **C57**, 1–12 (1993).

[100] H. Kiel, Diplomarbeit, Universität Dortmund, Germany, to be submitted March 2001.

[101] S.R. Mishra *et al.*, *Neutrino tridents and W-Z interference*, Phys. Rev. Lett. **66**, 3117 (1991).

[102] H. Abramowicz *et al.*, *Evidence for ψ production by neutrinos via neutral currents*, Phys. Lett. **109B**, 115 (1982).

[103] M. Althaus, Diplomarbeit, Universität Dortmund, Germany, to be submitted March 2001.

[104] M. Holder *et al.*, CDHS Collaboration, *A detector for high-energy neutrino interactions*, Nucl. Inst. & Meth. **148**, 235–249 (1978).

[105] D. Nordmann, *Untersuchung der Akzeptanz für Myonen aus Frontkalorimeter Ereignissen im NOMAD-Experiment*, Diplomarbeit, Universität Dortmund, Germany (1996).

[106] T. Schmidt, *Untersuchung von Dimyon-Ereignissen im Frontkalorimeter des NOMAD-Detektors*, Diplomarbeit, Universität Dortmund, Germany (1999).

[107] F. Sauli, *Instrumentation in High Energy Physics*, (World Scientific, 1993).

[108] G. Ferrari, P.R. Sala, *GEANT Hadronic Event Generators: a comparison at the single interaction level* (1996), ATLAS Internal Note ATL-PHYS-96-086.

[109] SPY Collaboration, G. Ambrosini *et al.*, *Measurement of pion and kaon fluxes below* 60 GeV/c *produced by* 450 GeV/c *protons on a beryllium target*, CERN-SPSLC/96-01 (1996) .

[110] SPY Collaboration, S. Ragazzi *et al.*, *Secondary Particle Yields from* 450 GeV/c *protons on Beryllium*, SPSC open meeting 1997 .

[111] F. Weber *et al.*, *The Construction and Use of the Flux Reweighting Tables*, NOMAD memo 97-037 (1997), CERN, Geneva.

[112] NOMAD Collaboration, P. Astier *et al.*, *A prototype of an instrumented target for the NOMAD detector*, CERN SPSLC/96-2; SPSLC P 261 Add. 3 (1996), CERN Geneva.

[113] C. Barichello *et al.*, *A* B_4C*-silicon target for the detection of neutrino interactions*, Nucl. Inst. & Meth. **A419**, 1–15 (1998), CERN EP/98-21.

[114] P. Nédélec, S. Soulié, *NOMAD data processing group FARINE web page* http://nomadinfo.cern.ch/Classified/working_groups/DATA/FARINE.

[115] A. Blondel *et al.*(CDHSW), *Electroweak parameters from a high statistics neutrino nucleon scattering experiment*, Z. f. Physik **C45**, 361 (1990).

[116] S.R. Mishra, Univ. South Carolina, USA, *priv. comm.* (2000).

[117] R. Frühwirth, *Application of Kalman Filtering to Track and Vertex Fitting*, Nucl. Inst. & Meth. **A262**, 444 (1987), and references therein.

[118] D. Geppert, *NOMAD DST event display*, NOMAD Collaboration Meeting (March 2000).

[119] R. Brun, F. Rademakers, *ROOT-An Object Oriented Data Analysis Framework*, Nucl. Inst. & Meth. in Phys. Res. **A389**, 81–86 (1997), see also http://root.cern.ch; Proceedings AIHENP96 Workshop, Lausanne, Sep. 1996.

[120] K. Schahmaneche, *Etude de la production de particules neutres étranges et charmées dans les interactions des neutrinos de haute energie. Premiers résultats avec NOMAD*, Ph.D. thesis, University of Paris, Paris (1997).

[121] T. Fazio *et al.*, *NOMAD TRD Electron Identification: Method and First Results*, NOMAD memo 95-041 (1995), CERN, Geneva.

[122] P. Nédélec *et al.*, *NOMAD TRD Identification of Overlapping Tracks*, NOMAD memo 96-005 (1996), CERN, Geneva.

[123] G. Bassompiere *et al.*, *Performance of the NOMAD transition radiation detector*, Nucl. Inst. & Meth. **A411**, 63 (1998).

[124] S.R. Mishra, Univ. South Carolina, USA, *priv. comm.* (2000).

[125] S.R. Mishra, *Update on $\nu_\mu \leftrightarrow \nu_e$ Electron Efficiency*, NOMAD Collaboration Meeting (October 1998), Padova (Italy).

[126] G.J. Feldman, R.D. Cousins, *Unified approach to the classical statistical analysis of small signals*, Phys. Rev. **D57**, 3873 (1998).

Acknowledgements

Finishing a thesis is not possible without the help and guidance of many people.

I am indebted to Prof. C. Gößling of Dortmund University for his confidence and support during the last few years. He offered me the possibility to spend extensive periods of time at CERN, which have been of immense worth to me. Also I am grateful to Prof. S.R. Mishra of South Carolina University for many long discussions, competent advice and for suggesting the FCAL analyses, in particular the possibility for the neutral heavy lepton search.

My thanks go also to all the members of the NOMAD collaboration, without them the experiment would not have been realizable and analyses not possible. I would especially like to thank the NOMAD data processing group, in particular S. Soulié. A. Rubbia for all his work on the NOMAD *MonteCarlo* event generator and D. Steele for everything he did to keep the experiment running. For many discussions and the enjoyable working environment I am grateful to S. Boyd, A. Bueno, L. Camillieri, L. DiLella, J. Dumarchez, A. Geiser, J.J. Gomez-Cadenas, P. Hurst, L. Linssen, P. Nédélec, R. Petti. D. Sillou, P. Soler, S. Valuev, K. Varvell and especially W. Huta.

Also thanks to the members of the Lehrstuhl für Experimentelle Physik IV at the University of Dortmund for discussions and their friendship, in particular B. Schmidt, T. Villett, T. Weiße, R. Wunstorf and J. Wüstenfeld.

Dank an meine Eltern Christa und Franz, als auch an meine Schwester Anke und meine Großmutter Maria G. für alles, was sie für mich getan haben, und vor allem für ihre Liebe.

Et finalement un grand merci à ma chere femme et amie Sylvie pour sa patience et sa compréhension pendant les dernières années et pour son amour.